

Performance studies of CBM Time of Flight (TOF) detector and a few aspects of particle production at a FAIR energy



Somen Gope

Enrolment No. : Phy/18/16 Registration No. : 2180 of 2009-2010

Date of Admission : 28/09/2016

Department of Physics

Gauhati University

This thesis is submitted to

Gauhati University as requirement for the degree of

Doctor of Philosophy

Dedicated to my Family.

Declaration

I hereby declare that the thesis titled “Performance studies of CBM Time of Flight (TOF) detector and a few aspects of particle production at a FAIR energy” is the result of my own research work which has been carried out under the guidance of Prof. Buddhadeb Bhattacharjee, Department of Physics, Gauhati University, Guwahati. I further declare that this thesis as a whole or any part thereof has not been submitted to any university (or institute) for the award of any degree or diploma.

This thesis contains less than 90,000 (ninety thousand) words excluding bibliography and captions.

Somen Gope
06/01/2023

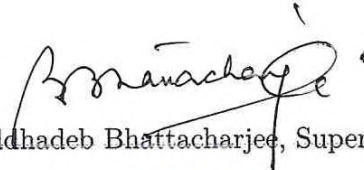
Somen Gope

January 2023

Certificate

This is to certify that the thesis titled “Performance studies of CBM Time of Flight (TOF) detector and a few aspects of particle production at a FAIR energy” is the result of research work of Somen Gope, carried under my supervision, submitted to Gauhati University for the award of the degree of Doctor of Philosophy in Physics.

This thesis conforms to the standard of PhD Thesis under Gauhati University including the standard related to plagiarism and has a similarity index not more than 10% (ten percent), excluding the bibliography.



Prof. Buddhadeb Bhattacharjee, Supervisor

Professor January 2023
Department of Phys
Gauhati University

RAC Member: Prof. Anurup Gohain Barua, Department of Physics, GU



RAC Member: Prof. Kushal Kalita, Department of Physics, GU



4/01/23

Professor
Department of Phys
Gauhati University

Acknowledgements

At the very beginning, I would like to acknowledge my indebtedness and express deep sense of gratitude to my supervisor Prof. Buddhadeb Bhattacharjee, Department of Physics, Gauhati University, for his invaluable guidance and inspiration throughout the course of this study. No word is too high to express my thanks to him for the encouragement and keen interest he has taken in my work.

I am thankful to Prof. A. G. Barua, Prof. M. P. Bora, and Prof. B. Bhattacharjee, all former Heads of the Department of Physics, GU and Prof. Deepali Sarkar, the present Head of the Department of Physics, Gauhati University, for providing me the departmental facilities and other supports in completing my PhD works.

I extend my heartfelt thanks to Prof. A. G. Barua and Prof. K. Kalita of this department for their valuable guidance, encouragement and support during the period of my research as RAC members.

I would like to thank all the faculty members of this department for their kind support and encouragement during the entire period of my research works.

I am thankful to all the office and support staff of the Department of Physics, GU for their constant help and supports during the entire period of my research work.

I shall be failing in my duty if I do not appreciate the help that I have been receiving constantly from my co-workers at Nuclear and Radiation Physics Research Laboratory

(NRPRL), Department of Physics, Gauhati University. Helps received from Dr. Nur Hussain, Dr. Pranjali Sarma are highly acknowledged. I also express my heartfelt thanks to Dr. Kalyan Dey of Bodoland University for his help during the initial days of my research work.

I would also like to thank the Department of Science and Technology (DST), Government of India for providing the necessary grant through a project bearing No. SR/MF/PS-01/2014-GU to install a high performance computing cluster (HPCC) facility at NRPRL, Physics, GU that has been used by me to generate Monte Carlo (MC) events for my research work.

I am thankful to Dr. Volker Friese and Dr. Florian Uhlig of GSI, Darmstadt, Germany for their support in the installation of CBM simulation software. I am also thankful to Dr. Ilya Selyuzhenkov for his support in particle identification using Time of Flight (ToF) geometry.

I thankfully acknowledge the UrQMD group for developing UrQMD and UrQMD-hydro codes and allowing me to use these codes for my research work.

I would also like to thank all my seniors, juniors and batch-mate research scholars of the Department of Physics, Gauhati University for their kind support and help. Also, I am thankful to all the boarders of the V. V. Rao Research Scholars Hostel for their support during my stay at the hostel. Special thanks goes to my roommates Vivek da and Pranab for their company.

I would like to thank my M.Sc. classmates cum friends Tonuj, Hrishikesh, Monomohan, Yoshiko, Suniti, Binita, Pratima for their support throughout my Ph.D. tenure. I would like to thank my other friends Subir, Pratik, Kingshuk, Jayashree, Banashree, Bhaskar, Bikash, Nilam, Kaberi, Dhanjita for their support in different stages of my life. Let me express my heartfelt thanks to Ms. Payel Saha for her inspiring words and support at the critical stages of my research work.

I would like to thank my parents Mr. Radha Raman Gope and Mrs. Rekha Gope for their immense patience and encouragement. Without their love and support, this thesis would not have been possible to complete. I'll never forget the continued support from my brothers Tushar Kanti Gope (elder) and Ashim Gope (younger). I am also thankful to my uncles and aunts and all my cousins, nieces and nephews for their love and support. Further, I am thankful to all my relatives for their support and guidance. Finally, I apologize if someone is forgotten to acknowledge.

Thank you so much all.

Somen Gope
02/01/2023
Somen Gope

Gauhati University, Jalukbari

January 2023

Abstract

One of the primary objectives of the relativistic and (ultra)relativistic heavy-ion collision programs is to explore the QCD phase diagram. In such collisions, exotic nuclear matter far away from normal nuclear density and temperature could be produced.

The Compressed Baryonic Matter (CBM) spectrometer at the Facility for Anti-Proton and Ion Research (FAIR) in Darmstadt, Germany, will be operational some times towards the end of this decade. In order to precisely define the phase diagram of nuclear matter and potential first or second order phase-transitions, the spectrometer seeks to carefully examine, in different phases, rare and bulk probes resulting from heavy ion reactions in the energy range $10 - 45 A GeV$. A time-of-flight (ToF) detector with a polar angular coverage of $2.5 - 25$ degree, that is set at a distance of $10 m$ from the target is the most crucial tool for hadron identification. According to simulations, the cell occupancy must be limited to $< 5\%$ while separating pions, kaons, and protons up to a few GeV/c momentum, which calls for a ToF resolution of $80 ps$ at high efficiency. The studies of physical observable at such unprecedented rate of $10 MHz$ using such a high efficient and wide acceptance Time of Flight (ToF) detector will be a very important aspect of CBM experiment. It, thus, becomes very pertinent to undertake CBM-ToF simulation and physics performance studies to realize its applicability under high luminosity, high reaction rate, and particularly for central

nuclear collision scenario. In this investigation, an attempt has therefore been made to identify light flavour hadrons, namely, pions (π^\pm), kaons (K^\pm), and protons (p, \bar{p}) with CBM simulation software for ToF detector and also to draw the m_T -spectra for this identified hadrons and hence to calculate the effective temperature of the system that would be produced in the CBM experiment through Au-Au collision at 10 AGeV.

Exploring the QCD phase diagram is one of the main goals of the relativistic and ultra-relativistic heavy-ion collision programmes. The overlapping region of the colliding nuclei can produce nuclear matter with temperatures and densities much higher than normal nuclear matter. It is possible that in relativistic heavy ion collisions, nuclear matter is created at vanishingly low or zero net-baryon density and extremely high temperature (RHIC and LHC), or at extremely high baryon density and moderate temperature (FAIR and RHIC-BES), depending on the collision energy and system under consideration. There is considerable experimental evidences that nuclear matter experiences a type of hadronic to partonic phase transition in both the circumstances. According to lattice QCD calculations, a theoretical model that is quite succesful in describing such high energy sub-atomic collisions the hadronic to partonic phase transition is of first-order type at high baryochemical potential μ_B (high net baryon density, $B - \bar{B}$), while the deconfined phase transition is of cross-over type at low μ_B (low net baryon density, $B - \bar{B}$). The QCD model calculation predicts, the cross-over and first-order phase transition have a critical end-point at roughly 160 *MeV*. However, the precise location of the critical point is yet to be ascertained, primarily due to experimental challenges and model reliance. The experimental fingerprints linked to the critical point, according to hydrodynamic prediction, are most pronounced at beam energies between the AGS and top SPS energies. Therefore, it is very much important to investigate some key physics observables at such beam energies to realize QCD critical point. Further, another important aspect of (ultra) relativistic heavy

ion collision studies is understanding the particle production mechanism. That is, how hadrons are being produced in such A-A collisions. In this work, an attempt has also been made, by analysing the hybrid UrQMD-hydro generated data for Au-Au collisions at 10 AGeV to investigate the dynamical fluctuation in particle multiplicity that might have arisen due to the existence of a QCD critical point and/or due to different hadronization mechanisms.

In chapter-1, a brief introduction to heavy ion collisions is provided. (Ultra) Relativistic heavy ion collisions are the collision of two Lorentz contracted nuclei (clouds of nucleons) which are moving (in Center of mass frame) almost with the speed of light and collide at some point. Such collisions might result in a hot and dense fireball resulting in the deconfinement of partons out of hadrons. This hot and dense nuclear matter then expands and free partons may recombine/coalesce in hadrons again. These hadrons are then detected by detectors. So, we started with hadrons and end up with hadrons again. The entire process takes a time of the order of 10-15 fm/c . It is therefore not possible to directly measure various parameters of the nuclear matter, thus produced in such collision. One has to rely on indirect measurement of the signature of heavy ion collision. Various observables related to heavy ion collisions are proposed by different workers to probe and characterize the exotic nuclear matter produced in such nuclear collisions, to understand the particle production mechanism, etc. A few global observables of heavy ion collision are discussed in detail in chapter 1. Event generators are essential tools of simulation and phenomenological studies of high energy heavy ion collisions. A few event generators have also been described in detail in chapter-1.

Chapter-2 contains the descriptions of simulation tools and detectors, with special reference to the Time of Flight (ToF) detector of the Compressed Baryonic Matter (CBM) experiment at Facility for Anti-proton and Ion Research (FAIR), Darmstadt,

Germany. The word *simulation* implies the imitation of a physical system of the selected system or process. Simulation models are key factors that represent the key features of the selected system or process. Simulation is frequently done in nuclear physics before the real experiment. High-energy nuclear and particle physics experiments are mainly focused on realizing several physics goals and are very much expensive and complicated due to their difficult design. Such a complex experiment generally consists of several sub-systems and sub-detectors. The goal of such an experiment may not be achieved if the design and performance of the sub-systems and sub-detectors are not perfect. Therefore, for the best result, detailed simulation studies are immensely essential to the design and performance studies of detectors using simulation tools for individual detector systems. Chapter-2 contains a brief description of various sub-detectors of CBM spectrometer, the CBM simulation tools used for ToF simulation and its physics performance studies.

Chapter-3 contains the physics performance studies of the CBM-ToF detector at 10 AGeV for central Au+Au collision. The CBM detector setup comprises several detectors for the identification of leptons and hadrons. Time of Flight (ToF) is one of the core detectors of the CBM experiment that will be used to identify charged hadrons by measuring flight time. In this chapter, an attempt has been made to identify light-flavored hadrons namely pion, kaon, and proton using ToF detector tracking algorithm of CBM experiment and estimate their yields for central (impact parameter $b = 0-3$ fm) Au+Au collisions at 10 AGeV beam energy. The effective temperature of the fireball created in such collision has been estimated with identified charged hadrons. The effective temperature evaluated from m_T spectrum of the reconstructed tracks of the present investigation is found to follow the expected mass ordering. The rapidity and p_T spectrum have also been drawn for these light flavoured hadrons. The widths of the rapidity distribution are found to follow the expected mass ordering.

The chapter-4 contains the studies of particle multiplicity fluctuation for primary charged particles in different phase spaces. In this chapter, an attempt has been made, in the light of scaled factorial moment (SFM) analysis, to investigate hybrid UrQMD-hydro generated events of Au+Au collisions at 10 AGeV to find the role of hydrodynamic evolution on observed intermittency, if any. In two dimensional cumulant $\chi(\eta - \phi)$ space, $\ln \langle F_q \rangle$ values for $q = 2 - 6$ are found to increase with increasing values of $\ln M^2$ indicating unambiguously the presence of intermittency in our data sample generated with both chiral and hadronic equations of state (EoS). Although various late processes like meson-meson (MM) and meson-baryon (MB) hadronic re-scattering and/or resonance decays are found to influence the intermittency index significantly, these processes could not be held responsible for the observed intermittency in hybrid UrQMD-hydro data. Moreover, the signature of intermittency is also found to exist in different sets of data samples generated with a change in initial conditions such as the start time (t_{start}) and transition energy density (TED) of the UrQMD-hydro model confirming the robustness of the observed power law behavior $F_q \propto (M^2)^{\alpha_q}$ in our various generated sets of hydro data. Such SFM studies with π , K , and p on two dimensional cumulant $\chi(\eta - p_T)$ space reveals a clear indication of non-thermal phase transition in the data sample of this work with hybrid UrQMD-hydro model.

Chapter-5 is the summary of the important results obtained from these investigation and conclusion made on the observed findings.

List of Publications

Publications in refereed journals

1. Somen Gope and Buddhadeb Bhattacharjee, *Signature of intermittency in hybrid UrQMD-hydro data at 10 AGeV Au+Au collisions*, Eur. Phys. J. A 57:44 (2021)
2. Somen Gope and Buddhadeb Bhattacharjee, *Physics performance studies of CBM-TOF detector*, Acta Physica Polonica B 53, 9-A3 (2022).

Conference Proceedings

1. S. Gope and B. Bhattacharjee, *Intermittency in hybrid UrQMD-hydro data.*, Proc. of the DAE Symp. on Nucl. Phys. 59, 736 (2019).
2. S. Gope and P. Srama, *Evidence of nonthermal phase transition in Au-Au collisions at $E_{lab}=10$ AGeV for AMPT generated data.*, DAE Symp. on Nucl. Phys.

Technical Reports

1. S. Gope and B. Bhattacharjee, *Charged particle identification with CBM-ToF* CBM Progress Report 2017, Darmstadt p-157.

DOI: 10.15120/GSI-2018-00485 (<https://dx.doi.org/10.15120/GSI-2018-00485>)

ISBN 978-3-9815227-5-4

Conference/Workshop/School Attended

1. Oral presentation at 65th DAE Nucl. Phys. Symp. (2021) with title *Evidence of nonthermal phase transition in Au-Au collisions at $E_{lab} = 10$ AGeV for AMPT generated data* held at DAE Convention Center, Anushaktinagar, Mumbai (India), 1-5 December 2021.
2. Presented a poster at 64th DAE Nucl. Phys. Symp. (2019) with title *Intermittency in hybrid UrQMD-hydro data* held at Lucknow University, Lucknow, Uttar Pradesh (India), 23-27 December 2019.
3. Oral presentation at National Seminar on Progresses in Nuclear and High Energy Physics, with presentation entitled *Identification of light flavor hadrons using TOF detector of proposed FAIR CBM experiment* held at Gauhati University, Guwahati (India), 30-31 March 2018.
4. Attended XI SERC School of Experimental High Energy Physics at National Institute of Science Education and Research (NISER), Jatni, Odisha, India from 7-27 November 2017.
5. Presented a poster at XIIth Biennial National Conference of Physics Academy of North East, held at St. Anthony's College, Shillong, Meghalaya, (India), 10-12 November 2016.

Table of contents

List of figures	xxv
List of tables	xxxi
1 Introduction	1
1.1 Introduction to Quantum Chromodynamics	1
1.2 High energy heavy ion collisions	5
1.3 Event generators of heavy ion collisions	8
1.3.1 UrQMD Model	9
1.3.2 UrQMD-hydro Model	11
1.4 Observables of heavy-ion collisions	13
1.4.1 Particle multiplicity	14
1.4.2 Rapidity and pseudorapidity	14
1.4.3 Transverse mass and transverse momentum	16
1.4.4 Nuclear modification factor	17
1.4.5 Multi-particle correlation	19
1.5 Motivation of the present work	19

2	CBM simulation tools and detectors	23
2.1	Introduction:	23
2.2	CBM detector system:	25
2.2.1	Micro Vertex Detector	25
2.2.2	Silicon Tracking System:	26
2.2.3	Muon Chamber:	27
2.2.4	Ring Imaging Cherenkov Detector:	28
2.2.5	Transition Radiation Detector:	29
2.2.6	Time of Flight Detector:	30
2.2.7	Electromagnetic Calorimeter:	30
2.2.8	Projectile Spectator Detector:	31
2.3	Software Tools:	32
2.3.1	FairSoft:	34
2.3.2	Simulation procedure:	37
3	Physics performance studies of CBM-ToF detector	43
3.1	Introduction	43
3.2	Method of particle identification	52
3.3	Results	56
3.4	Summary	63
4	Scaled factorial moment analysis of multiplicity fluctuation	65
4.1	Introduction	65
4.2	UrQMD hydrodynamic model	74
4.3	MC data generation using High Performance Computing Cluster(HPCC)	76
4.4	Mathematical formalism of scaled factorial moment analysis	77
4.5	Results	81

4.6 Summary	102
5 Summary	103
References	111

List of figures

1.1	The graphical representation of QCD potential as a function of distance between the strongly interacting particles [3].	2
1.2	(a) The relationship between p/T^4 and temperature, (b) ϵ/T^4 in terms of temperature as a function of the critical temperature (T_c). The lattice QCD computations utilising 2-flavours, 2+1 flavors, and 3-flavours, respectively, are shown by the red, green, and blue lines and points. The Stefan-Boltzmann limit is indicated by the horizontal arrow.[4].	4
1.3	Classification of events according to multiplicity for UrQMD simulated data at 40 AGeV Au+Au collisions [28].	15
1.4	Transverse mass spectra of identified particles at $\sqrt{s_{NN}} = 200\text{GeV}$ for $p - p$ and $Au - Au$ collisions [30].	17

1.5	The PACIAE + DCPC model calculates the nuclear modification factor (R_{AA}) as a function of p_T for various particle species in 0-5% most central and 40-60% peripheral $Pb - Pb$ collision events at $\sqrt{s_{NN}} = 2.76 TeV$. The ALICE data (solid markers) is used for the comparison and are shown in panel (c), (d) and (e). The shaded areas reflect the systematic uncertainty of the experimental data, and the vertical lines display the statistical uncertainty [32].	18
2.1	Pictorial view of various detectors of CBM experiment [37].	25
2.2	Pictorial view of different parts of CBM-STS detector [39].	26
2.3	Pictorial view of different parts of CBM-MUCH detector [40].	28
2.4	Pictorial view of CBM-RICH detector [41].	29
2.5	Pictorial view of CBM-TRD detector [42].	30
2.6	Pictorial view of CBM-ECAL detector [44].	31
2.7	Pictorial view of CBM-PSD detector [45].	32
2.8	Block diagram of FairRoot software framework [38, 47].	33
2.9	(a) The block diagram of the chain of the simulation procedure, and (b) the chronological order of CBM simulation procedure.	38
3.1	Modules arrangement in ToF detector wall.	50
3.2	Pictorial view of arrangements of MRPC in ToF detector wall.	51
3.3	(a) Monte Carlo (MC) points, and (b) hits distributions in time of flight detector wall.	56
3.4	$1/\beta$ vs. p/q plots for primary charged particles produced in Au+Au collisions at 10 AGeV beam energy with m^2 cuts (a) 1σ , and (b) 2σ . (c) published $1/\beta$ vs. p/q plot of I. Deppner and N. Herrmann for CBM collaboration [76].	57
3.5	m^2 distribution of primary particles produced in Au+Au collisions. . .	58

3.6	y vs. p_T acceptance of CBM-ToF detector for (a) pions, (b) kaons, and (c) protons, produced in Au+Au collisions at 10 AGeV beam energy.	59
3.7	m_T spectra of identified light flavored hadrons ($\pi^+ + \pi^-$), ($K^+ + K^-$), and ($p + \bar{p}$).	60
3.8	Rapidity spectra of identified light flavored hadrons ($\pi^+ + \pi^-$), ($K^+ + K^-$), and ($p + \bar{p}$).	61
3.9	p_T spectra of identified light flavored hadrons ($\pi^+ + \pi^-$), ($K^+ + K^-$), and ($p + \bar{p}$).	62
3.10	p_T dependent efficiency plots of CBM-TOF detector for light flavored hadrons ($\pi^+ + \pi^-$), ($K^+ + K^-$), and ($p + \bar{p}$).	63
4.1	The scaled variance ω against beam energy. The figure is taken from ref. [86].	69
4.2	Net-charge fluctuations, $v_{(+-,dym)}$, of charged particles produced in Au+Au collisions at $E_{lab} = 10-40$ AGeV, and $\sqrt{S_{NN}} = 7.7, 11.5$ GeV as a function of number of participants, N_{part} . The plot has been taken from ref. [92, 93]	70
4.3	Upper panel: Mean transverse momentum distributions at $E_{lab} = 40, 80$ and 158 AGeV/c. Data events indicated by circles and solid line represent the mixed events. Lower panel: The ratio between the distributions of data events to mixed events for all three energies. The plot has been taken from ref. [98]	72
4.4	Pictorial view of high performance computing cluster (HPCC) of NRPRLLaboratory, Department of Physics, Gauhati University.	77

4.5	Transverse mass spectra of π^+ for Au+Au collisions at 8 AGeV (a) m_T spectra plotted with our set of UrQMD-hydro generated data and compared with the plot of E895 experimental result [128] (b) ratio of m_T spectra of π^+ of the experimental to our generated data. (c) compared published spectra by C. Spieles using UrQMD-hydro data with experimental spectra of E895.	82
4.6	Density distribution spectrum for (a) a single event in 2D $\eta - \phi$ space, (b) entire sample in 2D $\eta - \phi$ space and (c) entire sample in 2D $\chi(\eta - \phi)$ spaces.	83
4.7	$\ln \langle F_q \rangle$ vs $\ln M^2$ plots for (a) UrQMD-hydro (default) events and UrQMD and RAN-GEN events (inset) (b) for UrQMD-hydro events with hadronic and chiral equations of state (EoS). Solid straight lines are the best fitted lines to the data points.	84
4.8	$\ln \langle F_q \rangle$ vs $\ln M^2$ in $\chi(\eta - \phi)$ space for UrQMD-hydro data with different start time (t_{start}). Solid straight lines are the best fitted lines for the data points.	87
4.9	$\ln \langle F_q \rangle$ vs $\ln M^2$ in $\chi(\eta - \phi)$ space for UrQMD-hydro data with two different transition energy density (TED). Solid straight lines are the best fitted lines for the data points.	87
4.10	(a) Intermittency index (α_q) vs q and (b) anomalous fractal dimension (d_q) vs q for UrQMD-hydro data with chiral and hadronic EoS.	88
4.11	$\ln \langle F_q \rangle$ vs $\ln M^2$ in $\chi(\eta - \phi)$ space for UrQMD-hydro data with (a) MM and MB scattering off (b) resonance decays off (c) both MM, MB scattering and resonance decays off. Solid straight lines are the best fitted lines for the data points.	90

4.12	The variation of λ_q against q for UrQMD-hydro generated data at 10 AGeV Au-Au collisions.	93
4.13	$\ln \langle F_q \rangle$ vs. $\ln M^2$ plot for all charged particles in $\chi(\eta - p_T)$ space for UrQMD-hydro data with (a) chiral EoS, and (b) hadronic EoS.	94
4.14	$\ln \langle F_q \rangle$ vs. $\ln M^2$ plot for pion in $\chi(\eta - p_T)$ space for UrQMD-hydro data with (a) chiral EoS, and (b) hadronic EoS.	95
4.15	$\ln \langle F_q \rangle$ vs. $\ln M^2$ plot for kaon in $\chi(\eta - p_T)$ space for UrQMD-hydro data with (a) chiral EoS, and (b) hadronic EoS.	96
4.16	$\ln \langle F_q \rangle$ vs. $\ln M^2$ plot for proton in $\chi(\eta - p_T)$ space for UrQMD-hydro data with (a) chiral EoS, and (b) hadronic EoS.	97
4.17	Intermittency indices(α_q) vs. order of moments (q) plot for π , K , and p in $\chi(\eta - p_T)$ space with (a) chiral EoS, and (b) hadronic EoS.	98
4.18	Variation of values of anomalous fractal dimension (d_q) against order of moments (q) for identified pion, kaon and proton using UrQMD-hydro data with (a) chiral EoS, and (b) hadronic EoS.	99
4.19	λ_q vs. q plot for all charged particles with (a) chiral EoS, and (b) hadronic EoS.	100
4.20	λ_q vs. q plot for identified pion, kaon, and proton using UrQMD-hydro data with (a) chiral EoS, and (b) hadronic EoS.	100

List of tables

1.1	List of baryons of UrQMD event generator.	10
1.2	List of mesons and meson resonances included in UrQMD and classified according to their spin and parity.	10
3.1	Inverse slope and χ^2/NDF for $(\pi^+ + \pi^-)$, $(K^+ + K^-)$, and $(p + \bar{p})$. . .	61
3.2	Widths of the rapidity distribution of $(\pi^+ + \pi^-)$, $(K^+ + K^-)$, and $(p + \bar{p})$	61
4.1	Intermittency index values for $q=2-6$ for various systems using UrQMD-hydro model	91
4.2	Intermittency index and λ_q values for order of moment $q = 2 - 5$ for all charged particles and different identified particles using UrQMD-hydro model	101

1

Introduction

1.1 Introduction to Quantum Chromodynamics

A well-known theory of strong interaction that describes the interaction between partons (quarks and gluons) is known as quantum chromodynamics (QCD). Quarks and gluons, together called partons, whose interactions adhere to the rules of relativistic quantum field theory (QFT) with a non-abelian gauge invariance $SU(3)$, are the particles of QCD

theory. Like the electric charge in the QED, the quarks and gluons are characterised by a new quantum number called the *colour* [1]. The potential of strong interactions between two quarks or color charges depends on the separation (r) between them and is represented by V_s . The quark-(anti)quark potential is represented by equation 1.1., where α_s is the strong coupling constant, signifies the strength of the interaction, and b defines the string tension between them. The first term of equation 1.1 is inversely proportional to the distance and is similar to coulomb potential. On the other hand, the second term is motivated by a string picture of quark confinement. In this scenario, the color string keeps interacting quarks bound. If r increases, the string tension b also increases, and similarly, potential energy also increases, which means more energy is needed to separate the quarks. In other words, a huge amount of energy will be necessary to separate the constituent quarks of hadrons, which is popularly known as the confinement property of strong interaction [2]. The strong coupling constant (α_s) is energy-dependent, not a fixed quantity like that of QED. The variation of potential as the function of r is shown in Fig. 1.1.

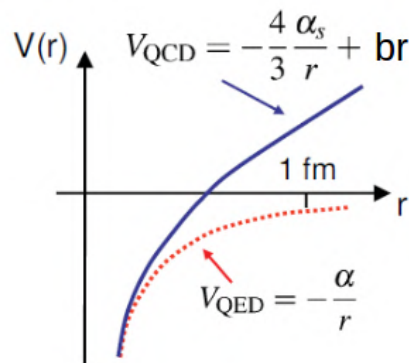


Fig. 1.1 The graphical representation of QCD potential as a function of distance between the strongly interacting particles [3].

$$V_s = -\frac{\alpha_s}{r} + br \quad (1.1)$$

The confinement property of color charge is true for normal nuclear matter density and temperature. However, when the matter density and/ or temperature are very high, the hadronic matter is transformed to Quark Gluon Plasma (QGP), a new state of matter where the quarks and gluons are the degrees of freedom. In such a medium, the partons can move freely, not confined inside a particular hadron. In the QGP medium, equation 1.1 is not effective. So, the modified formula of potential is given by equation 1.2.

$$V_s(T, r) = -\frac{\alpha_s}{r} e^{-\frac{r}{r_D}} \quad (1.2)$$

where, r_D is the Debye length and T is the temperature.

The phase transition from hadronic matter to QGP is illustrated by simple thermodynamic model. The thermodynamic variables such as pressure (P) of hadronic gas follows the simple form of Stefan-Boltzmann formula as represented by equation (1.3) and the equation of energy density (ϵ) bears a relationship with pressure (P) as given by equation (1.4).

$$P = g_{eff} \frac{\pi^2}{90} T^4 \quad (1.3)$$

Here, g_{eff} represents the effective degrees of freedom (DOF). It varies with the matter created in collisions, for pion gas the value of g_{eff} is 3, and for QGP matter its value is 47.5.

Energy and pressure are related through the following relation:

$$\epsilon = 3 \times P \quad (1.4)$$

The ratios of thermodynamic variables P/T^4 and ϵ/T^4 can provide information about the effective DOF of created matter in nuclear collisions.

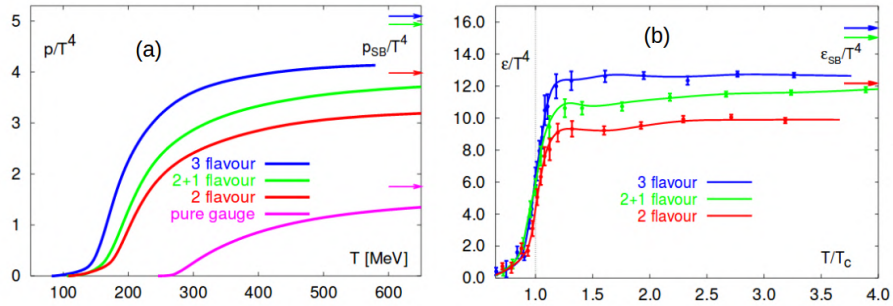


Fig. 1.2 (a) The relationship between p/T^4 and temperature, (b) ϵ/T^4 in terms of temperature as a function of the critical temperature (T_c). The lattice QCD computations utilising 2-flavours, 2+1 flavors, and 3-flavours, respectively, are shown by the red, green, and blue lines and points. The Stefan-Boltzmann limit is indicated by the horizontal arrow.[4].

Even though perturbative QCD ($pQCD$) computations excel at large momentum transfer (Q), they falter at small Q , which corresponds to a distance of the order of hadronic size ($1fm$), necessitating the use of a non-perturbative technique. The Lattice QCD is one such non-perturbative method. The branch of quantum chromodynamics that is known as lattice QCD (lQCD) treats space-time as discrete points on a lattice and is based on numerical Monte-Carlo simulation [5]. At a critical temperature of approximately $170MeV$ and at a critical energy density of $1GeV/fm^3$, lattice QCD anticipated a phase transition from hadronic matter to a deconfined state of quarks and gluons. According to Lattice QCD simulation, Figs. 1.2 (a) and (b) respectively depicts the variation of pressure and energy density as a function of temperature, both normalised by T^4 . The phase transition from hadronic to partonic degrees of freedom is shown by the abrupt shift in pressure and energy density at a specific temperature, $T = T_c$.

1.2 High energy heavy ion collisions

As mentioned above, QCD theory predicts that at extremely high pressure and temperature the normal nuclear matter may go through a transition to a color-conducting deconfined state of quarks and gluons known as quark-gluon plasma (QGP), and subsequently there will be transition from QGP to hadrons again [6]. Studies on QCD phase transition aims to find answers to a number of unresolved mysteries of nature, such as - what are the mechanisms of hadronization? why universe is matter dominant? how did the elementary particle got their masses? etc.

According to lattice QCD (lQCD) calculation a situation like early universe can be recreated in the laboratory through the collision of energetic nuclei [7]. The expectation is to match the temperature and matter density similar to the universe existed about $10^{-6}sec$ after its birth. It occupies a small volume in laboratory, typically around $10^2 - 10^3 fm^3$, and its survival time is approximately $50fm/c$. This event is known as the *Little bang*, and is a tiny replica of the big bang [8].

In heavy ion collision, a large amount of energy is deposited into the region of overlapping portion of the colliding nuclei, creating thereby a system known as a *fireball* [9]. Depending on the initial conditions, the fireball energy density can rise to such a high value that new forms of matter may be created. As mentioned above, the search for such a new phase of matter is the central objective of studying high energy heavy-ion collisions.

The history of high-energy nucleus-nucleus collisions dates back to the 1970s. There can be two types of High Energy-HIC experiments, such as (a) fixed target experiments, where one of the colliding nuclei remains fixed in the laboratory. The other type is (b) collider experiments, where both the colliding nuclei are made to move towards each other from opposite directions almost with the speed of light and collide. The advantage of collider facilities is that at the same incident beam energy, the energy

available in the center of the momentum system is much higher in magnitude than that available in a fixed target facility. The disadvantage is that in colliders, the collision rate is lower by a factor of $10^2 - 10^3$ than that in the fixed target experiments [10].

- **Collider experiments:**

Relativistic Heavy Ion Collider Experiment: The first collider experiment, the Relativistic Heavy Ion Collider (RHIC) at Brookhaven National Laboratory (BNL), US, began in 2000 with a design luminosity of $1400 (\mu b)^{-1}$ Au-Au collisions per second. RHIC gathered data on Au-Au collisions up to a maximum center-of-mass energy of 130 GeV per nucleon pair in 2000 during its initial operation. The following three runs, which took place between 2001 and 2004, allowed RHIC to collect data up to the maximum energy of 200 GeV ($\sqrt{s_{NN}}$). To provide an appropriate reference point for the more complex Au-Au collisions, RHIC additionally gathered data for several colliding systems, including pp, d-Au, and Cu-Cu collisions at various energies (maximum $\sqrt{s_{NN}} = 200$ GeV). RHIC consists of four major experiments with various experimental goals, namely (i) BRAHMS, (ii) PHOBOS, (iii) PHENIX, and (iv) STAR [11].

Large Hadron Collider experiment: The Large Hadron Collider (LHC) at CERN has been successfully operating since 2009, making it the biggest and highest-energy particle accelerator in the world. Proton-proton, proton-lead, and lead-lead collisions at the TeV energy ranges have extensively been studied at the LHC. It consists of four major experiments: the Compact Muon Solenoid (CMS), A Large Ion Collider Experiment (ALICE), the ATLAS, and the Large Hadron Collider beauty (LHCb) [12].

- **Fixed target experiments:** A few examples of high energy fixed target particle accelerators are, (i) Synchrotron at JINR, Dubna, (ii) AGS at BNL, Brookhaven, (iii) SIS at GSI, Darmstadt, Germany, etc.

The Facility for Anti proton and Ion Research:

The future Facility for Antiproton and Ion Research (FAIR) will be a unique international particle accelerator facility that will provide research opportunities in diverse fields of physics viz. nuclear, particle, atomic and plasma physics [13]. The facility at FAIR will accelerate a varieties of nuclei right from Hydrogen to Uranium with beam energies ranging from 2–45A GeV. FAIR is unique in the sense that it will provide beams with unprecedented beam intensity with brilliant beam quality [14, 15]. In this new facility, a set of four beamlines will be operational to use: (i) radioactive ion beams for nuclear physics; (ii) exploring novel phenomena in hadron physics using antiprotons; (iii) laser and plasma physics, and (iv) physics of strongly interacting matter at extreme density. Accordingly, four scientific collaborations, comprising nearly 3000 researchers from 53 countries were formed. These collaborations are- APPA: Atomic, Plasma Physics and Applications [16]; PANDA: anti-Proton ANnihilation at Darmstadt [17]; NUSTAR: NUclear STructure, Astrophysics and Reactions [18]; and CBM: Compressed Baryonic Matter experiments [19].

The new FAIR facility will be comprised of (i) a proton-LINAC to inject a high-intensity proton beam to the main rings; (ii) double rings (having circumference 1.1 km) with rigidities 100 and 300 Tm known as SIS-100 and SIS-300 respectively housed in the same tunnel; and (iii) superconducting fragment separator (Super-FRS).

The proposed CBM experiment at FAIR is designed to explore the QCD phase diagram in the region of high baryon densities and moderate temperature, a condition that is believed to be analogous to the situation at the heart of a neutron star. Along with bulk particles, the main thrust of the CBM experiment would be the detection of the messengers of the fireball created at the early stages

of the heavy-ion collisions. These are the particles with very low production cross-section, also known as rare probes such as ψ' , J/ψ , \bar{D}^0 , D^0 , D^\pm , etc. To measure these rare probes, the CBM experiment will be run under an extreme reaction rate. For some observables, there will be dedicated runs with luminosity up to 10 MHz . To work efficiently under such an unprecedented reaction rate requires development of ultra-fast and extreme radiation hard detectors and electronics. Simulation of detector geometry and physics performance studies of various sub-detectors of CBM experiment thus becomes inevitable. A few physics observables related to the CBM experiment are briefly described in section 1.4.

1.3 Event generators of heavy ion collisions

Event generators, as such are computer programs written in Fortran, C, C++ or other high level language where Monte Carlo (MC) approach are taken to calculate cross-section, matrix elements for various physical processes, fragmentation functions etc.

The Monte Carlo technique is used in event generators of heavy ion collisions to choose all pertinent variables in accordance with the required probability distributions. With the aid of the Monte Carlo technique, the idea of randomness (or probability) as given by quantum mechanics can be implemented in the event generators. A list of all final state observable particles, such as hadrons, leptons, and photons, along with their details, such as momenta, isospin, charges, pdg codes, and space-time coordinates, is often what is meant by an *event*. An event is thus a h-h, h-A, or A-A collision along with all the relevant parameters of particles photons and nuclei produced in such a collision.

Monte-Carlo event generators are the prime tools for the detector simulation for relativistic or ultra-relativistic heavy ion collisions. Various transport models are used for this type of simulation work. These transport models such as GEANT3, GEANT4 etc are useful for different detector simulations depending on the collision system, beam energies, detector parameter etc. In FAIR energies, the successful event generators are UrQMD, UrQMD-Hydro, SMASH, AMPT, HSD, PHSD, etc. The details of UrQMD (Ultra-relativistic Quantum Molecular Dynamics) and UrQMD-hydro models, used in this work, are briefly described in the following sections.

1.3.1 UrQMD Model

The Ultra relativistic Quantum Molecular Dynamics model [20] is a theory of microscopic particles that is based on covariant propagation of hadrons. Projectile beam and target are modelled using the Fermi-gas ansatz. In this model, Gaussian shaped density distribution function is used to represent nucleons, and the function is given by equation 1.5 [20].

$$\phi_j(x_j, t) = \left\{ \frac{2\alpha}{\pi} \right\}^{3/4} \exp\left\{ -\alpha(x_j - r_j(t))^2 + \frac{2\pi i}{h} p_j(t)x_j \right\} \quad (1.5)$$

Where, x_j and p_j are generalized co-ordinate and momentum respectively.

The wave function Φ of nucleus is the product of the wave functions of the nucleons ϕ and is represented by equation 1.6 [20].

$$\Phi = \prod_j \phi_j(x_i, p_i, t) \quad (1.6)$$

The interaction is based on a non-relativistic density-dependent Skyrme-type equation of state with additional Yukawa and Coulomb potentials. The nucleon or baryon-density can be obtained from the Gaussian distribution function [20]-

$$\rho_j(x_j, t) = \left\{ \frac{2\alpha}{\pi} \right\}^{3/2} \exp\{-2\alpha(x_j - r_j(t))^2\} \quad (1.7)$$

Table 1.1 List of baryons of UrQMD event generator.

Nucleon	Δ	Λ	Σ	Ξ	Ω
N_{938}	Δ_{1232}	Λ_{1116}	Σ_{1192}	Ξ_{1317}	Ω_{1672}
N_{1440}	Δ_{1600}	Λ_{1405}	Σ_{1385}	Ξ_{1530}	
N_{1520}	Δ_{1620}	Λ_{1520}	Σ_{1660}	Ξ_{1690}	
N_{1535}	Δ_{1700}	Λ_{1600}	Σ_{1670}	Ξ_{1820}	
N_{1650}	Δ_{1900}	Λ_{1670}	Σ_{1775}	Ξ_{1950}	
N_{1675}	Δ_{1905}	Λ_{1690}	Σ_{1790}	Ξ_{2025}	
N_{1680}	Δ_{1910}	Λ_{1800}	Σ_{1915}		
N_{1700}	Δ_{1920}	Λ_{1810}	Σ_{1940}		
N_{1710}	Δ_{1930}	Λ_{1820}	Σ_{2030}		
N_{1720}	Δ_{1950}	Λ_{1830}			
N_{1900}		Λ_{1890}			
N_{1990}		Λ_{2100}			
N_{2080}		Λ_{2110}			
N_{2190}					
N_{2200}					
N_{2250}					

Table 1.2 List of mesons and meson resonances included in UrQMD and classified according to their spin and parity.

0^{+-}	1^{--}	0^{++}	1^{++}	1^{+-}	2^{++}	$(1^{--})^*$	$(1^{--})^{**}$
π	ρ	a_o	a_1	b_1	a_2	ρ_{1450}	ρ_{1700}
K	K^*	K_o^*	K_1^*	K_1	K_2^*	K_{1410}^*	K_{1680}^*
η	ω	f_o	f_1	h_1	f_2	ω_{1420}	ω_{1662}
η'	ϕ	f_o^*	f_1'	h_1'	f_2^*	ϕ_{1680}	ϕ_{1900}

The UrQMD collision term contains 55 different baryon species (including nucleon, delta and hyperon resonances with masses up to $2.25 \text{ GeV}/c^2$) and 32 different meson species (including strange meson resonances), which are supplemented by

their corresponding anti-particle and all isospin-projected states. The baryons and baryon-resonances which can be populated in UrQMD are listed in table 1.1, the respective mesons in table 1.2 [20, 21]. The states listed can either be produced in string decays, s-channel collisions or resonance decays. For excitations with higher masses than $2 \text{ GeV}/c^2$ a string picture is used. Full baryon/antibaryon symmetry is included: the number of implemented baryons therefore defines the number of antibaryons in the model and the antibaryon-antibaryon interaction is defined via the baryon-baryon interaction cross sections. The model also includes meson-meson (MM) and meson-baryon (MB) interactions.

1.3.2 UrQMD-hydro Model

The hybrid UrQMD-hydro model is based on the theory of ideal fluid where initial and final stages of a collision are described by the UrQMD transport model [22]. On the other hand, for the description of the intermediate stage of such collision, hydrodynamic evolution of the nuclear matter is considered. Ideal, relativistic one-fluid dynamics is based on the conservation of energy, momentum, and the net-baryon number current. For the hydrodynamical evolution, one assumes local equilibrium and zero viscosity, which corresponds to zero mean free path. The two conservation equations that govern the evolution are [22]-

$$\partial_\mu T^{\mu\nu} = 0 \text{ and } \partial_\mu N^\mu = 0$$

Where, $T^{\mu\nu}$ is the energy momentum tensor and N^μ is the baryon current.

For ideal fluid, the form of $T^{\mu\nu}$ is as follows-

$$T^{\mu\nu} = (\epsilon_{trf} + P)u^\mu u^\nu - P g^{\mu\nu} \text{ and } N^\mu = \rho_{trf} u^\mu$$

The mathematical quantities ϵ, P , and ρ_{lrf} represent the energy density, pressure, and net-baryon density in local rest frame. u^μ is the four velocity, $g^{\mu\nu}$ is the metric tensor.

The equation of motion are solved in the following form by employing computational frame quantities ϵ_{cf}, p^i , and ρ_{cf} for the energy, momentum, and net-baryon number densities.

$$\partial_t \epsilon_{cf} + \nabla \cdot \epsilon_{cf} v = -\nabla(Pv), \quad (1.8)$$

$$\partial_t p + \nabla(pv) = -\nabla P, \quad (1.9)$$

$$\partial_t \rho_{cf} + \nabla \rho_{cf} v = 0. \quad (1.10)$$

In this case, the full (3+1)-dimensional hydrodynamic evolution is performed using the SHASTHA algorithm [22].

The equation of state (EoS) is needed as an additional input to calculate the pressure, temperature, chemical potential corresponding to the energy and the baryon number densities [22, 23]. Since the evolution of the system is driven by pressure gradient, the EoS has the most important influence on the evolution. In the EoS, the pressure as a function of energy, and the net baryon number density are required as inputs in order to solve the hydrodynamical equations of nuclear matter. It can appear detrimental to have this additional uncertainty in the model because the precise EoS of hot and dense QCD matter is still unknown. However, being able to examine changes in the dynamics of the bulk matter while altering the EoS and identifying observables for a phase transition in hot QCD

matter may prove to be a crucial feature of the model. There are two variables that are crucial for initialising and limiting the hydrodynamic evolution. The first transition from the initial (UrQMD) to the intermediate (hydrodynamic) stage is defined by the *start time*, t_{start} . The freeze-out condition, which is parametrized as an energy density (ϵ) criterion, is the second parameter that is related to the duration of hydrodynamic evolution [21, 22]. In this investigation, both these parameters are varied to investigate an important observable of HIC and is discussed in detail in chapter-4.

1.4 Observables of heavy-ion collisions

(Ultra)Relativistic heavy ion collisions are the collision of two lorentz contracted nuclei (clouds of nucleon) which are moving (in Center of mass frame) almost with the speed of light and collide at some point [24]. Such collisions might result in Quark-Gluon Plasma (QGP). This QGP matter then expands and subsequently at some favourable condition recombine/coalesce in hadrons again, which are detected by detectors. So, we started with hadrons and ends up with hadrons again. The entire process takes a time of the order of 10-15 fm/c [25]. It is therefore not possible to measure various parameters of the nuclear matter thus produced in such collision directly. One has to rely on indirect measurement of various signatures of different stages of heavy ion collision. Various observables related to heavy ion collisions are proposed to probe and characterize the exotic nuclear matter thus produced in such nuclear collision, to understand the particle production mechanism, their transport properties etc. The technique and purpose of measurement of a few global observables of heavy ion collision are discussed in detail in the following section-

1.4.1 Particle multiplicity

The total number of secondary particles (N), both charge and neutral, produced in a particular nuclear collision is defined as particle multiplicity of that event. It provides information about the rigorousness of nuclear collisions [26]. Multiplicity is directly related to collision geometry as well. Nuclear collisions can be characterized by using the term centrality and centrality is also parameterized by impact parameter (b). A large value of b means less central or *peripheral* collision where less number of particles will be produced. On the other hand, a *central* collision means least value of b and a huge number of final state particle production. The collisions that occur with impact parameter values between central and peripheral collisions are called *semi-central* collision. Most of the detectors generally detect charged particles and the term *multiplicity* is often synonymously considered as charged particle multiplicity (N_{ch}) [26, 27].

Studies on dynamical fluctuation in multiplicity is considered to be a very important aspect of high energy heavy ion collision studies as such dynamical fluctuations provide information about particle correlation and particle production mechanism.

1.4.2 Rapidity and pseudorapidity

The rapidity and/or pseudorapidity distributions are important indicators for the global reaction dynamics and kinematics of the system created in high-energy collisions [26]. According to the Landau hydrodynamic model, the rapidity density ($\frac{dN}{dy}$) or pseudorapidity density ($\frac{dN}{d\eta}$) is proportional to the entropy of the system and hence to the energy density produced in the collisions.

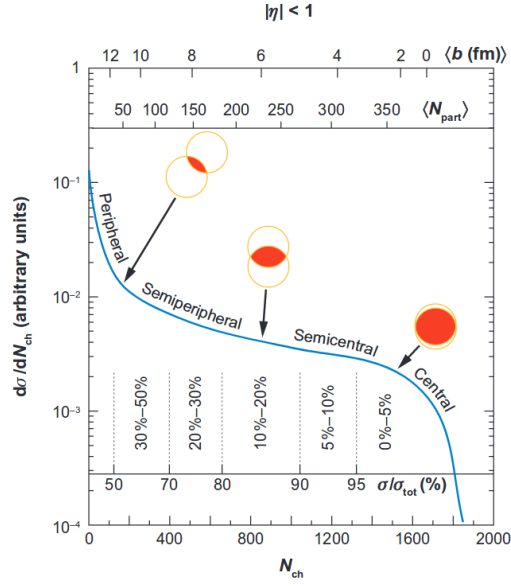


Fig. 1.3 Classification of events according to multiplicity for UrQMD simulated data at 40 AGeV Au+Au collisions [28].

If a particle is emitted with an angle θ with beam axis, then the mathematical formula of rapidity can be expressed as follows [28, 29]-

$$y = \frac{1}{2} \ln \left\{ \frac{E + P_L}{E - P_L} \right\} \quad (1.11)$$

Where, E and P_L are the energy and longitudinal momentum.

$$P_L = p \cos(\theta)$$

$$y = \frac{1}{2} \ln \left\{ \frac{\sqrt{m^2 + p^2} + p \cos \theta}{\sqrt{m^2 + p^2} - p \cos \theta} \right\} = \frac{1}{2} \ln \left\{ \frac{p \sqrt{\left(\frac{m}{p}\right)^2 + 1} + p \cos \theta}{p \sqrt{\left(\frac{m}{p}\right)^2 + 1} - p \cos \theta} \right\}$$

At ultra-relativistic energy, $p \gg m$. Hence, the value of $\left(\frac{m}{p}\right)$ will be negligible.

$$= \frac{1}{2} \ln \left\{ \frac{p + p \cos \theta}{p - p \cos \theta} \right\} = -\ln \left\{ \tan \left(\frac{\theta}{2} \right) \right\} = \eta \quad (1.12)$$

$$y \approx \eta = -\ln\left(\tan\frac{\theta}{2}\right) \quad (1.13)$$

η in terms of momentum can be written as [28]:

$$\eta = \frac{1}{2}\ln\left\{\frac{|p| + p_z}{|p| - p_z}\right\} \quad (1.14)$$

Without momentum, energy, and mass information the polar angle θ is the only variable to measure pseudorapidity. θ is independent of any mechanism of particle production in heavy ion collision [28].

The width of the rapidity distribution is considered to be a very important observable of HE-HIC as rapidity width provides information about the velocity of sound in the medium as well as the extent of scattering of various particles produced in nuclear collision.

1.4.3 Transverse mass and transverse momentum

The transverse momentum or transverse mass spectrum of the created particles is one of the most significant results of heavy-ion collision investigations because it provides essential information on the full space-time development of the system produced in a collision. Around 99 percent of the particles produced in heavy-ion collisions have a momentum of less than 2 GeV/c. The transverse mass distributions of identified particles (π , K , and p), for p-p and Au-Au collisions at $\sqrt{s_{NN}} = 200\text{GeV}$ are shown in Fig. 1.4 [30].

It is believed that the measure of mean transverse momentum ($\langle p_T \rangle$) or transverse mass (m_T) spectra is a viable tool for studying the QCD phase transition. Inverse slope of the p_T (or m_T)-spectra gives information about

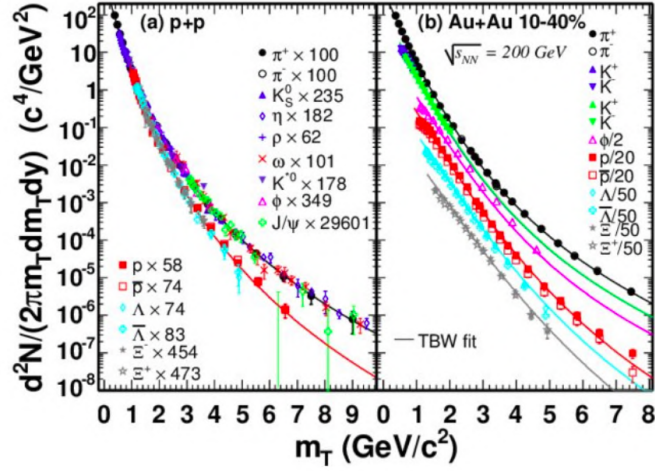


Fig. 1.4 Transverse mass spectra of identified particles at $\sqrt{s_{NN}} = 200 \text{ GeV}$ for $p - p$ and $Au - Au$ collisions [30].

the effective temperature (T_{eff}) of the expanding fireball, which in turn gives information about kinetic freeze-out temperature (T_k) as well as a radial velocity (β) of the matter produced in such nuclear collision. If there is a first order phase transition, it has been anticipated that the mean transverse momentum excitation function will exhibit a plateau like structure when plotted against total number of charged particle multiplicity. The flattening results from the system's temperature remaining constant while a hadron gas and QGP phase coexist i.e., when the system is in the mixed phase [28].

1.4.4 Nuclear modification factor

Quarks and gluons evolving in the system produced by ultra-relativistic heavy-ion collisions are predicted to experience radiative energy loss in the medium if the system evolves through a phase of deconfined colour charges. The nuclear modification factor (R_{AA}) is typically used as an observable of this energy loss. When properly normalised, the yield ratio in $A - A$ collisions to that in $p - p$

collisions at the same energy is what is meant by the term R_{AA} , as stated in refs. [31, 32]. The mathematical formula of R_{AA} is given by-

$$R_{AA} = \frac{1}{N_{coll}} \frac{\frac{d^2 N_{AA}}{dy dp_T}}{\frac{d^2 N_{pp}}{dy dp_T}} \quad (1.15)$$

where N_{coll} denotes the quantity of binary $A - A$ collisions.

There are three probable R_{AA} values. If $R_{AA} = 1$, that means the $A - A$ collisions are just a trivial summation of pp collisions. For $R_{AA} < 1$, this means that the parameter describes the impact of highly interacting matter in AA collisions, and $R_{AA} > 1$ indicates that the particle generation in $A - A$ collisions is boosted. The Fig. 1.5 shows the plots of nuclear modification factor as a function of transverse momentum. A suppression in particle yield in heavy ion collision at low and high p_T region is readily evident in these plots. The increase in R_{AA} values at intermediate P_T is considered as an indication of collective flow of the matter produced in such collision [26].

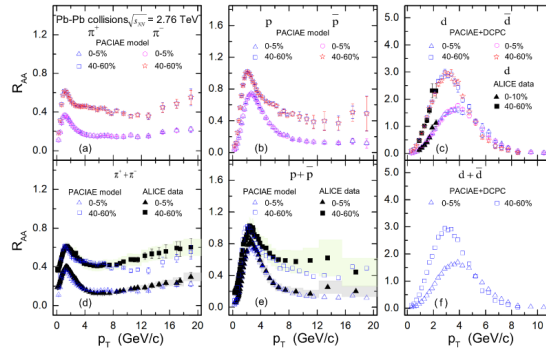


Fig. 1.5 The PACIAE + DCPC model calculates the nuclear modification factor (R_{AA}) as a function of p_T for various particle species in 0-5% most central and 40-60% peripheral $Pb - Pb$ collision events at $\sqrt{s_{NN}} = 2.76 TeV$. The ALICE data (solid markers) is used for the comparison and are shown in panel (c), (d) and (e). The shaded areas reflect the systematic uncertainty of the experimental data, and the vertical lines display the statistical uncertainty [32].

1.4.5 Multi-particle correlation

Large baryon density fluctuations are said to be capable of acting as a specific signal for the phase transition in the QCD phase diagram in heavy-ion collisions. If the system freezes out right near the critical point, it is anticipated that the critical density fluctuations arising due to multi-particle correlation will be visible as a power-law pattern on the available phase-space resolution. Calculations of Scaled Factorial Moment (SFM) of baryon number density can be used in high-energy experiments to determine the power-law or intermittency behaviour of the emission spectra of the charged secondaries. The details of SFM is rigorously described in the chapter-4.

1.5 Motivation of the present work

The operations for the Compressed Baryonic Matter (CBM) spectrometer at the Facility for Anti-Proton and Ion Research (FAIR) in Darmstadt, Germany, will be operational some times towards the end of this decade. In order to precisely define the phase diagram of nuclear matter and potential first or second order phase-transitions, the spectrometer seeks to carefully examine, in different phases, rare and bulk probes resulting from heavy ion reactions in the energy range $10 - 45 A GeV$. A time-of-flight (ToF) detector with a polar angular coverage of $2.5 - 25$ degree, that is set at a distance of $10 m$ from the target is the most crucial tool for hadron identification. According to simulations, the cell occupancy must be limited to $< 5\%$ while separating pions, kaons, and protons up to a few GeV/c momentum, which calls for a ToF resolution of $80 ps$ at high efficiency. The studies of physical observable at such unprecedented rate of $10 MHz$ using such a high efficient and wide acceptance Time of Flight (ToF) detector will be a

very important aspect of CBM experiment. It, thus, becomes very pertinent to undertake CBM-ToF simulation and physics performance studies to realize its applicability under high luminosity, high reaction rate, and particularly for central nuclear collision scenario. In this investigation, an attempt has therefore been made to identify light flavour hadrons, namely, pions (π^\pm), kaons (K^\pm), and protons (p, \bar{p}) with CBM simulation software for ToF detector and also to draw the m_T -spectra for this identified hadrons and hence to calculate the effective temperature of the system that would be produced in the CBM experiment through Au-Au collision at 10 $AGeV$.

Exploring the QCD phase diagram is one of the main goals of the relativistic and ultra-relativistic heavy-ion collision programmes. The overlapping region of the colliding nuclei can produce nuclear matter with temperatures and densities much higher than normal nuclear matter. It is possible that in relativistic heavy ion collisions, nuclear matter is created at vanishingly low or zero net-baryon density and extremely high temperature (RHIC and LHC), or at extremely high baryon density and moderate temperature (FAIR and RHIC-BES), depending on the collision energy and system under consideration. There are considerable experimental evidences that nuclear matter experience a type of hadronic to partonic phase transition in both the circumstances. According to lattice QCD calculations, a theoretical model that is quite successful in describing such high energy sub-atomic collisions the hadronic to partonic phase transition is of first-order type at high baryochemical potential μ_B (high net baryon density, $B - \bar{B}$), while the deconfined phase transition is of cross-over type at low μ_B (low net baryon density, $B - \bar{B}$). The QCD model calculation predicts, the cross-over and first-order phase transition have a critical end-point at roughly 160 MeV. However, the precise location of the critical point is yet to be ascertained, primarily due

to experimental challenges and model reliance. The experimental fingerprints linked to the critical point, according to hydrodynamic prediction, are most pronounced at beam energies between the AGS and top SPS energies. Therefore, it is very much important to investigate some key physics observables at such beam energies to realize QCD critical point. Further, another important aspect of (ultra)relativistic heavy ion collision studies is understanding the particle production mechanism. That is, how hadrons are being produced in such A-A collisions. In this work, an attempt has also been made, by analysing the hybrid UrQMD-hydro generated data for Au-Au collisions at 10 $A\text{GeV}$ to investigate the dynamical fluctuation in particle multiplicity that might have arisen due to the existence of a QCD critical point and/or due to different hadronization mechanism.

2

CBM simulation tools and detectors

2.1 Introduction:

The word *simulation* implies the imitation of a physical system. Simulation models are of much significance as they represent the key features of the selected system or

process. Computations are one of the main tools used to execute various simulations. Simulation is frequently done in nuclear physics before the real experiment [33, 34]. High energy particle and nuclear physics experiments are mainly focused on realizing several physics goals and are very much expensive and complicated due to their difficult design and the complexity of the process itself. Such a complex experiment generally consists of several sub-systems and sub-detectors. The goal of such an experiment may not be achieved if the design and performance of the sub-systems and sub-detectors are not perfect. Therefore, to achieve the best result, detailed simulation studies are immensely essential to the design and performance studies of detectors using simulation tools for individual detector systems.

The Facility for Anti-proton and Ion Research (FAIR) of GSI, Germany is a future HIC facility that is expected to be fully operational sometime during the last part of this decade and is designed to study nucleus-nucleus collisions from 10-45 $AGeV$ with high luminosity beam. This considered energy range is estimated to be relevant for studying the critical point of QCD phase diagram.

The CBM detector is a complex multi-detector system designed to cope up with interaction rates up to $10^7 Hz$ to enable measurements of rare observables and diagnostic probes of hot and dense fireball created in Au+Au collisions by identifying both hadrons and leptons created in such exotic events. The complex CBM detector system consists of: Micro-Vertex Detector (MVD), Silicon Tracking System (STS), Ring Imaging Cerenkov Detector (RICH), Muon Chamber (MUCH), Transition Radiation Detector (TRD), Time of Flight (TOF) detector, Electromagnetic Calorimeter (ECAL) and Projectile Spectator Detector (PSD) [35].

In this chapter, a detailed discussion about detectors and software tools used for CBM detector simulation will be discussed in details.

2.2 CBM detector system:

As mentioned above, the Compressed Baryonic Matter (CBM) detecting system composed of different sub-detectors with various purposes [36]. These sub-detectors are briefly described in the following sub-sections.

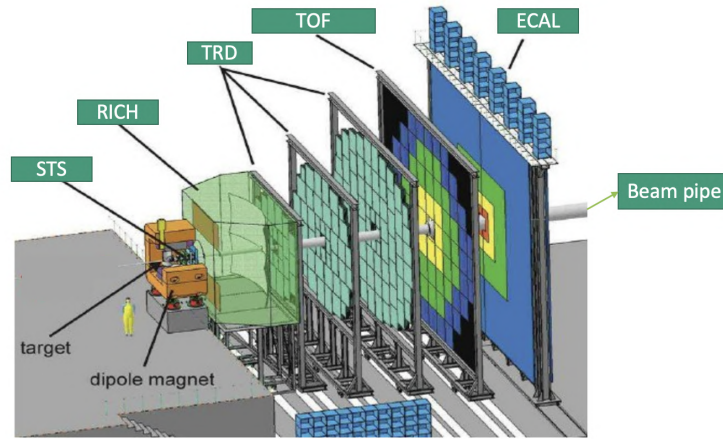


Fig. 2.1 Pictorial view of various detectors of CBM experiment [37].

2.2.1 Micro Vertex Detector

Micro Vertex Detector (MVD) [38] of CBM experiment will be used for secondary vertex determination (within 10 micro-meter scales). It is specially used in di-electron spectroscopy for background rejection and reconstruction of weak decays. Highly granular (pixel size $20 \times 20 \mu\text{m}^2$) silicon pixel detector will be used for this detector. Monolithic Active Pixel Sensors (MAPS) technology will be used to fulfill the high granularity and very thin (of the order of μm thickness) thickness requirement of MVD detector. MVD would be placed very close to the interaction vertex.

2.2.2 Silicon Tracking System:

The silicon tracking system (STS) [38] is the core component of the CBM experiment. It is comprising of 876 detector modules made out of double-sided silicon micro-strip sensors of various sizes: $6.2 \times 2.2 \text{ cm}^2$, $6.2 \times 4.2 \text{ cm}^2$, $6.2 \times 6.2 \text{ cm}^2$, $6.2 \times 12.4 \text{ cm}^2$. STS's function is to measure the momentum of produced particles in the nuclear collision. This requires large detector acceptance to cover rapidity from center of mass to beam rapidity. There are a few challenges in detecting the particles coming out from interaction vertex precisely. One of them is the required high track efficiency in a high track density environment. The other is the requirement of high hit rates for fast-tracking and precise measurement.

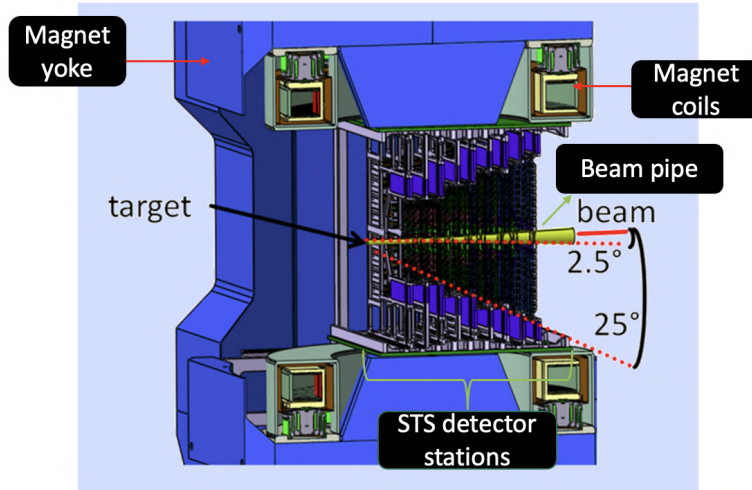


Fig. 2.2 Pictorial view of different parts of CBM-STS detector [39].

STS of CBM will be located inside the superconducting dipole magnet (1 *Tesla*) in a 2 m^3 volume. It will comprise of about 8 tracking stations and will be placed between 30 *cm* to 1 *m* downstream from the collision vertex. The STS shall work both in SIS100 with beam momentum 2 to 14 *AGeV* in the start-up phase of the CBM physics program and later on in SIS300 with beam energies 45 *AGeV* for heavy ion collision system (Au+Au). Interaction rates 10 *MHz* will be required to detect rare probes

from the beam-target interaction of Au+Au collisions. The typical track multiplicity produces in central Au+Au collisions is about 700 in the polar angular acceptance 2.5° to 25° . The full STS will be enclosed with walls of the thermally insulated component to allow the detecting operation of silicon sensors in a dry and cooled environment.

The pictorial representation of different sections or parts of STS is shown in the following Fig. 2.2.

2.2.3 Muon Chamber:

The study on low mass vector meson J/ψ , which consists of c and \bar{c} quarks, is very much important from the point of view that because of its short life time ($7.2 \times 10^{-21} \text{sec.}$) it decays into dileptons and as the leptons do not take part in strong interactions, it is believed that they carry the undistorted information of early state of nuclear collision. Thus, one of the aims of future CBM experiment is to detect J/ψ from leptonic decay channels. The Indian collaborators of CBM experiment have proposed the Muon Chamber (MUCH) [38] detector for identification of J/ψ from di-muon channel and would be responsible for the installation and functioning of MUCH detector at the FAIR site. The MUCH will consist of alternate absorbers and detector layers. It will have a number of stations (for SIS100: 4 detector stations and 4 absorbers, for SIS300: 5 detector stations and 6 absorbers) and each of them will have triplet of detector layers in between two consecutive absorbers. MUCH will be placed at a distance of about 1.25 m downstream from the beam interaction vertex and will extend about a 50° conical angle.

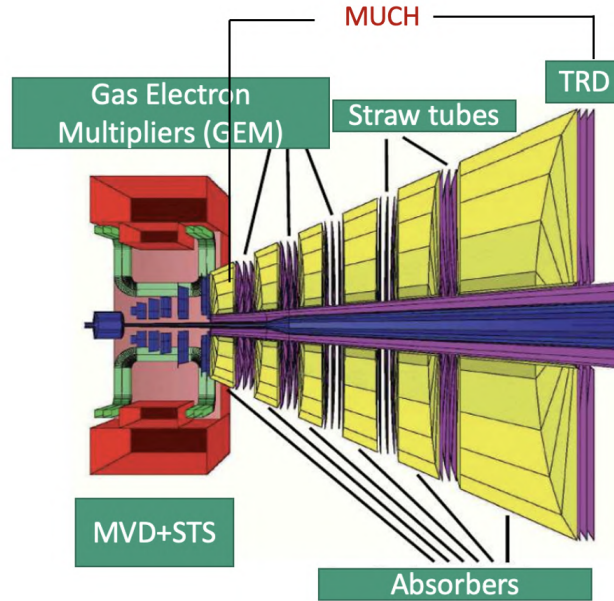


Fig. 2.3 Pictorial view of different parts of CBM-MUCH detector [40].

2.2.4 Ring Imaging Cherenkov Detector:

A Ring Imaging Cherenkov (RICH) [38, 41] detector of the proposed CBM experiment will be installed to identify electrons and positrons up to their momenta of about $8 \text{ GeV}/c$. RICH will be placed after the dipole magnet. Another separate detector Transition Radiation Detector (TRD) will be installed with it to separate electrons from pions at a higher momentum range. RICH will also be used in the detection of J/ψ particle. When MUCH will be collecting data, RICH will be sitting idle and vice-versa.

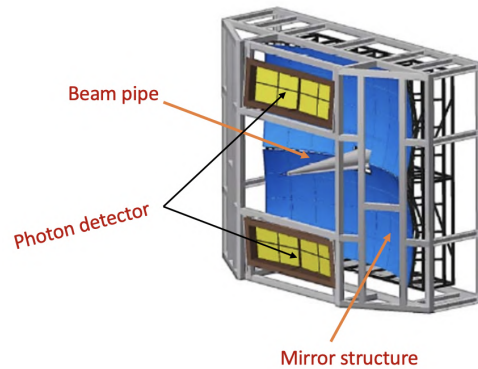


Fig. 2.4 Pictorial view of CBM-RICH detector [41].

2.2.5 Transition Radiation Detector:

The function of the Transition Radiation Detector (TRD) [38, 42] is to identify electrons and positrons with particle momentum greater than $1.0 \text{ GeV}/c$. In TRD, each station consists of four detector layers for SIS100 configuration and ten detector layers in three stations for SIS300 configuration. The TRD will be placed at about 4.1 m to 5.9 m downstream from the collision vertex [42]. The total active area of TRD detector is about 114 m^2 for the SIS100 setup.

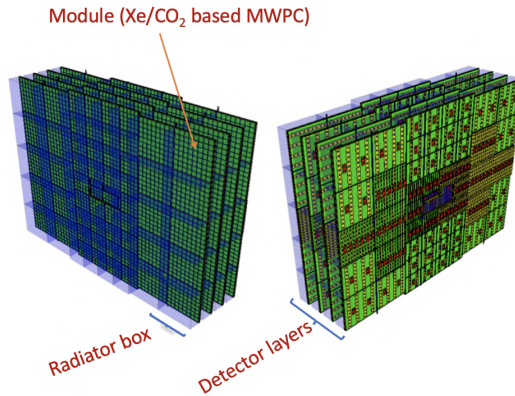


Fig. 2.5 Pictorial view of CBM-TRD detector [42].

2.2.6 Time of Flight Detector:

The time of Flight detector (TOF) [38, 43] consists of an array of multi-gap resistive plate chambers which are used for hadron identification via their time-of-flight measurement. The TOF detector covers an active area of about 120 m^2 and is located about 6 m downstream of the target for measurements at SIS100, and at 10 m at SIS300. The required time resolution is of the order of 80 ps . For 10 MHz minimum bias Au+Au collisions, the innermost part of the detector has to work at rates up to 20 kHz/cm^2 . Prototype MRPCs built with low-resistivity glass have been tested with a time resolution of about 40 ps at 20 kHz/cm^2 [43]. At small deflection angles the pad size is about 5 cm^2 corresponding to an occupancy of below 5% for SIS300 setup. ToF is generally used to identify hadrons, such as pions, kaons, and protons.

More details of CBM-ToF detector is provided in the next chapter (chapter-3).

2.2.7 Electromagnetic Calorimeter:

Electromagnetic Calorimeter (ECAL) [38, 44] of the CBM experiment will be used to identify and measure the energy and position of photons, and electrons. ECAL will

measure the photons spectra and spectra of photonic decay channels decaying from neutral mesons (π^0 , η). The ECAL consists of a total 140 layers of 1 mm lead and 1 mm scintillator, with cell size of $3 \times 3 \text{ cm}^2$, $6 \times 6 \text{ cm}^2$, and $12 \times 12 \text{ cm}^2$. The shashlik modules can be arranged either as a wall or in a tower geometry with a variable distance from the target. Calorimeter modules are grouped in two rectangular blocks which could be moved up and down (changing the angular range of measured particles and optimizing the experimental conditions for different colliding ion systems and beam energies) as illustrated in Fig. 2.6.

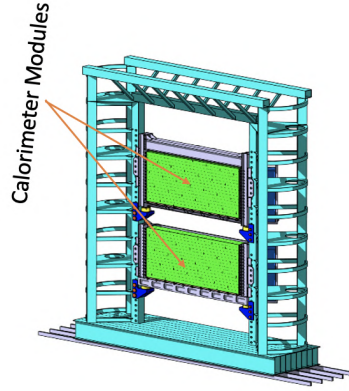


Fig. 2.6 Pictorial view of CBM-ECAL detector [44].

2.2.8 Projectile Spectator Detector:

The Projectile Spectator Detector (PSD) [38, 45] will be used in the CBM experiment at FAIR accelerator facility to determine such global event characteristics in A-A collisions as the centrality of the collision and the reaction plane orientation. The modular hadron calorimeter will allow to measure the energy of the projectile spectators and also transverse spectator coordinate for the reaction plane determination in each A-A collision.

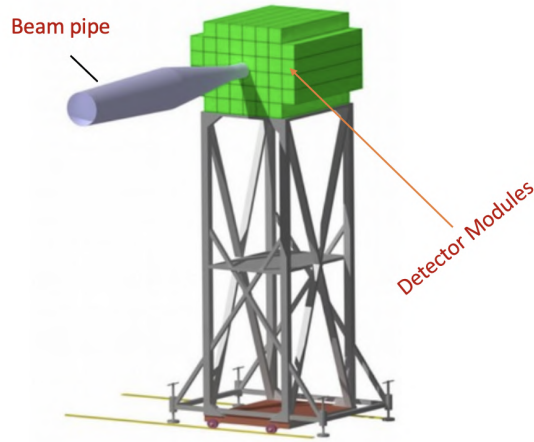


Fig. 2.7 Pictorial view of CBM-PSD detector [45].

The experimental estimate of global event characteristics in A-A collision such as the centrality of the collision which is related to the number of participating nucleons and the reaction plane orientation are challenging tasks in any high-energy heavy-ion experiment. In heavy-ion interactions the event-by-event determination of the collision centrality is used to study observables like collective flow, particle multiplicity and fluctuations which vary strongly with centrality. The collision centrality can be determined either by multiplicity of produced particles in the participant zone or by measuring energy carried away by the non-interacting nucleons (projectile spectators) and detected by forward hadron calorimeter. Moreover, the measurement of the number of projectile spectators and hence the total charge of projectile spectator fragments allows to estimate the number of participants and hence the impact parameter (b) of the collision.

2.3 Software Tools:

CbmRoot software is used to perform the simulation work of the present investigation. This software is a part of FairRoot software [46, 47]. The FairRoot is a ROOT-based

simulation and data analysis framework. Fig. 2.8 represents the structure of the full FairRoot framework [46, 47]. An interface for reading magnetic field maps and storage for event-by-event information regarding particle detection is also implemented.

The information regarding particle detection is stored in binary ROOT files. *CbmMCPPoint*, an interface class is provided to define the structure of registered hits (striking point) in a detector. All registered hits will be collected into dedicated lists, one list corresponding to one detector entity. The Root class *TTree* is used to organize the output data into an *ntuple*-like data structure. For the related analysis, the *CbmRootManager* provides methods to read these informations [47].

The event reconstruction and analysis software is organized into so-called tasks. The *CbmTask* is an abstract class that can be used to create specialized algorithms inheriting from it [38]. For each event, various tasks or reconstruction algorithms are created. Each task defines the relevant input data and parameters and creates its particular output data. The relevant input data and parameters are retrieved from the input file and the output data objects are stored in the output file.

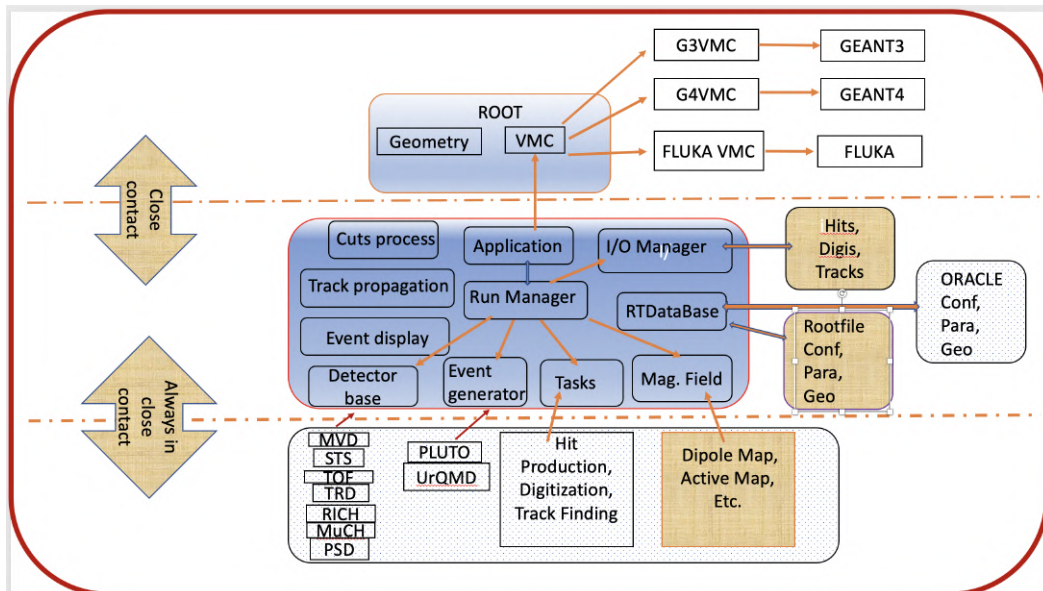


Fig. 2.8 Block diagram of FairRoot software framework [38, 47].

Simulation framework: For any simulation work, various external software is required. The required software for CBM detector simulation is mainly divided into two components:

- (a) Fairsoft (or external package), and (b) CbmRoot.

The structure of CBM simulation software in the form of a cartoon is depicted in Fig. 2.8.

2.3.1 FairSoft:

To perform CBM-ToF detector simulation, CBMROOT framework is used. The C++ based object-oriented ROOT analysis platform is used for the CBMROOT framework. The full detector simulation was performed within the framework of CBMROOT [46]. Several external generators were used for simulation works, which are supported by CBMROOT. The generators and algorithms which were used for the simulation are GEANT3 [48], GEANT4 [49] or FLUKA [50], by keeping the user code unchanged. It attributes full descriptions of the detector geometries and responses of the different sub-detectors of the CBM system and hence allows for the study of the various observables to check the realistic performance of CBM detectors. The overall CBM detector setup used here includes, apart from the ToF, STS as well as the beam pipe and the magnet. GEANT3 transport code is used to propagate model-generated particles.

ROOT: ROOT is a C++ based data analysis software framework broadly used by high energy physics researchers. The idea and design of ROOT software were initiated by Rene Brun and Fons Rademakers in mid-1990s. The major advantage of ROOT is that it can handle a huge volume of data efficiently. ROOT was developed in the context of the NA49 experiment at CERN [47, 51]. The basic functionality in ROOT is – histogramming, graph plotting, curve fitting, statistical tools for data analysis, four-vector as needed in high energy physics, matrix algebra, multivariate analysis,

interfacing Monte-Carlo event generators, 3D geometry visualization, etc. ROOT is, therefore, an inevitable part of CBM simulation and analysis.

Event Generator: The details of event generators have already been given in section 1.3. The event generators are the algorithms for Monte Carlo generation of nuclear collisions which are based on computer programs written in HLL. These are used to generate particles created in nuclear collisions at any chosen (SIS to LHC energies) energy range. The main inputs of this MC event generators are [52, 53],

- Matrix elements for different physical processes.
- Parametrized or experimentally measured cross-sections for various physical processes.
- Fragmentation functions etc.

The various event generators that are available with the FairSoft package are UrQMD [54, 55], UNIGEN [56], PLUTO [57] etc.

In our simulation work, the UrQMD event generator is used to generate Monte Carlo data and identify the light flavored particles using CBM Time of Flight detector. The effective temperature of fireball is then measured with the identified hadrons using transverse mass (m_t) distribution spectra, which is discussed in more details in chapter-3.

Libraries: GSL, [58] also known as GNU Scientific Library, is a set of software libraries needed for numerical computation that is also included in FairSoft. The distinct subject areas covered by GSL are - Complex numbers, special functions, statistics, interpolation, integral transforms, roots of polynomials, vectors and matrices, linear algebra, random numbers, Monte Carlo integration, differential equations, etc. CLHEP [59] or Class Library for High Energy Physics consists of several needed packages for high energy physics data analysis. The functionality included in CLHEP is vectors,

random numbers generation, matrix, geometry, etc. Boost [60] contains a set of libraries of C++. It also supports several functionality such as linear algebra, pseudorandom number generation, etc.

CbmRoot [61], on the other hand, is an experiment-specific code. Since virtual Monte-Carlo is incorporated in CbmRoot, the user code that creates simulated data does not depend on a particular Monte-Carlo engine. During simulation, the sensitive detectors (active components) provide the simulated data which are stored in the binary ROOT file on an event-by-event basis. The class *CbmMCPoint* is responsible for defining the structure of registered hits in a detector [62]. The output data is organized in the form of *ntuple*-like data structure with the help of the ROOT class called TTree [63]. During analysis, the class *CbmRootManager* could be utilized to read the various numerical parameters such as digitization parameters, geometry positions of the detector etc are needed for track reconstruction. The class *CbmRuntimeDb* is responsible for handling the parameter definitions. Different formats of inputs are supported in CbmRoot viz. Ascii, ROOT binary format and Oracle database input [47, 62].

FairRoot is a software framework based on ROOT which has been effectively used by CbmRoot for performing detector design simulation, track reconstruction, and online/offline data analysis. The basic structure of FairRoot is illustrated in Fig. 2.8. In this framework, a notoriously complex analysis task could be performed simply by making use of the task mechanism of ROOT framework. Although FairRoot was originally designed for CBM experiment, other upcoming experiments viz. PANDA, R3B, ASYEOS at GSI/FAIR, etc. have subsequently been using the FairRoot framework as the basis for their simulation, reconstruction, and analysis. The framework provides necessary arrangements to handle the classes responsible for performing simulation, reconstruction, handling of Input-Output (IO) files and building of necessary

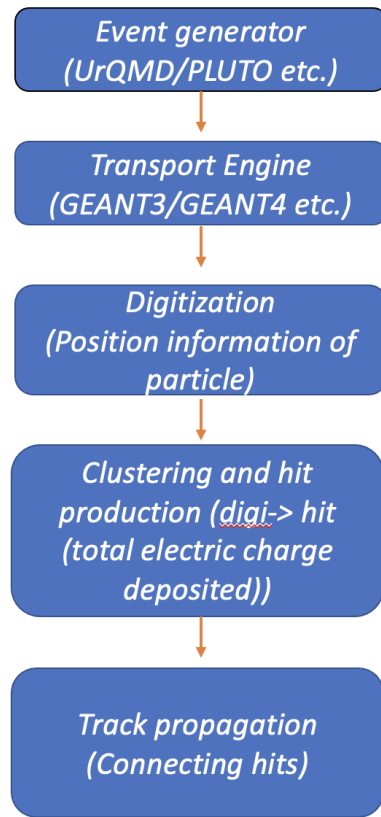
geometry. On the other hand, the framework manages the base classes to handle the detector-specific tasks e.g. defining magnetic field, Monte-Carlo event generators, and analysis. Run Manager, the main class of the framework executes (a) initialization (b) running event loops (c) handling IO with the help of IO Manager, and (d) handling parameters using runtime database (RTDatabase). During simulation, it also sets up the necessary environment and sends the information (regarding geometry definition, material, magnetic field, event generators, etc.) to the Virtual Monte Carlo application (Application) [47].

2.3.2 Simulation procedure:

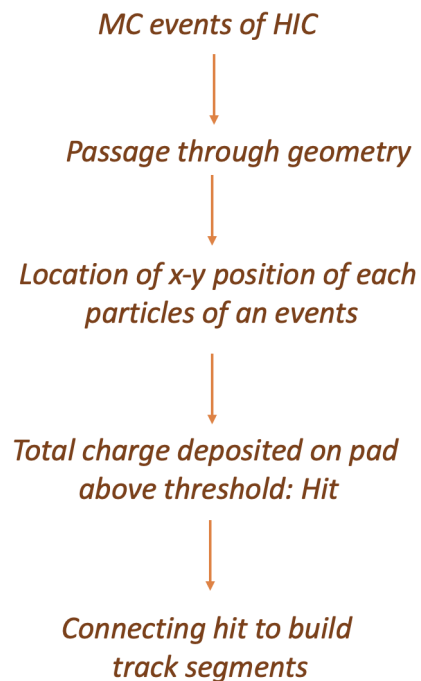
The simulation chain performed using the UrQMD event generator for input and GEANT3 transport engine can be summarized by the block diagram. As discussed briefly below it consists of the following fundamental blocks. (a) creation of a sample of minimum bias events of one's interest, (b) geometry implementation and detector response, (c) digitization (d) cluster and hit reconstruction and (e) Track reconstruction [38, 64]. The steps of simulation procedure is represented by the following block diagram in Figs. 2.9 (a) and (b).

Detector Response

The response model of the Micro Vertex Detector [38, 64] allows the simulation of clusters of pixels firing after the passage of a charged particle through the detector geometry. It also allows taking into account important effects such as the contribution of δ -electrons from the target and the pile-up of several collisions in the MVD. The STS detector response is also implemented here. STS detector response model [38, 64] includes all the physical processes related to the passage of a charged particle, from the charge generation in the detecting medium to the digital output signals. The simulation



(a)



(b)

Fig. 2.9 (a) The block diagram of the chain of the simulation procedure, and (b) the chronological order of CBM simulation procedure.

includes charge sharing between strips, charge collection inefficiency, Lorentz drift due to the presence of a magnetic field, channel dead time, and electronic noise.

Digitization:

GEANT3 provides the position of energy deposition inside the detector module. These locations along with the information of energy deposition taken together are called ToF points. To account for realistic detector geometry, the readout planes of the modules are segmented in pads for obtaining a final detectable response. The procedure of distributing the ToF-points to pads, known as digitization involves the procedure of implementing the response of the gas detector to the energy deposition inside the chamber. The procedure of digitization is mainly divided into two types- (a) simple, and (b) advanced digitization [38, 47, 65]. These digitization schemes are briefly described in the following.

(a) Simple digitization: According to simple digitization, *Digi* is the count of points on a given pad. In this type of digitization process, the detector responses are not included, so it is quite unrealistic for the detector simulation [47].

(b) Advanced digitization: In advanced digitization, the inclusion of detector response is considered. In this scheme, the total stored electric charge in each pad is calculated, and the amount of charge depends on the secondary electrons. In the advanced digitization scheme, random noise is added to make the simulation more realistic. If the total charge accumulation is greater than the threshold value, then it is counted as a *Digi*. Some of the other parameters have also been necessary to tune for precise simulation [47].

Cluster and hit reconstruction

The information stored in the *Digi* object is used to reconstruct the clusters of firing pads in the different detectors. For the MVD detector, the particle impact point is reconstructed by calculating the center of gravity of charge on the pixels belonging to a cluster. The output data type is called *Hit* and provides the coordinates of the reconstructed impact as well as the corresponding uncertainties. The hits are used to reconstruct particle trajectories. The STS detector algorithm provided that a strip has a signal of at least 4000 electrons, it is used to construct a cluster. Several adjacent strips are grouped in a cluster [38].

Track reconstruction

The track reconstruction in CBM is performed with the Cellular Automaton algorithm [64]. The technique builds segments of tracks, called triplets, by connecting hits in three consecutive detector planes of MVD and STS. Triplets are combined until a complete track is reconstructed. The algorithm provides the option to use the MVD in the track reconstruction procedure. In this case, the MVD detector planes are used in the same way as the STS planes. Priority is given to long tracks with momentum $p > 1\text{GeV}/c$ which point to the target. Next, tracks with lower momenta are addressed. When all possible hits have been assigned to tracks, the tracks are fitted with the Kalman filter method [64], which is a track fitting procedure used for the reconstruction of track parameters. The track fit algorithm first provides an approximate trajectory, which is extrapolated to all the surfaces to find intersections and to order and store all crossed surfaces. These ordered surfaces together with the hits are then used to modify the track parameters and covariance matrix taking into account multiple scattering and energy loss when a material surface is crossed [64]. The advantage of the Kalman filter method with respect to other methods, e.g., least squares, is that it allows to

the inclusion of noise and other inaccuracies in the calculation. In the case of track reconstruction, the Kalman filter allows to include the effect of multiple scattering of the particle in the trajectory.

3

Physics performance studies of CBM-ToF detector

3.1 Introduction

In relativistic heavy ion collisions, a system with high temperature and energy density is produced after the collision in the participant region. Due to the collisions of the nuclei almost the entire kinetic energy of the projectile is deposited in the overlapping region and a huge energy density and temperature is believed to be produced at the

collision vertex resulting what is called a *fireball*. If the temperature and energy-density exceed the critical value, the hadronic to partonic phase transition may occur. With the expansion of the fireball, the partons coalesce or recombine to reproduce hadrons again which will then collide inelastically among themselves to produce new hadrons and photons. The system continues to expand due to the pressure difference between the medium and surroundings and the temperature of the system continues to decrease. If the system temperature decreases and falls below a certain value at which the hadronic interactions become completely elastic and the production of new particles ceases, chemical freeze-out occurs. The temperature at which new particle production ceases, that is, at which chemical freeze-out occurs is known as the chemical freeze-out temperature (T_{ch}). On further expansion, the temperature of the system eventually reaches the kinetic or thermal freeze-out temperature (T_k) below which, the system dilutes to such an extent that the mean-free path becomes larger than the system size. Below T_k , the elastic collision between hadrons ceases and no change in the momentum of the particle is further expected. The particles then freely fly to fall onto the detector [47, 66].

Therefore, it is important to know the various thermodynamical properties of the fireball produced in heavy ion collisions. Different observables of heavy-ion physics are used to study the thermodynamical properties such as temperature, pressure, entropy, density, etc. of the fireball produced in nuclear collisions [67]. Some of the important observables are particle multiplicity, rapidity, transverse mass spectra, etc. Charged particle multiplicity is a measure of the rigorousness of collision, the largest multiplicity corresponds to the most central collisions that are most rigorous. It is also an important global observable of thermodynamic model of heavy ion collision that provides information about the entropy of the evolving system [68]. The rapidity distribution, on the other hand, is an important observable and it is an indicator of the

global reaction dynamics and kinematics of the fireball created in high energy heavy ion collision [69]. The transverse momentum/mass spectrum provides information about the entire space-time evolution of fireball created in nuclear collisions. The information about the evolving collision system, such as kinetic freeze-out temperature (T_k), radial flow velocity (β_T), etc. could be extracted from the transverse mass/momentum spectra of identified particles [70].

Transverse Collective Flow:

Just after the collision, the transverse velocity of the fluid is zero by symmetry. The pressure difference drives the expansion rapidly and builds up transverse velocities in the order of half of the velocity of light. Euler's equation of fluid acceleration for non-relativistic and for the generalized case are presented in equations 3.1 and 3.2 respectively [71].

$$\frac{dB}{dt} = -\frac{1}{\rho} \nabla p \quad (3.1)$$

$$\frac{dB}{dt} = -\frac{c^2}{\epsilon + \rho} \nabla p \quad (3.2)$$

Here, ϵ is the total energy density. Time scale associated with transverse collective flow is thus naturally of the order of the transverse size of the system, which gives rise to the gradients: any observables associated with transverse collective flow (p_T or m_T spectra, HBT correlations, elliptic flow) probes the system on a time scale which is essentially of the order of the transverse radius.

In this section, an important observable, transverse mass (m_T) spectra, will be discussed, which is usually used to characterize the transverse collective expansion of the fireball. Precisely, one tries to draw out from experimental data a quantitative details about the freeze-out temperature, T_k , and the transverse collective velocity, β_T , at freeze-out.

It is now well known that the transverse momentum or transverse mass spectra of various identified particles can disentangle thermal and collective motion of the constituent particles of the fireball.

Single particle P_T/m_T spectra: The four momenta of a massive particle of mass m is generally parameterized by the following form:

$$p^\mu = \begin{cases} E = m_T \cosh y \\ p_z = m_T \sinh y \\ p_T \end{cases} \quad (3.3)$$

Where E and y represent energy and rapidity respectively. p_z is the momentum of the particle in the z-direction, that is along the direction of the beam.

The mass-shell consideration $p^\mu p_\mu = m^2$ gives the relation $m_T^2 = p_T^2 + m^2$.

In nuclear collision, the particle production mechanism can be understood with the help of statistical model. A single particle energy distribution of hadronizing matter produced in such collision follows the Boltzmann form [73], which is represented as follows:

$$\frac{dN}{dp} \propto \exp(-E/T) \quad (3.4)$$

Where, T represents temperature variable.

For two-dimensional transverse system, $p_z = 0$, the energy E coincides with the transverse mass m_T . For a thermalized fluid at rest, neglecting the effect of quantum statistics, transverse mass distributions follow the following form:

$$\frac{1}{m_T} \frac{dN}{dm_T} = A * \exp\left(\frac{-m_T}{T}\right) \quad (3.5)$$

Where A is constant.

If one considers the longitudinal momentum (p_L), the expression of exponential is replaced by a more complicated function, which varies from the exponential behavior by powers of m_T .

Surprisingly, it came out that m_T -distributions of produced particles in nuclear collisions, are preferably well fit by such uncomplicated exponentials in m_T . If the motion of the system is collective transverse in type, the *inverse slope parameter* T obtained by fitting m_T spectra no longer corresponds to the exact temperature of the fluid. We therefore replace T by T_{eff} (effective temperature).

For simplicity, we consider a one-dimensional motion of a non-relativistic fluid to understand how T_{eff} is related to the fluid velocity β_T and temperature T . The particle velocity v in the fluid is the sum of two components, one is thermal velocity, v^* , and the other is fluid velocity β .

$$v = v^* + \beta \quad (3.6)$$

Then the average kinetic energy of a particle of mass m in the fluid is, therefore [28]:

$$\left\langle \frac{mv^2}{2} \right\rangle = \frac{mv^{*2}}{2} + \frac{m\beta^2}{2} \quad (3.7)$$

Due to the random orientation of thermal velocity, the cross term ($v^* \times \beta$) vanishes. For one-dimensional fluid, the thermal energy is related to temperature by the mathematical relation: $\frac{\langle mv^{*2} \rangle}{2} = \frac{T}{2}$ [28], whereas the average kinetic energy is related to the effective temperature T_{eff} of the collision system. The relation is represented by the following equation:

$$T_{eff} = T + m\beta^2 \quad (3.8)$$

Returning back to the m_T spectra in the nuclear collision, one may obtain a similar relation, with β replaced by the transverse velocity of the fluid β_T .

Two important lessons can be drawn from this equation 3.8. First, one can not easily disentangle the effects of thermal motion from collective motion using the spectra of a single species of particle; one only sees the inverse slope (equation 3.8) which is a combination of both thermal and collective expansions. Secondly, the inverse slope parameter T_{eff} increases with particle mass when collective expansion is present, so that collective expansion and thermal motion may be disentangled by comparing the spectra of different particles. A heavier particle is more sensitive to the collective fluid velocity than the lighter one.

The CBM detector is a complex multi-detector system designed to cope up with the interaction rates up to 10^7 Hz to enable measurements of rare observables and diagnostic probes of hot and dense fireball created in Au+Au collisions by identifying both hadrons and leptons created in such exotic events. The complex CBM detector system consists of a number of other sub-detectors such as MVD, STS, RICH, MUCH, TRD, TOF, ECAL, and PSD, the details of which are already discussed in section 2.2.

Particle identification is very important in the study of nucleus-nucleus collisions at all energies. Particle identification means identification of their mass, velocity/energy, and electrical charge. However, the mass of an elementary particle produced in A+A collisions can not be directly measured. The mass must be estimated from the measurement of momentum or otherwise from the velocity of the particle. It is known that the curvature of a particle in a magnetic field depends not only on its electric charge but also on its momentum. The principle of a magnetic spectrometer therefore rely on the measurement of a quantity called rigidity $R = \frac{p}{Z}$, where Z is the charge of the particle under investigation. The time of flight (ToF) detector, on the other

hand, rely on the measurement of flight time of a particle from interaction vertex to the detector.

A particle having mass m , say and momentum p has a velocity

$$\beta = \frac{p}{\sqrt{p^2 + m^2}} \quad (3.9)$$

where, $\beta = \frac{v}{c}$.

If L is the path length and T is the time that the particle will take to travel that path length L , then

$$T = \frac{L}{v} = \frac{L}{c \times \beta} \quad (3.10)$$

Since the path length L travels by different particles in ToF detector remains the same, two particle having different mass but the same momentum will have a time difference on travelling the same distance L . This time difference is given by,

$$\delta T = T_1 - T_2 = \frac{L}{c} \left(\sqrt{1 + \frac{m_1^2}{p^2}} - \sqrt{1 + \frac{m_2^2}{p^2}} \right) \approx (m_1^2 - m_2^2) \frac{L}{2cp^2} \quad (3.11)$$

The Time of Flight (ToF) detector is an array of Multi-gap Resistive Plate Chambers (MRPC) that will be used for the identification of hadrons in a time of flight measurement [74]. A module is a basic unit for the organization of ToF detector system. The modules comprised of MRPC counters, front-end electronics (digitizer, pre-amplifier, etc), gas-tight box enclosure, clock system, readout electronics, etc. Six different types of modules (M1, M2, M3, M4, M5, and M6) will be used for the ToF wall arrangement and is pictorially represented by Figs. 3.1 and 3.2. A total of 226 numbers of modules will be used for the whole ToF wall arrangement.

The module is composed of various components. In this section, some of the components are briefly described.

M6	M6	M5	M5	M4	M5	M5	M6	M6
		M5	M5	M4	M5	M5		
		M5	M5	M4	M5	M5		
M6	M6	M5	M5	M4	M5	M5	M6	M6
		M5	M5	M4	M5	M5		
		M5	M5	M4	M5	M5		
M6	M6	M5	M5	M4	M5	M5	M6	M6
		M5	M5	M4	M5	M5		
		M5	M5	M4	M5	M5		
M6	M6	M5	M5	M4	M5	M5	M6	M6
		M5	M5	M4	M5	M5		
		M5	M5	M4	M5	M5		
M6	M6	M5	M5	M4	M5	M5	M6	M6
		M5	M5	M4	M5	M5		
		M5	M5	M4	M5	M5		
M6	M6	M5	M5	M4	M5	M5	M6	M6
		M5	M5	M4	M5	M5		
		M5	M5	M4	M5	M5		
M6	M6	M5	M5	M4	M5	M5	M6	M6
		M5	M5	M4	M5	M5		
		M5	M5	M4	M5	M5		
M6	M6	M5	M5	M4	M5	M5	M6	M6
		M5	M5	M4	M5	M5		
		M5	M5	M4	M5	M5		
M6	M6	M5	M5	M4	M5	M5	M6	M6
		M5	M5	M4	M5	M5		
		M5	M5	M4	M5	M5		
M6	M6	M5	M5	M4	M5	M5	M6	M6
		M5	M5	M4	M5	M5		
		M5	M5	M4	M5	M5		
M6	M6	M5	M5	M4	M5	M5	M6	M6
		M5	M5	M4	M5	M5		
		M5	M5	M4	M5	M5		
M6	M6	M5	M5	M4	M5	M5	M6	M6
		M5	M5	M4	M5	M5		
		M5	M5	M4	M5	M5		
M6	M6	M5	M5	M4	M5	M5	M6	M6
		M5	M5	M4	M5	M5		
		M5	M5	M4	M5	M5		
M6	M6	M5	M5	M4	M5	M5	M6	M6
		M5	M5	M4	M5	M5		
		M5	M5	M4	M5	M5		
M6	M6	M5	M5	M4	M5	M5	M6	M6
		M5	M5	M4	M5	M5		
		M5	M5	M4	M5	M5		
M6	M6	M5	M5	M4	M5	M5	M6	M6
		M5	M5	M4	M5	M5		
		M5	M5	M4	M5	M5		
M6	M6	M5	M5	M4	M5	M5	M6	M6
		M5	M5	M4	M5	M5		
		M5	M5	M4	M5	M5		
M6	M6	M5	M5	M4	M5	M5	M6	M6
		M5	M5	M4	M5	M5		
		M5	M5	M4	M5	M5		
M6	M6	M5	M5	M4	M5	M5	M6	M6
		M5	M5	M4	M5	M5		
		M5	M5	M4	M5	M5		
M6	M6	M5	M5	M4	M5	M5	M6	M6
		M5	M5	M4	M5	M5		
		M5	M5	M4	M5	M5		
M6	M6	M5	M5	M4	M5	M5	M6	M6
		M5	M5	M4	M5	M5		
		M5	M5	M4	M5	M5		
M6	M6	M5	M5	M4	M5	M5	M6	M6
		M5	M5	M4	M5	M5		
		M5	M5	M4	M5	M5		

Fig. 3.1 Modules arrangement in ToF detector wall.

MRPC counter: The Multigap Resistive Plate Chamber (MRPC) is the most successful and widely used detector in high-energy nuclear physics experiments due to its excellent timing performance [77]. The CBM experiment requires higher time resolution and rate capabilities [77, 78]. For the Time of flight (ToF) detector of CBM experiment, MRPCs will be required to work at particle fluxes of order of $1-10 \text{ kHz/cm}^2$ at the outer region and $10-25 \text{ kHz/cm}^2$ at the inner or central region [74]. The rate capability is therefore a crucial factor for the MRPCs of the CBM-ToF detector.

Front-end electronics (FEE): The FEE is based on the PADI ASIC as a preamplifier and discriminator. The FEE will be placed near the read-out electrodes. To reduce the sensitivity to common-mode noise, the design of FEE is kept completely differential. Event-driven TDC ASIC GET4 is chosen for the digitization of the signal, which has been especially developed for CBM-ToF detector [74].

Clock system: CLOSY: a very accurate clock generation and distribution system has been designed for time measurements with the CBM ToF wall. In this system, the

frequency-synthesizer chip is the key factor of the main card or CBM-CLOCK-SYSTEM to create two independent phase-coupled output frequencies [74].

Readout chain: The readout chain has to supply adequate bandwidth to permit free-streaming of data taking even at the highest assumed rates. The necessity for the CBM-TOF system is a time performance in the order of or better than 80 ps. The design goal of CBM detecting system for time resolution in the order of 50 ps for the start time system leads to a requirement in the order of 60 ps for every individual channel of any counter and associated electronics. Pre-assuming that MRPC counters can reach timing performance as good as 50 ps, this leaves simply 38 ps for the electronics and associated clock system [74].

ToF detector will cover an area of 120 m^2 and the dimension of the ToF wall is 9 m high and 13.5 m wide. Also, the angular coverage of CBM-ToF detector is 2.5-25 degrees and the detector will be placed 10 m downstream from the collision vertex for SIS100 setup [74].

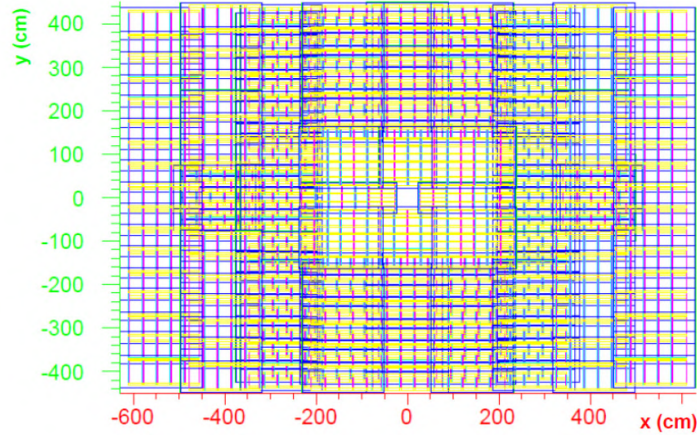


Fig. 3.2 Pictorial view of arrangements of MRPC in ToF detector wall.

In this chapter, an attempt has been made, through simulation, to evaluate the performance of CBM ToF detector in identifying the light flavoured hadrons namely, pions ($\pi^{+/-}$), kaons ($K^{+/-}$) and protons (p, \bar{p}) using ToF detector geometry of CBM

experiment and estimate their yields for Au+Au collisions at 10 AGeV using CBM FairSoft software. m_T -spectrum are then drawn and the inverse slopes of m_T -spectrum of identified particles are estimated to estimate the effective temperature (T_{eff}) of the system from the respective m_T -spectrum to evaluate the performance of the considered ToF geometry.

3.2 Method of particle identification

There are mainly two approaches of identification of charged hadrons using CBM-ToF detector and these two are- (a) Standard method or $n\sigma$ approach, and (b) Bayesian method. These two are briefly described in the following section.

- **Standard method:** In this work, the standard method or $n\sigma$ -approach of particle identification is adopted for the identification of π , K , and p with the CBM-ToF detector. According to this method, a particle is identified by measuring the time of flight. Time of flight depends on the measurement of momentum and velocity of the produced particles of nuclear collisions. The trajectory of the particle is reconstructed from the collision vertex to the Time of Flight (ToF) detector system, the measured time-of-flight allows to calculate the velocity β of the particle. Also, by measuring the momentum of the particle from STS tracks curvature, the mass of the particle can be calculated using the following mathematical relation [74, 75]:

$$m^2 = p^2 \left(\frac{1}{\beta^2} - 1 \right) \quad (3.12)$$

where, $\beta = c \times (\text{time of flight}(t) / \text{track length}(l))$

Generally, the time resolution σ_t of ToF detector dominates the error in the mass squared (m^2) over the contributions of momentum (p) and track-length (l) inaccuracies. Then, the error in m^2 is mathematically represented as:

$$\sigma_{m^2} = \frac{2p^2 \sigma_t}{\beta^2 t} \quad (3.13)$$

The error is independent of the mass of the particle (m) but it is a quadratic function of the momentum (p). Because of this dependence on momentum, the particle identification capability decreases with increasing momentum for an ideal detector system.

For quantitative particle identification, the two-dimensional probability density function (PDF) has to be written as the sum of the single-particle functions.

$$PDF(p, m^2) = \sum_{\alpha} PDF^{(\alpha)}(p, m^2) \quad (3.14)$$

The summation is for the contributions of pions, kaons, and protons. Mathematically, the single particle function has to be written as:

$$PDF^{(\alpha)}(p, m^2) = r_{\alpha} f_{\alpha,p}(m^2) \quad (3.15)$$

Where r_{α} is the momentum spectrum of identified particles (pions, kaons, and protons) within the detector acceptance and α represents the type of the identified hadrons. For visualization, assuming a completely Gaussian contribution of each identified particle with a momentum-dependent width:

$$f_{\alpha,p} = \frac{1}{\sqrt{2\pi}\sigma_{m^2}} \exp\left[-\frac{(m^2 - m_{\alpha}^2)^2}{2\sigma_m^2}\right] \quad (3.16)$$

- **Bayesian method:** According to the Bayesian approach, particle species identification depends on two parameters, one is the detector response and the other is particle abundance. PID from several detectors can be combined using the Bayesian technique; in actuality, simple selections based on separate PID signals from each detector do not fully utilize the detector's particle identification capabilities. Consequently, a Bayesian strategy can be used to maximize the PID capabilities of the detector. This method allows for the definition of a conditional probability $r(s|i)$ for a single detector to notice a PID signal in some other detector if a particle of type i is detected, where $i = (e, \mu, \pi, K, p\dots)$. The probabilities must then be folded with priors, which are the expected abundances of the particles. The probability $w(i|s)$ of the observed signal ' s ' for the particle i -type is determined using the Bayesian relation, and is represented by following formula:

$$\omega(i | s) = \frac{r(s | i)C_i}{\sum_{k=e,\mu,\pi,\dots} r(s | k)C_k} \quad (3.17)$$

Here, C_i is the priori probability.

A-priori probabilities are computed using a selection of events and tracks chosen in a particular physics study after calculating a detector response function, according to which each track is given an $r(s|i)$ value. When all priors are set equal, the condition is the simplest, but it can be found more precisely by using information from several detectors.

It is possible to accomplish the same thing by employing several detectors and computing the combined response function $P(s|i)$, which is the sum of the individual response functions:

$$P(s|i) = \prod r_\alpha(s_\alpha|i) \quad (3.18)$$

3.3 Results

In this work, the analysis has been carried out with UrQMD generated events at 10 AGeV central Au+Au collisions. The simulation and reconstruction works were carried out using the framework of the CBMROOT package.

The ToF is one of the core detectors of the upcoming CBM experiment which is capable of identifying all charged hadrons and will be used in all CBM experiments at SIS 100 [74]. As mentioned, the standard method has been adopted in this analysis for particle identification. In the standard method, m^2 of the charged particle is estimated using equation 3.9.

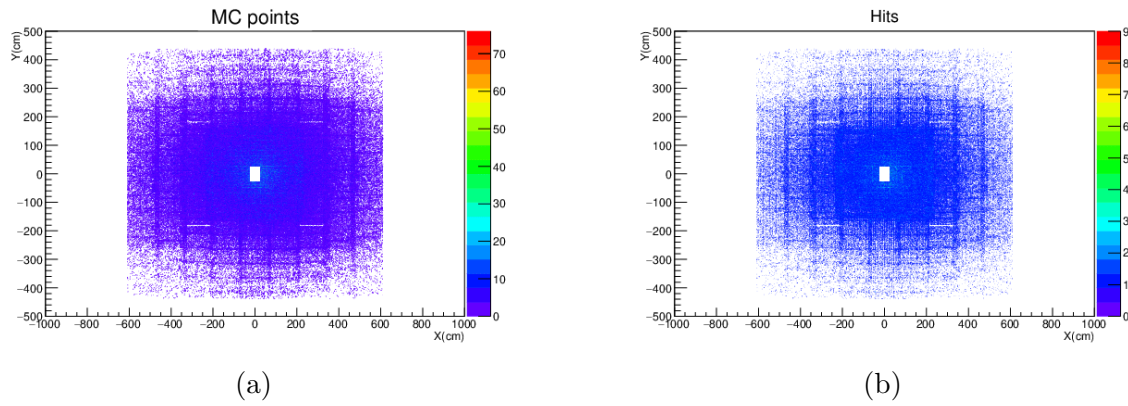


Fig. 3.3 (a) Monte Carlo (MC) points, and (b) hits distributions in time of flight detector wall.

In FAIR-CBM detector assembly, both MVD and STS will be placed in the gap of 1 T superconducting magnet [74]. The CBM simulation setup version *CbmRoot-JUN16* and *FAIRROOT-nov15p7* are used for this analysis. The details of setup and detector geometries are listed as follows:

- Detector setup: *sis100_hadron*.
- Event generator: *UrQMD*
- Target Element: *Gold (tar 197 79)*

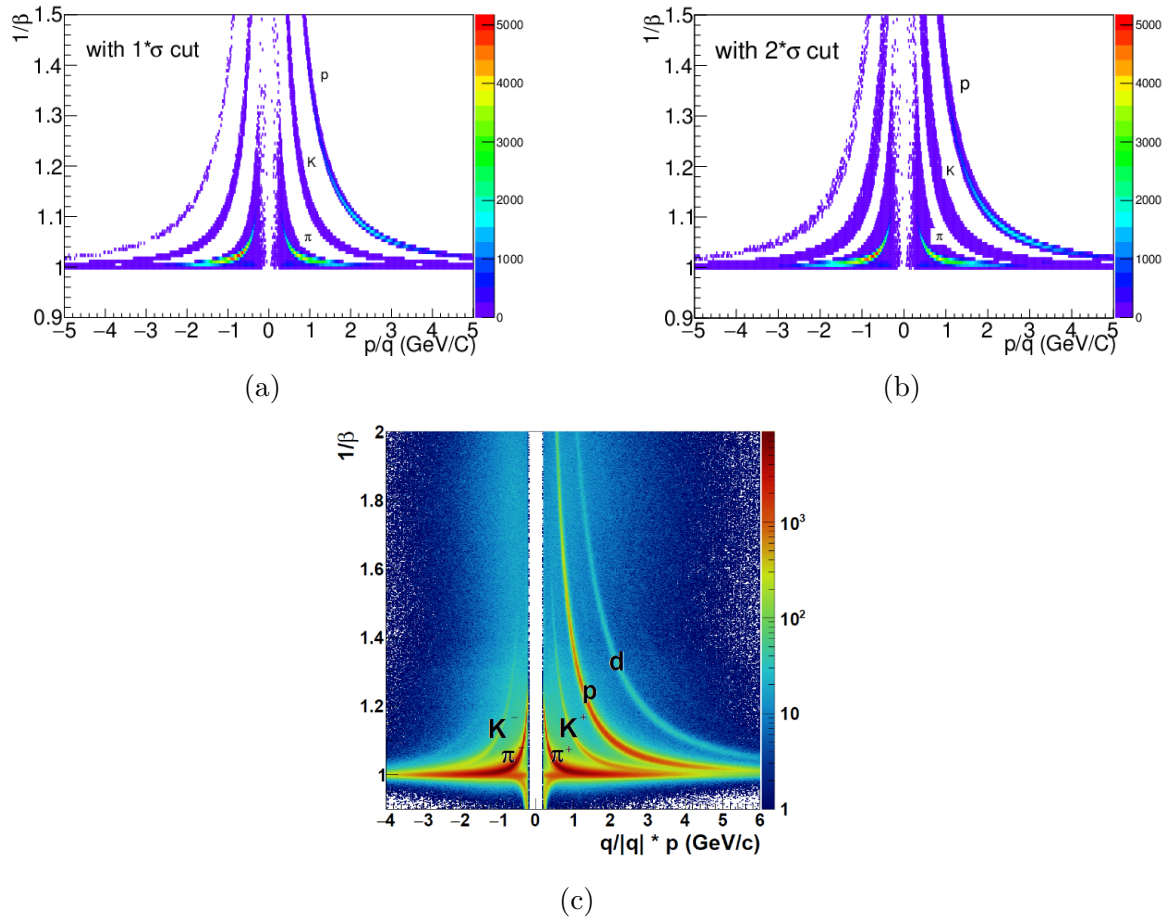


Fig. 3.4 $1/\beta$ vs. p/q plots for primary charged particles produced in Au+Au collisions at 10 AGeV beam energy with m^2 cuts (a) 1σ , and (b) 2σ . (c) published $1/\beta$ vs. p/q plot of I. Deppner and N. Herrmann for CBM collaboration [76].

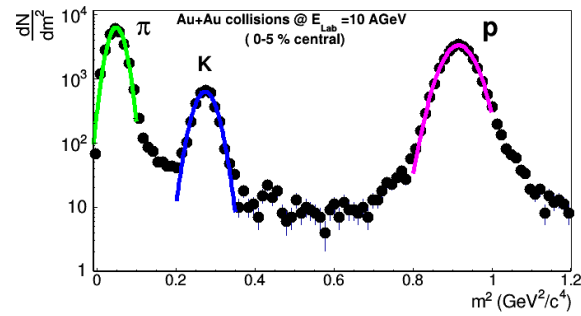


Fig. 3.5 m^2 distribution of primary particles produced in Au+Au collisions.

- Target Thickness: 0.025 cm
- Target Diameter: 2.5 cm
- Projectile Element: *Gold (pro 197 79)*
- E_{lab} : 10 AGeV
- Transport Engine: *GEANT3*
- Cave geometry: *cave.geo*
- Pipe geometry: *pipe_standard.geo*
- Magnet geometry: *magnet_v15a.geo.root*
- MVD geometry: *mvd_v15a.geo.root*
- STS geometry: *sts_v16x.geo.root*
- ToF geometry: *tof_v16a_1h.geo.root*
- Platform geometry: *platform_v13a.geo.root*
- PSD geometry: *psd_geo_xy.txt*
- ToF digi: *tof_v16a_1h.digi.par*

- ToF digibdf: *tof_v16a_1h_digibdf.par*
- MVD matbudget: *mvd_matbudget_v15a.root*
- STS matbudget: *sts_matbudget_v16x.root*

In Figs. 3.3(a) and 3.3(b), the QA plots for MC-points and hit distributions are shown. It is readily evident from these two plots that both the distributions are in good agreement. In Figs. 3.4(a) and 3.4(b) respectively, $1/\beta$ vs. p/q for different $n\sigma$ cuts are presented and compared with the published result of I. Deppner and N. Herrmann [76]. Fig. 3.5 represents the m^2 distribution plots for the identified π , K and p . It could be readily seen from Figs. 3.4(b) and 3.4(c) that with 2σ cut the time of flight geometry along with the selection criteria (track fit quality cut $\chi^2/(NDF) < 3$) used for this analysis agree well with published result of I. Deppner and N. Herrmann and can well be used to identify π , K , p up to the momentum of 2.5 GeV/c.

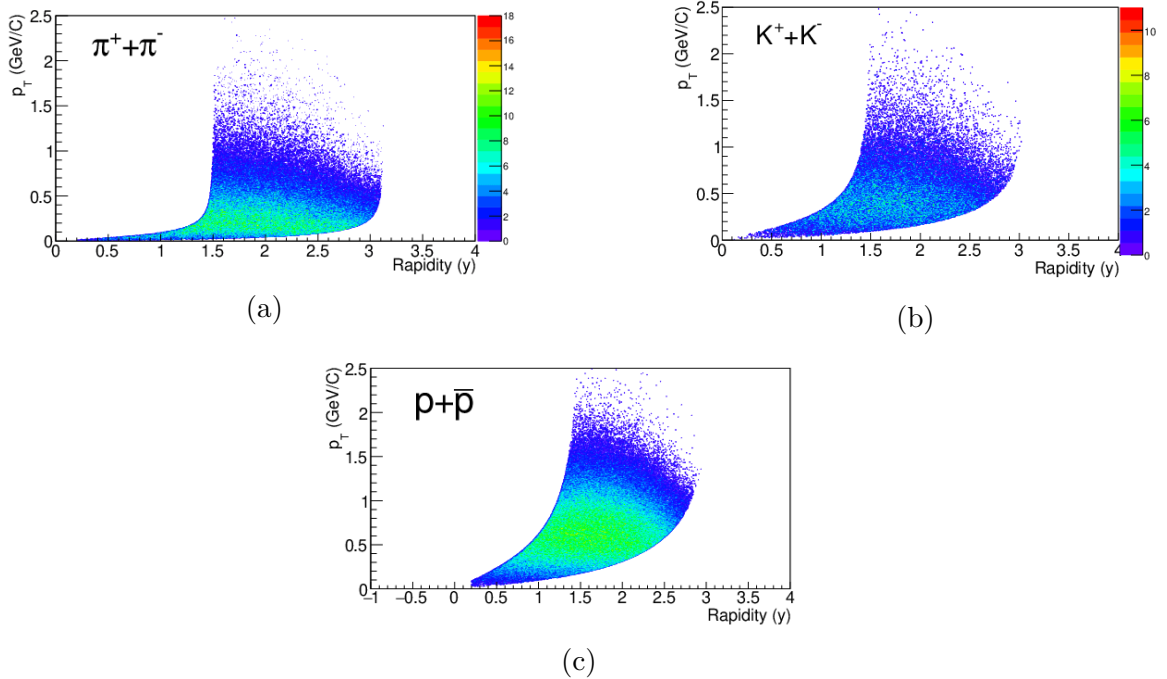


Fig. 3.6 y vs. p_T acceptance of CBM-ToF detector for (a) pions, (b) kaons, and (c) protons, produced in Au+Au collisions at 10 AGeV beam energy.

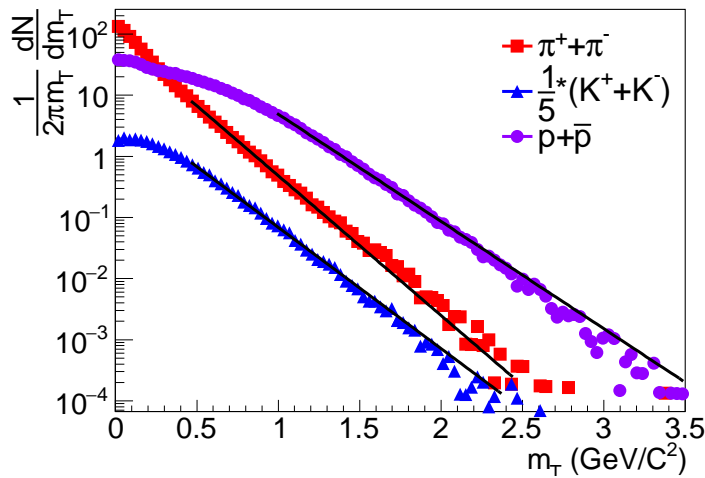


Fig. 3.7 m_T spectra of identified light flavored hadrons ($\pi^+ + \pi^-$), ($K^+ + K^-$), and ($p + \bar{p}$).

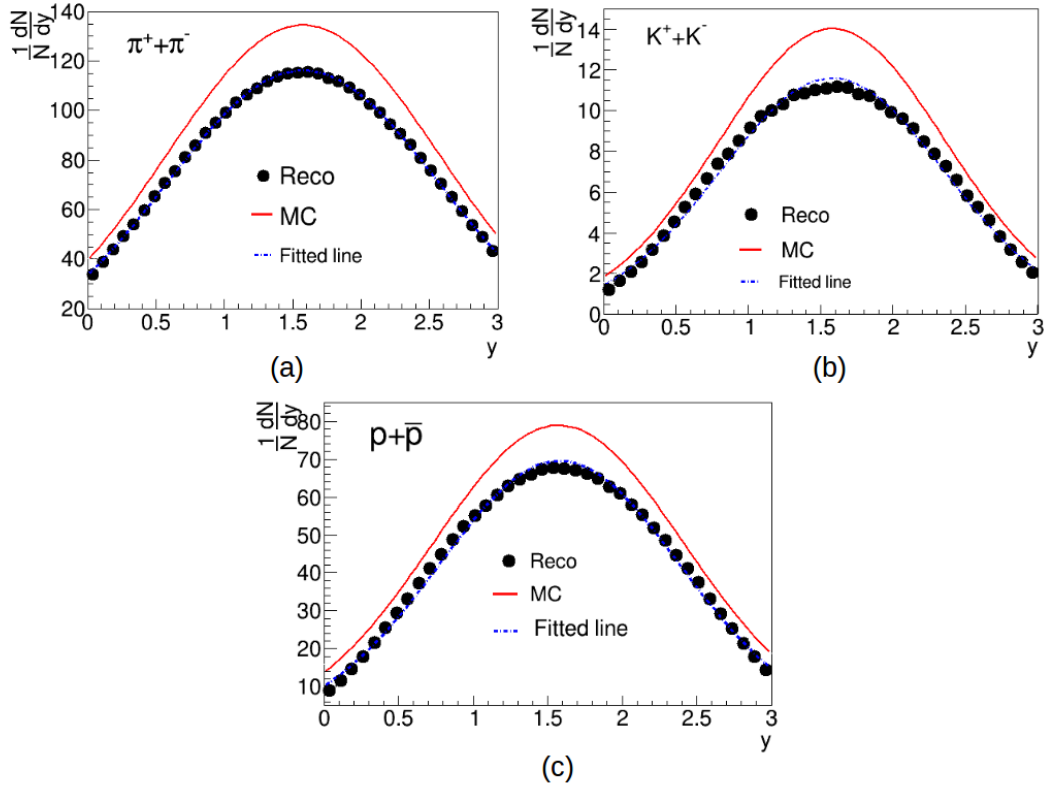
To have a check on the particle identification using the considered ToF detector geometry, yet another quality assurance plot is drawn, namely y vs. p_T plot and is shown in Fig. 3.6 for identified π , K , and p . All the identified particles are found to be fallen well within the expected $y - p_T$ acceptance for the system under consideration.

Fig. 3.7 represents the m_T spectra of the light flavored particles identified with considered ToF detector geometry and track selection criteria as described above. The solid lines represents the m_T spectra obtained for π , K , p using the equation 3.5. It could be readily seen from this plots that the obtained m_T spectra for π , k , and p identified with the considered TOF detector geometry follow the expected pattern. The values of the inverse slopes and χ^2/NDF as obtained from these plot for π , K and p are listed in table 3.1. It is interesting to see that the obtained temperatures follow the expected mass ordering.

Further, more accurate information regarding the extent of stopping achieved in such collision, as well as the history of the evolution of fireball can be found from the rapidity and transverse momentum distributions of the particles emitted in the collisions. Such plots are often used as more sensitive checks of a particular model's

Table 3.1 Inverse slope and χ^2/NDF for $(\pi^+ + \pi^-)$, $(K^+ + K^-)$, and $(p + \bar{p})$

Particles	Inverse slope(MeV)	χ^2/NDF
$\pi^+ + \pi^-$	185.10 ± 18.08	0.0542
$K^+ + K^-$	219.00 ± 25.44	0.0375
$p + \bar{p}$	247.00 ± 19.77	0.0734

Fig. 3.8 Rapidity spectra of identified light flavored hadrons $(\pi^+ + \pi^-)$, $(K^+ + K^-)$, and $(p + \bar{p})$.Table 3.2 Widths of the rapidity distribution of $(\pi^+ + \pi^-)$, $(K^+ + K^-)$, and $(p + \bar{p})$

Particles	Rapidity width
$\pi^+ + \pi^-$	1.9997 ± 0.0293
$K^+ + K^-$	1.6129 ± 0.0404
$p + \bar{p}$	1.5476 ± 0.0227

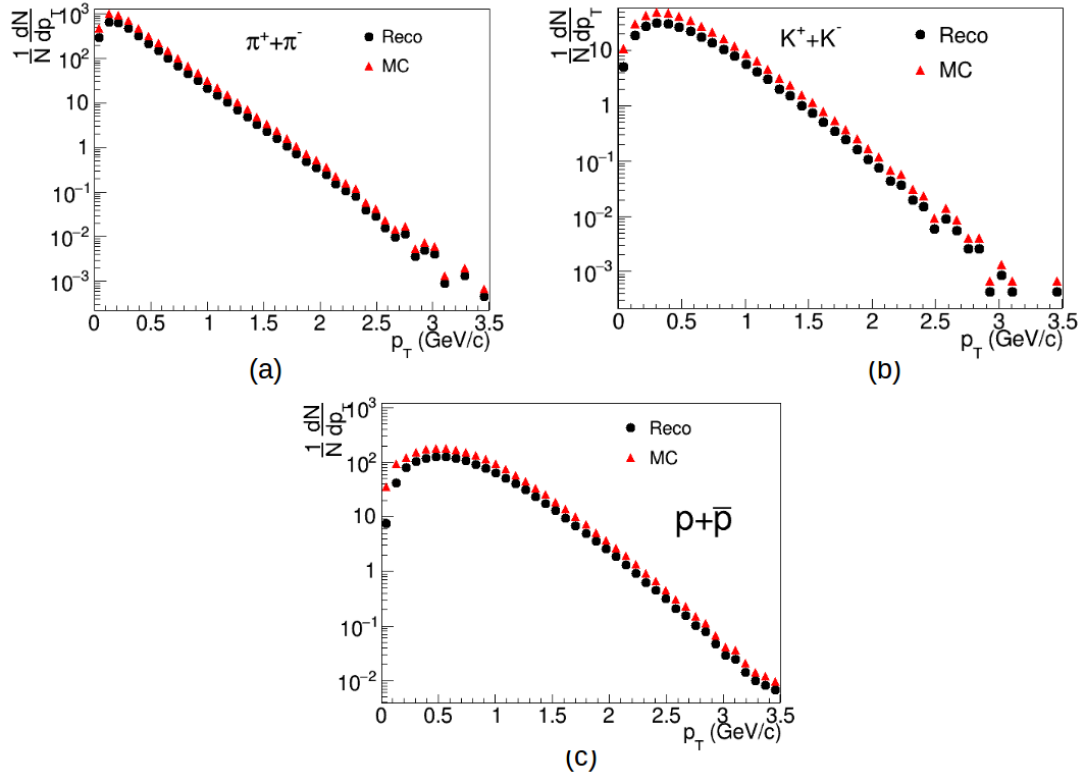


Fig. 3.9 p_T spectra of identified light flavored hadrons ($\pi^+ + \pi^-$), ($K^+ + K^-$), and ($p + \bar{p}$).

predictions viability. It was found that the rapidity distribution of proton peaks at about mid-rapidity, which is consistent with a high degree of stopping and thus high baryon density. The rapidity distributions and p_T spectra of pions, kaons, and protons identified with CBM-TOF detector with the above mentioned geometry are shown in Fig. 3.8 and Fig. 3.9 respectively. In Fig. 3.8, the solid lines represent the Monte Carlo (MC) (UrQMD generated) and the solid circles represent the reconstructed track (Reco) of ToF. The widths of the rapidity distribution spectra of the identified π , k , p are obtained with single gaussian fit and the values are listed in table 3.2. As could be readily seen from this table the rapidity width follows the expected kinematical mass ordering. In Fig. 3.9, the p_T spectra shown with solid circular points and the other one shown as solid triangular points are obtained respectively with reconstructed and monte

carlo (MC) π , k , p . As can be seen from Fig. 3.10 that the p_T dependent ratio of reco to MC of TOF detector remains greater than 80 % for the considered TOF geometry of this investigation. Therefore, from the results obtained from this investigation, it could be concluded that the TOF geometry considered in *tof_v16a_1h.geo.root* under *CbmRoot-JUN16* of *FAIRROOT-nov15p7* can well be used for identification of light flavored particle for the upcoming FAIR CBM experiment.

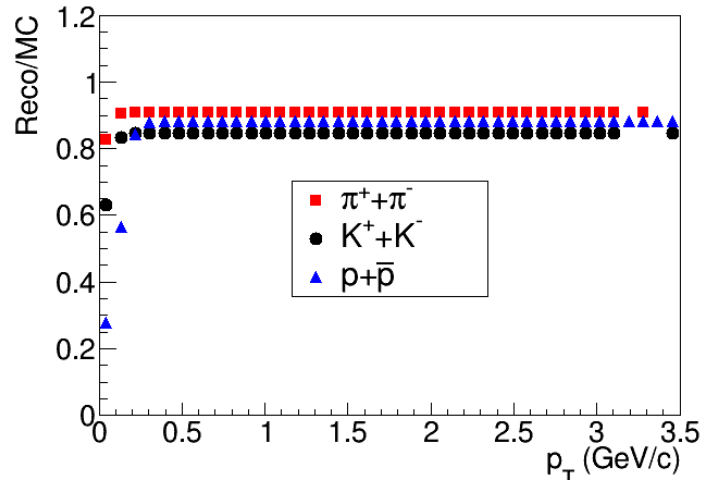


Fig. 3.10 p_T dependent efficiency plots of CBM-TOF detector for light flavored hadrons ($\pi^+ + \pi^-$), ($K^+ + K^-$), and ($p + \bar{p}$).

3.4 Summary

From the present study, it is seen that the ToF geometry, as considered in *CbmRoot-JUN16* and *FAIRROOT-nov15p7*, is quite successful in identifying light flavored particles π , K and p with $n\sigma$ -cut equal to 2 and track fit quality cut $\chi^2/(NDF) < 3$. The m_T -spectra for the identified particles follow the expected pattern. Even though the inverse slope parameters, as estimated from the present work, are found to be to some extent higher than the expected values, the mass ordering of the inverse slope is quite evident.

Further, the rapidity distribution of π , k , p shows maximum at mid-rapidity which indicates high baryon stopping and thus high baryon density. The widths of the rapidity distribution spectra of the identified π , k , p are found to follow mass ordering (table 3.2). The p_T spectra of TOF identified π , k , p are found to follow the expected Boltzmann distribution pattern. The ratio of reconstructed tracks to MC points is found to be more than 80 % over the considered p_T range of ToF. The considered TOF geometry of the present investigation, that is, *tof_v16a_1h.geo.root* under *CbmRoot-JUN16* of *FAIRROOT-nov15p7* can well be used for identification of light flavoured particles and related observables of HIC of FAIR CBM experiment.

4

Scaled factorial moment analysis of multiplicity fluctuation

4.1 Introduction

The lattice QCD is the most well established theory among non-perturbative approaches to QCD [79, 80]. This approach is applicable for low momentum transfer and uses a discrete set of space-time points known as lattice to reduce the analytically uncontrollable path integrals of the continuum theory to a very difficult numerical computation.

While it is a slow and resource-intensive approach, it has applicability into the strong forces acting between quark-quark and quark-antiquark pairs in a meson. Further, lattice QCD (lQCD) predicts, under some favourable conditions transition from the hadronic to partonic phase of matter, a consequence of asymptotic freedom feature of QCD interactions. The theory also predicts that the type of phase transition is of first order type at high baryon density and low temperature, and smooth crossover at high temperature and at low baryon density. According to QCD, at the end of the first order phase transition, there exists a critical point at which the phase transition is of 2^{nd} order.

In the vicinity of critical point, the thermodynamic variables such as entropy (S), specific heat (c_v), chemical potential (μ), compressibility (κ_T) etc are sensitive to slight change in order parameter and often exhibit a large scale fluctuation around the QCD critical point. In ref. [81, 82], the mathematical relationships between compressibility and susceptibility around critical point is shown. In this region, the quark matter density (n) is always finite but the susceptibility becomes large. This indicates that the system is easily compressible around critical point region.

The fluctuations of physical observables on an event-by-event basis have been used as basic tools for realizing QCD type phase transition. Since the fluctuations of physical observables, such as- (*i*) particle multiplicity, (*ii*) net-charge, (*iii*) strangeness, (*iv*) baryon numbers, (*v*) transverse momentum etc of heavy ion collisions are related to thermodynamic properties, in the following section, an attempt has been made to discuss the relation between thermodynamic properties and physical observables of heavy ion collisions.

Mathematically, the isothermal compressibility (κ_T) of a thermodynamic system can be defined as [83].

$$\kappa_T = -\frac{1}{V} \left(\frac{\delta V}{\delta P} \right)_T \quad (4.1)$$

where, V , T and P are the volume, temperature and pressure of the system respectively.

In nuclear collisions, the Grand Canonical Ensemble (GCE) properties may be considered to be true for experimental measurements near mid and central rapidity regions. According to GCE, the conserved quantum numbers here are exchanged with the rest of the system [83]. Also, according to GCE properties, the square of the variance is directly proportional to the isothermal compressibility of the system [84, 85], i.e,

$$\sigma^2 = \frac{k_B T \mu^2}{V} \kappa_T \quad (4.2)$$

where, μ and k_B are the mean multiplicity and Boltzmann's constant respectively.

The scaled variance is directly proportional to the compressibility (κ_T). The value of compressibility increases almost ten to hundred times at the critical point (T_c) region of the phase transition, and it is expected to have a power-law scaling with a critical exponent γ as,

$$\kappa_T \propto \left(\frac{T - T_c}{T_c} \right)^{-\gamma} \propto \epsilon^{-\gamma} \quad (4.3)$$

Here, the isothermal compressibility is proportional to the multiplicity fluctuations, and the fluctuation is expressed in terms of the scaled variances of the multiplicity distributions.

Moreover, κ_T is mathematically related to the susceptibility (χ_q) through the following relation-

$$\kappa_T = \frac{\chi_q(T, \mu)}{n^2(T, \mu)} \quad (4.4)$$

Therefore, it is easy to compress the thermodynamic system at the critical point region [81]. A number of the workers [82] have shown that, the quark-number susceptibility diverges at the critical point region which may be because of the sudden decrease of the interaction between the quarks-quarks and quarks-(anti)quarks after chiral symmetry restoration. The scaled variance (σ) is proportional to susceptibility (χ_q). So, through the study of multiplicity fluctuation it will be easier to search for the critical phenomena in the high-energy heavy ion collision experiments. The fluctuations of above mentioned quantities such as multiplicity, net-charge and mean transverse momentum fluctuation are briefly described in the following sections.

- **Multiplicity fluctuations:**

In statistical physics, the micro-canonical ensemble (MCE) represents the states of an isolated system where neither energy nor particles can be exchanged with the surroundings. For the canonical ensembles (CE), the energy can be exchanged until the system reaches equilibrium, but the particles can not be exchanged. Therefore, in the case of non-relativistic gases, the particle number is conserved in the micro-canonical as well as the canonical ensembles. For the grand canonical ensembles (GCE), equilibrium is achieved through the exchange of both the energy and the particle numbers.

The multiplicity fluctuations affect the other physical quantities of high energy nuclear collisions. Fluctuations of multiplicity are characterized by the following mathematical relation, which is the variance of multiplicity distributions.

$$\omega = \frac{\langle N_{ch}^2 \rangle - \langle N_{ch} \rangle^2}{\langle N_{ch} \rangle} = \frac{\sigma^2}{\mu} \quad (4.5)$$

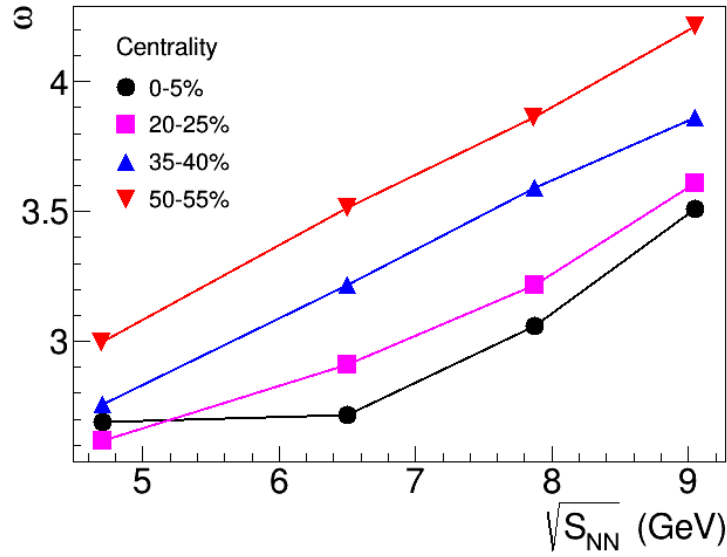


Fig. 4.1 The scaled variance ω against beam energy. The figure is taken from ref. [86].

where, $\mu = \frac{\sum N_{ch}}{n}$ -is the mean multiplicity, N_{ch} - is event multiplicity, n - is number of events, σ^2 - is the variance.

A larger ω value indicates the additional non-statistical fluctuations, a smaller value of ω might be a hint for a suppression of fluctuations. The Fig. 4.1 shows the energy dependence scaled variance ω for Au+Au collisions and as observed from the plot, the increase of scaled variance with energy is found to be a bit weaker for the central events.

Multiplicity fluctuation is the mixture of both statistical as well as non-statistical or dynamical fluctuation. The statistical parts come from the limited statistics, selection of centrality, beam energy, limited acceptance of the used detector, effects of rescattering etc [88, 89]. On the other hand, dynamical fluctuation arises from the inherent dynamics, such as presence of critical point, the particle production mechanism of heavy ion collision etc. In this chapter, multiplicity fluctuation will be discussed in detail in subsequent sections.

- **Net-charge fluctuations:** Net-charge fluctuation is one of the proposed signatures of existence of critical point of phase transition from hadronic matter to partonic matter. Charge fluctuations directly depends on square of the charges of the produced particles in nuclear collisions. One of the method of net-charge fluctuation is the calculation of $v_{(+-,dyn)}$. Mathematically, $v_{(+-,dyn)}$ is represented by the following relation [91]-

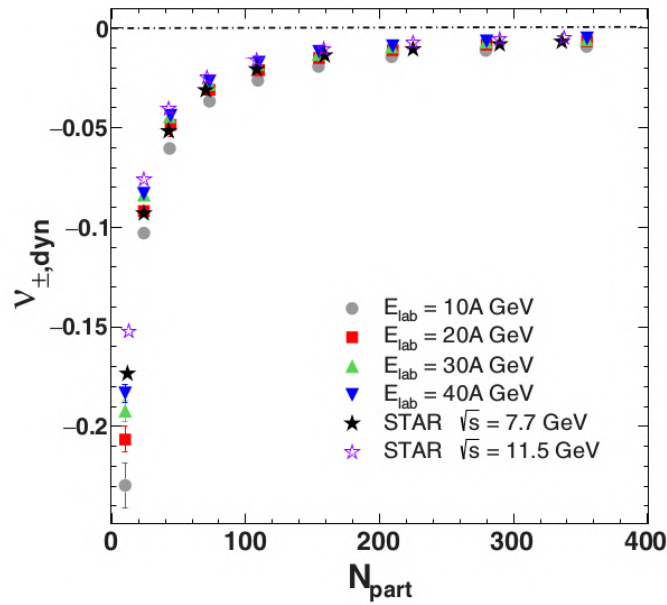


Fig. 4.2 Net-charge fluctuations, $v_{(+-,dyn)}$, of charged particles produced in Au+Au collisions at $E_{lab} = 10-40$ AGeV, and $\sqrt{S_{NN}} = 7.7, 11.5$ GeV as a function of number of participants, N_{part} . The plot has been taken from ref. [92, 93]

$$v_{(+-,dyn)} = \frac{N_+(N_+ - 1)}{\langle N_+ \rangle^2} + \frac{N_-(N_- - 1)}{\langle N_- \rangle^2} - 2 \frac{N_- N_+}{\langle N_- \rangle \langle N_+ \rangle} \quad (4.6)$$

where,

$\langle N_+ \rangle$ = average number of positively charged particles, and

$\langle N_- \rangle$ = averaged number of negatively charged particles.

The estimation of net-charge fluctuation $v_{(+-,dyn)}$ is actually constrained by the conservation of global charges, and the limited detector acceptance. The global charge conservation would lead to zero fluctuation, if each and every charged particles emerging from a collision are measured. Fig. 4.2 shows the centrality dependence of $v_{(+-,dyn)}$ distribution for Au-Au collisions at various energies. It is observed that the general trend of findings on net-charge fluctuations is somewhat comparable and consistent with one another. However, in ref. [93], it has been shown that, the plot of $v_{(+-,dyn)}$ against N_{part} for $E_{lab} = 10$ AGeV slightly differs from the same plot of other energies. This has been attributed to the more abundances of baryons over other charged particles.

- **Mean transverse momentum fluctuations:** One of the reasons for initial state fluctuations is the fluctuation of positions of nucleons, participating in heavy ion collisions. Initial state fluctuations evolves and it influences the fluctuations in final state observables. The average transverse momentum ($\langle p_T \rangle$) of final state particles for each and individual events depends on initial energy density fluctuation. Also it inversely depends on the area of the overlapping region [94]. Mathematically, the fluctuation in mean transverse momentum $\langle p_T \rangle$ is defined as [95, 96] -

$$\frac{\sigma(p_T)}{\langle p_T \rangle} = \frac{\sqrt{\langle (p_T - \langle p_T \rangle)^2 \rangle}}{\langle p_T \rangle} \quad (4.7)$$

An enhancement of mean p_T fluctuations showing up specifically in nuclear reactions might be related to non-trivial effects. It was predicted that mean p_T fluctuations can be enhanced if the system passes close to the QCD critical point [97]. The Fig 4.3 [98] shows the event-by-event fluctuations of the mean transverse momentum in

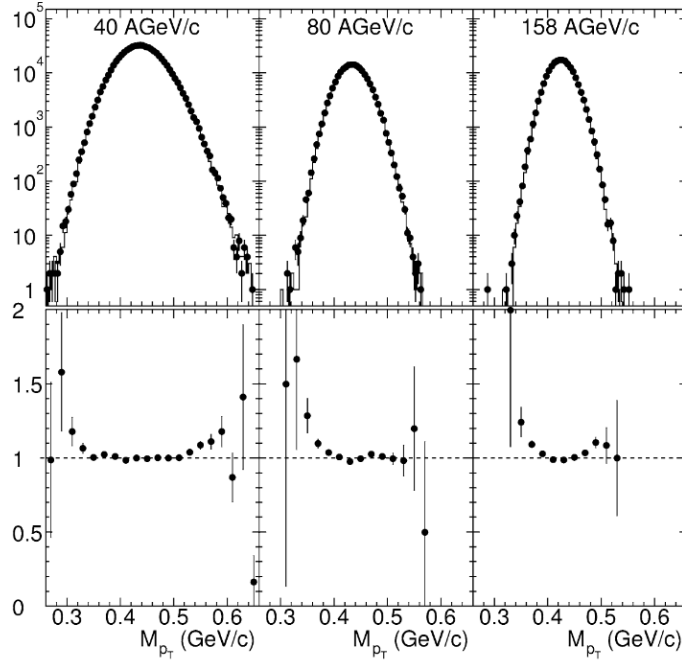


Fig. 4.3 Upper panel: Mean transverse momentum distributions at $E_{lab}= 40, 80$ and 158 AGeV/c. Data events indicated by circles and solid line represent the mixed events. Lower panel: The ratio between the distributions of data events to mixed events for all three energies. The plot has been taken from ref. [98]

Pb-Au collisions at 40, 80, and 158 AGeV. In these events at mentioned energies, the remarkable dynamical mean p_T fluctuations has been observed.

Out of above mentioned fluctuation studies, studies on multiplicity fluctuation is considered to be one of the most widely studied parameters of heavy ion collisions. In heavy ion collisions several mathematical tools exist to study multiplicity fluctuation. The effectiveness of any such method relies on the fact that how successful a particular technique is to disentangle the statistical component of fluctuation from the mixture of statistical and dynamical one. Scaled factorial moment (SFM) is considered to be one of the most sophisticated methods to separate dynamical fluctuations from the mixture of two. A power law behavior of factorial moment F_q on diminishing phase space bin width δw , or otherwise, on increasing number M of bins into which the phase space is divided, that is, $F_q \propto M^{\alpha_q}$ is termed as intermittency where the exponent α_q is called

the intermittency index and denotes the strength of intermittency. Intermittency is a property connected with the scale invariance of the physical process and was used first in connection with the turbulence burst in classical hydrodynamics [99–101].

The JACEE collaboration is pioneer in observing the large fluctuation in particle multiplicity in rapidity space in cosmic ray events and then in accelerator experiments. The application of SFM technique to JACEE events not only confirmed the presence of non-statistical fluctuation but also provided evidence for a power law dependence of fluctuation on phase space bin size. It is believed that in ultra-relativistic heavy ion collision, the existence of intermittent type fluctuation in density spectrum could be due to QGP type phase transition or due to cascading particle production mechanism [102]. The fluctuations at low energy nucleus-nucleus collision are also found to be of dynamical origin and exhibit intermittency in the emission spectra [103]. At CERN Super Proton Synchrotron (SPS), the NA49 and NA61 collaborations have performed the intermittency analysis with diverse collision systems. An intermittent type behavior has been observed for Si+Si collision at 158 AGeV energy [104]. Lately, the STAR collaboration of RHIC from the beam energy scan (BES) program conveyed the preliminary result of particle intermittency. The critical exponent obtained from intermittency index shows a minimum value in central Au+Au collisions at beam energy $\sqrt{S_{NN}} = 20$ to 30 GeV [105]. On the other hand, a number of workers [106, 107] with various model generated data for different systems have conducted intermittency analysis on their generated sets of MC data.

In ref. [106], the authors have studied the scaled factorial moment in $^{16}\text{O} - \text{AgBr}$ and $^{28}\text{Si} - \text{AgBr}$ interactions at 4.5 AGeV/c using UrQMD generated events. They found that the data produced with the UrQMD model exhibits only a weak intermittency for $^{28}\text{Si} - \text{AgBr}$ interaction. However, they could not observe any intermittent behavior in $^{16}\text{O} - \text{AgBr}$ interactions at 4.5 AGeV/c.

In recent findings on baryon density fluctuations in central Au-Au collisions at $\sqrt{s_{NN}} = 7.7, 11.5, 19.6, 27, 39, 62.4,$ and 200 GeV with STAR data, Jin Wu et al. [105] retrieved the energy-dependent intermittency indices. These energy-dependent intermittency plot displays a non-monotonic pattern with a peak around $20\text{-}27 \text{ GeV}$, showing that this energy range is where intermittency strength increases the most. They reported that UrQMD model is unable to explain the observed behavior without including the critical physics.

In this work, an attempt has been made to analyze UrQMD-hydro (in hydrodynamic mode) model generated data using scaled factorial moment technique to realize the presence of intermittency, if any, in the data sample and hence to assess if the hydro plays any role on the observed intermittent type of emission of particles produced in a nuclear collision. Keeping in mind the large acceptance of the upcoming Compressed Baryonic Matter (CBM) experiment of Facility for Antiproton and Ion Research (FAIR), Germany as well as the facts that 10 AGeV is the highest achievable energy for A-A collision at SIS100 of FAIR [108] and according to hydrodynamical calculation, the deconfinement phase border is first reached around 10 AGeV [109], the present investigation is carried out with 10 AGeV Au+Au collisions MC data.

4.2 UrQMD hydrodynamic model

Ultra-relativistic Quantum Molecular Dynamics (UrQMD) model is a transport model of relativistic heavy ion collisions. The detail description of UrQMD transport model is provided in chapter 2. UrQMD is a pure hadronic transport model, where a phase transition to a quark-gluon state is not incorporated explicitly into the model dynamics. However, a detailed analysis of the model in equilibrium yields an effective EoS of Hagedorn type. It is one of the most successful model to describe the particle yields, transverse momentum spectra of identified particles in nucleus(A)- nucleus(A),

hadron(h)-hadron(h) and hadron(h)-nucleus(A) collisions [110–112]. However, it is comparatively less successful as -

- The values of elliptic flow above SPS energy range are too small.
- Baryons with strange and multi-strange quark contents are not produced in sufficient amounts.
- Hanbury-Brown Twiss radii hint to a very small ratio of outward radius (R_o), to sideward radius (R_s).

So, the purely hadronic transport approach may not be enough to explore the dynamics of hot and dense matter produced in nuclear collisions. Therefore, the relativistic hydrodynamic description is required for these nuclear reaction framework, and coupled with hydrodynamic description to transport approach and naming as hybrid UrQMD-hydrodynamic model is introduced. In this hybrid model, microscopic transport calculation for initial condition and freeze-out procedure is implemented with intermediate hydrodynamic calculations.

The UrQMD transport model is used to calculate the initial state of a heavy ion collision followed by hydrodynamical evolution [22]. This is necessary to account for the nonequilibrium nature of the very early stage of the collision. Event-by-event fluctuations of the initial state are naturally included in this setup. The coupling between the UrQMD initial state and the hydrodynamical evolution takes place when the two Lorentz-contracted nuclei have passed through each other. The initial time to begin the hydrodynamical evolution is calculated by the following equation:

$$t_{start} = 2R\sqrt{\frac{2m_N}{E_{lab}}} \quad (4.8)$$

Where, R is the nuclear radius, m_N is the nuclear mass, and E_{lab} is the beam energy in laboratory frame.

Moreover, the equation of state (EoS), the pressure as a function of energy, and net baryon number density are needed as inputs to solve the hydrodynamical equations. Since the exact EoS of hot and dense QCD matter is still not specifically known, it may seem disadvantageous to have this additional uncertainty in the model. Nonetheless, it may prove to be an important trait of the model to be able to study changes on the dynamics of the bulk matter when changing the EoS, thus finding observables for a phase transition in hot QCD matter. The equations of state, which are used for the evolution with phase transition are hadron gas (HG) EoS, Chiral EoS, Bag model EoS etc. Moreover, evolution of the hydrodynamic part is defined by transition energy density (TED) and hydrodynamic cells in the model framework are converted to particles at the end of the evolution with a Cooper-Frye method. The final stage of evolution is handled by the UrQMD hadronic cascade approach.

4.3 MC data generation using High Performance Computing Cluster(HPCC)

For the present investigation, different sets of UrQMD-hydro data have been generated using high performance computing cluster (HPCC) of Nuclear and Radiation Physics Research Laboratory (NRPRL), Department of Physics, Gauhati University. The HPCC cluster contains four blade servers of which one is used as master and other three as slaves. In this cluster system, rock-7.0 cluster software and CentOS 7.6 operating system have been implemented to do our jobs in a smoothly and efficient way. The system consists of total 84 nodes and 168 numbers of threads. Such a high configuration provides us an opportunity to do our jobs with a reasonable speed. An external storage system of 20 TB was connected to the HPCC to store MC data. The

pictorial view of HPCC of our laboratory is shown in Fig. 4.4. A computer program is written for parallel processing of the events using this HPCC facility.



Fig. 4.4 Pictorial view of high performance computing cluster (HPCC) of NRPR laboratory, Department of Physics, Gauhati University.

4.4 Mathematical formalism of scaled factorial moment analysis

The Scaled Factorial Moment (SFM) technique is considered to be one of the most successful and widely accepted mathematical tool to extract and analyse dynamical fluctuation from the mixture of statistical and dynamical fluctuations. Over last four decades, a large number of workers have applied this technique on a various system at different energies and observed a clear evidence of power law behavior of the emitted particles over phase space under investigation [113, 114].

In the study of intermittency in one dimension, a pseudorapidity interval $\Delta\eta$ is divided into M bins of equal width $\delta\eta = \frac{\Delta\eta}{M}$, where η is defined as $\eta = -\ln(\tan(\theta/2))$. Here, θ is the polar angle of each emitted charged particle of an event and is estimated as $\theta = \cos^{-1}(p_z/p)$.

If n_m be the number of particles in the m^{th} bin, where m can take any value from 1 to M (=10, say), the factorial moment f_q of order q is defined as [114, 115]-

$$f_q = \langle n_m(n_m - 1)\dots(n_m - q + 1) \rangle \quad (4.9)$$

If the averaging in the above equation is performed over all events for a fixed bin, the procedure is called vertical averaging and gives fluctuation in event space. On the other hand, if n_m is averaged over all bins for a fixed event, it is called horizontal averaging and provides information on fluctuation in phase space.

Assuming that the statistical contribution to the fluctuation in the spatial distribution of the charged particles is Poisson distributed, Bialas and Peschanski showed that the factorial moments of the multiplicity distribution of the entire sample of events are equivalent to the moments of the corresponding dynamical part only, irrespective of the nature of the statistical component [114, 116]. In either method of averaging, if the probability distribution P_n of n_m can be expressed as a convolution of dynamical distribution $D(\nu)$ and the statistical (Poissonian) distribution, f_q is shown to be a simple moment of $D(\nu)$, the statistical component is regarded as having been filtered out by f_q estimation [117].

For a single event, the q^{th} order scaled factorial moment is defined as-

$$F_q = M^{q-1} \sum_{m=1}^M \frac{n_m(n_m - 1)\dots(n_m - q + 1)}{n(n - 1)\dots(n - q + 1)} \quad (4.10)$$

where, n is the multiplicity of an event. Thus, $n = \sum_{m=1}^M n_m$.

For an ensemble of events having varying multiplicity, the expression for scaled factorial moment is modified as-

$$F_q = M^{q-1} \sum_{m=1}^M \frac{n_m(n_m - 1)\dots(n_m - q + 1)}{\langle n \rangle^q} \quad (4.11)$$

where, $\langle n \rangle = \frac{\sum_1^{N_{ev}} n}{N_{ev}}$, N_{ev} is the total number of events of the population.

The horizontally averaged normalized or scaled factorial moment is then expressed as-

$$\langle F_q \rangle = \frac{1}{N_{ev}} \sum_{i=1}^{N_{ev}} M^{q-1} \sum_{m=1}^M \frac{n_m(n_m - 1)\dots(n_m - q + 1)}{\langle n \rangle^q} \quad (4.12)$$

In log-log plot, a linear increase of scaled factorial moment $\langle F_q \rangle$ with decreasing bin width $\delta\eta$ or otherwise, increasing number of bins M into which the pseudorapidity space is divided confirms the power law behavior of the form $\langle F_q \rangle \propto M^{\alpha_q}$, thereby indicating the intermittent pattern of emission of particle in a nuclear collision.

Intermittency, in turn, is related to self similarity and fractal behavior of the emission spectra [114, 118–120]. The anomalous fractal dimension d_q ($= D - D_q$, where D and D_q are ordinary topological dimension and generalized fractal dimension respectively), is related to intermittency index α_q through the relation

$$d_q = \frac{\alpha_q}{(q - 1)} \quad (4.13)$$

A study on the order q dependence of d_q is quite informative about the particle production mechanism. It is claimed that an increase in d_q with q is associated with particle production via some branching mechanism. An order independence of d_q , on the other hand, is indicative of particle production via a phase-transition.

The intermittent behaviour exhibited by the emission spectra of particles of heavy ion collision may also be a projection of non-thermal phase transition that occurs

during the evolution of the collisions, which in turn, would be responsible for the occurrence of the anomalous events. The presence of a non-thermal phase transition is characterized by a quantity λ_q , related to the intermittency index α_q , through the relation 4.1 and is expected to have minimum value at some $q = q_c$.

$$\lambda_q = \frac{\alpha_q + 1}{q} \quad (4.14)$$

The value of q_c need not necessarily be an integer and the region satisfying the condition $q < q_c$ may be dominated by many small fluctuations, whereas, the region $q > q_c$ contains rarely occurring large fluctuations.

4.5 Results

The analysis was initiated by generating equal number of events 3.02×10^4 of UrQMD-hydro (default)[121–123] and UrQMD (default)[54, 55, 124] Monte Carlo (MC) events for central (0-5% $\equiv b \leq 2.0$ fm)[125] Au+Au collisions at 10 AGeV. To examine the applicability of hybrid UrQMD-hydro model at SIS100 energy, another set of MC events for Au+Au collisions at 8 AGeV is generated and the transverse mass (m_T) spectra of π^+ of the generated data is compared with the experimental m_T spectra of E895 experiment (Fig. 4.5(a)). The ratio of both the spectra is shown in Fig. 4.5(b). From these plots it is readily evident that the UrQMD-hydro model generated data is successful in describing the experimental m_T spectra of E895 experiment and thus justifies the applicability of the hybrid UrQMD-hydro model at an energy relevant to this work. Such a claim is also supported by the work of C. Spieles [126] and is shown in Fig. 4.5(c).

To minimise the projection effect, if any, the analyses of the UrQMD-hydro and UrQMD data using SFM technique are being carried out for all charged particles in two dimensional pseudorapidity-azimuthal ($\eta - \phi$) space. Initial shape dependence of the two dimensional density distribution spectrum (Fig. 4.6(a) and (b)) is removed by converting the pseudorapidity (η) and azimuthal angle (ϕ) [$\phi = \tan^{-1}(p_y/p_x)$] values of every primary charged particle of each generated event to a new cumulative variable $\chi(\eta)$ and $\chi(\phi)$ respectively, defined as -

$$\chi(\eta) = \frac{\int_{\eta_{min}}^{\eta} \rho(\eta) d\eta}{\int_{\eta_{min}}^{\eta_{max}} \rho(\eta) d\eta} \quad \text{and} \quad \chi(\phi) = \frac{\int_{\phi_{min}}^{\phi} \rho(\phi) d\phi}{\int_{\phi_{min}}^{\phi_{max}} \rho(\phi) d\phi} \quad (4.15)$$

where, $\eta_{min} = -5.0$, $\eta_{max} = 5.0$, $\phi_{min} = 0$ and $\phi_{max} = 6.28$. Obviously, from equation 4.15, the values of $\chi(\eta)$ and $\chi(\phi)$ vary from 0 to 1. The two dimensional $\chi(\eta - \phi)$ space is now divided into $M_i \times M_i$ bins of equal width $d\chi_\eta \times d\chi_\phi$ where $M_i=1$ to

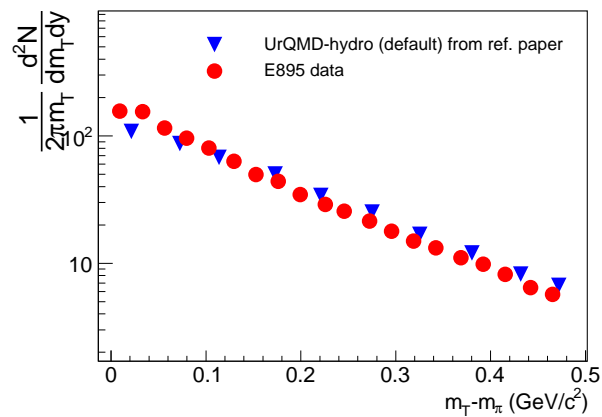
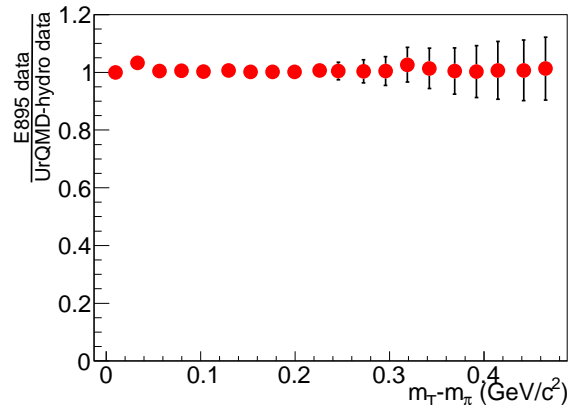
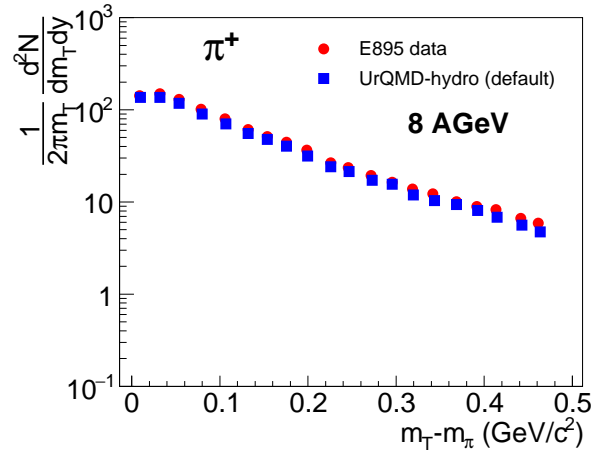


Fig. 4.5 Transverse mass spectra of π^+ for Au+Au collisions at 8 AGeV (a) m_T spectra plotted with our set of UrQMD-hydro generated data and compared with the plot of E895 experimental result [128] (b) ratio of m_T spectra of π^+ of the experimental to our generated data. (c) compared published spectra by C. Spieles using UrQMD-hydro data with experimental spectra of E895.

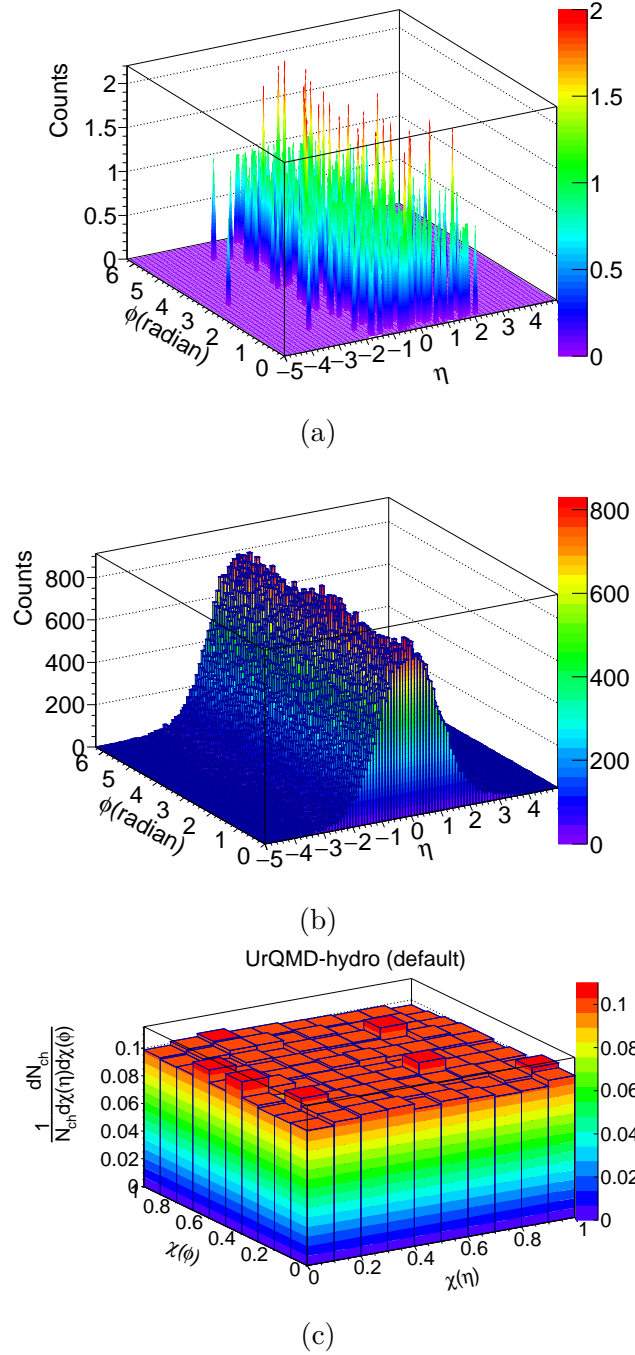
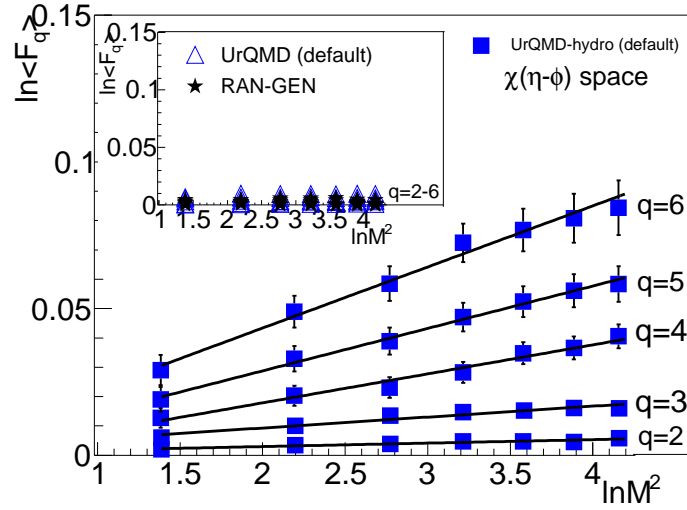
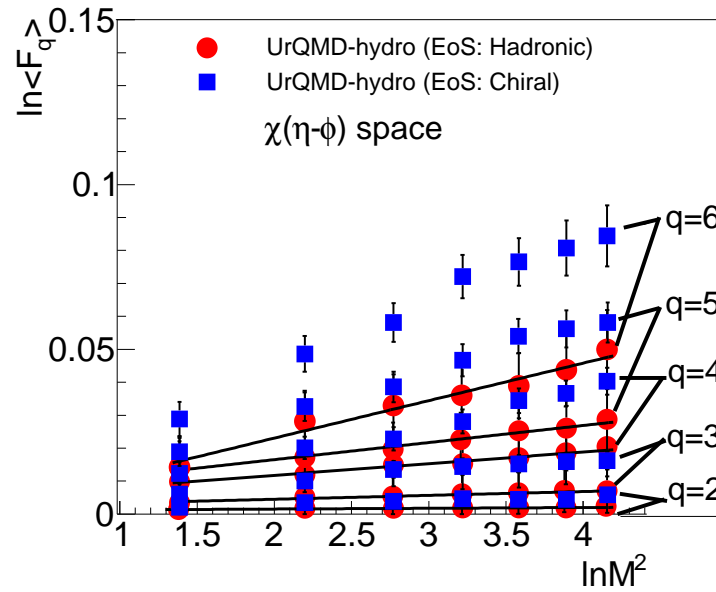


Fig. 4.6 Density distribution spectrum for **(a)** a single event in 2D $\eta - \phi$ space, **(b)** entire sample in 2D $\eta - \phi$ space and **(c)** entire sample in 2D $\chi(\eta - \phi)$ spaces.



(a)



(b)

Fig. 4.7 $\ln \langle F_q \rangle$ vs $\ln M^2$ plots for (a) UrQMD-hydro (default) events and UrQMD and RAN-GEN events (inset) (b) for UrQMD-hydro events with hadronic and chiral equations of state (EoS). Solid straight lines are the best fitted lines to the data points.

10 and $d\chi_\eta = \frac{\chi_{max}(\eta) - \chi_{min}(\eta)}{M} = \frac{1}{M}$ and $d\chi_\phi = \frac{\chi_{max}(\phi) - \chi_{min}(\phi)}{M} = \frac{1}{M}$ [127, 107]. Thus, the minimum and maximum values of $d\chi_\eta$ (and $d\chi_\phi$) would be 0.1 and 1 respectively. Accordingly, the size of the smallest bin of the two dimensional $\chi(\eta - \phi)$ space would be 0.1×0.1 when it is divided into hundred square bins of equal size. The single particle density distribution spectrum of two dimensional $\eta - \phi$ space (Fig. 4.6(b)) is then replotted in two dimensional $\chi(\eta - \phi)$ cumulant phase space as shown in Fig. 4.6(c) with UrQMD-hydro (default) and UrQMD (not shown) generated data. It could be readily seen from Fig. 4.6(c) that, as expected, the distribution is found to be flat in $\chi(\eta - \phi)$ space and is free from any preferential emission thereby minimizing the scope of any error in our fluctuation studies due to initial (kinematic) shape dependence of the single particle spectra itself.

Equal number of events are then generated using random number generator (RAN-GEN) with same multiplicity as that of each event of UrQMD-hydro data with $\chi(\eta)$ and $\chi(\phi)$ values for each particle randomly generated between 0 and 1.

To estimate the scaled factorial moment in two dimensional cumulant $\chi(\eta - \phi)$ space using the above formula (equation 4.12), as stated above, the two dimensional $\chi(\eta - \phi)$ space is successively divided into $M_i \times M_i = M^2 = 1, 4, 9, 16, \dots, 100$ bins of equal width $d\chi_\eta \times d\chi_\phi$. The number of particles populating each square bin is computed to estimate the corresponding SFM. The SFM estimated for each bin are then averaged for all bins and finally over all events to get $\langle F_q \rangle$ for different values of M^2 .

The two dimensional horizontally averaged scaled factorial moments $\langle F_q \rangle$ of order $q = 2 - 6$ are then estimated for $\chi(\eta - \phi)$ space with UrQMD-hydro, UrQMD and RAN-GEN generated data and the values of $\ln \langle F_q \rangle$ are plotted against $\ln M^2$ in Fig 4.7(a). From this plot, a clear signature of the estimated values of $\langle F_q \rangle$ with the increasing number of phase space bin M^2 could be observed confirming the presence

of intermittency in UrQMD-hydro (default) generated data with chiral equation of state (EoS). The error bars shown in these plots are estimated by considering them as independent statistical errors only and the effect of correlation of statistical errors for different bin size has not taken into consideration here. However, as pointed out by several other workers [129–131] exclusion of the correlation of statistical errors does not change the main results appreciably.

Moreover, it is evident from the inset plot of Fig. 4.7(a) that no such intermittency effect could be seen with UrQMD (transport model) and RAN-GEN generated data. The observation with our UrQMD set of generated data is consistent with the results reported by other workers [112, 106]. In hybrid UrQMD model, to account for the non-equilibrium nature of the initial stage of collision, the transport UrQMD model is used as the hydro relies on local thermalization of the produced matter. Further, in the late stage of the heavy ion reaction, the system gets too diluted to apply ideal fluid dynamics. The hadronic re-scattering and decays of resonances have been described by using transport description again. Thus, in hybrid UrQMD-hydro model, both the initial and final stages of the collision are described by transport UrQMD model [22], which does not exhibit any signal of intermittency. The observed intermittency in UrQMD-hydro (default) data could therefore be due to hydrodynamic evolution of the matter created in the collisions or/and due to use of chiral EoS.

To the best of our knowledge, no work on intermittency has been reported yet with UrQMD-hydro generated data and therefore to check the robustness of the observed power law behavior in the hybrid UrQMD-hydro (default) data, new sets of hybrid UrQMD-hydro events are generated by changing the initial conditions such as the start time (t_{start}) of hydrodynamic evolution and the transition energy density (TED), which is related to the end time of the hydrodynamic evolution. In hybrid UrQMD hydro model, while the two lorentz contracted nuclei pass through each other, the coupling

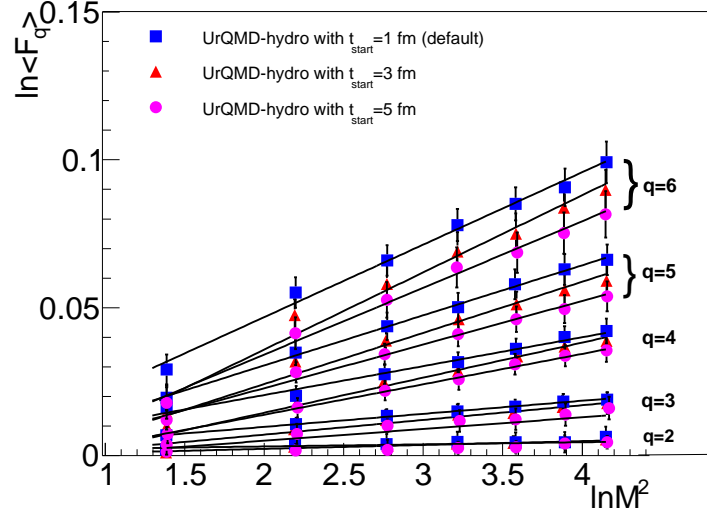


Fig. 4.8 $\ln \langle F_q \rangle$ vs $\ln M^2$ in $\chi(\eta - \phi)$ space for UrQMD-hydro data with different start time (t_{start}). Solid straight lines are the best fitted lines for the data points.

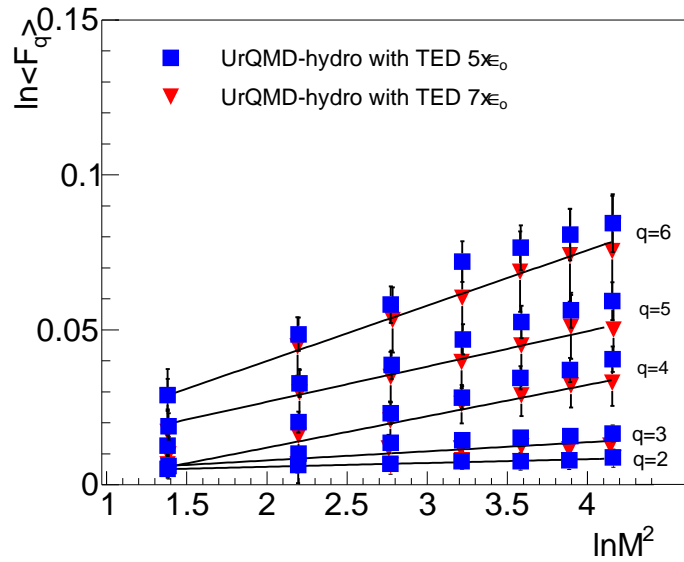
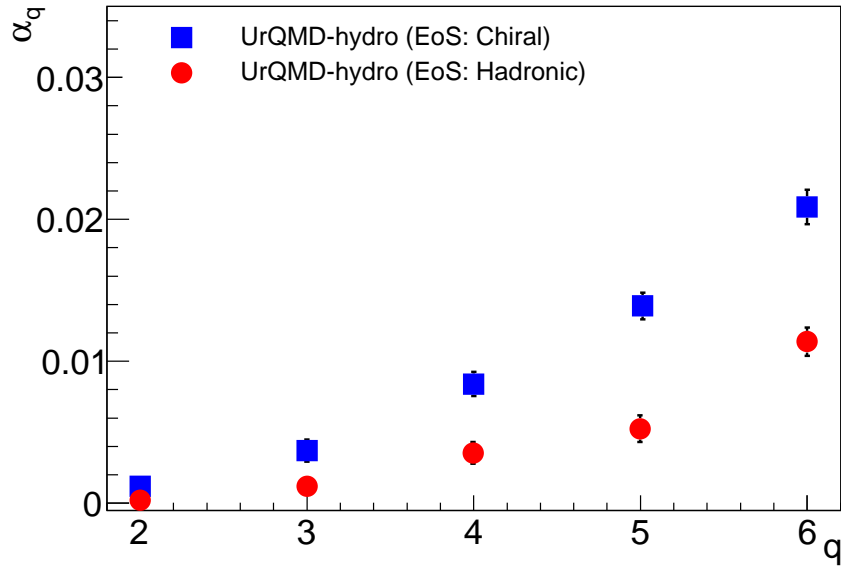
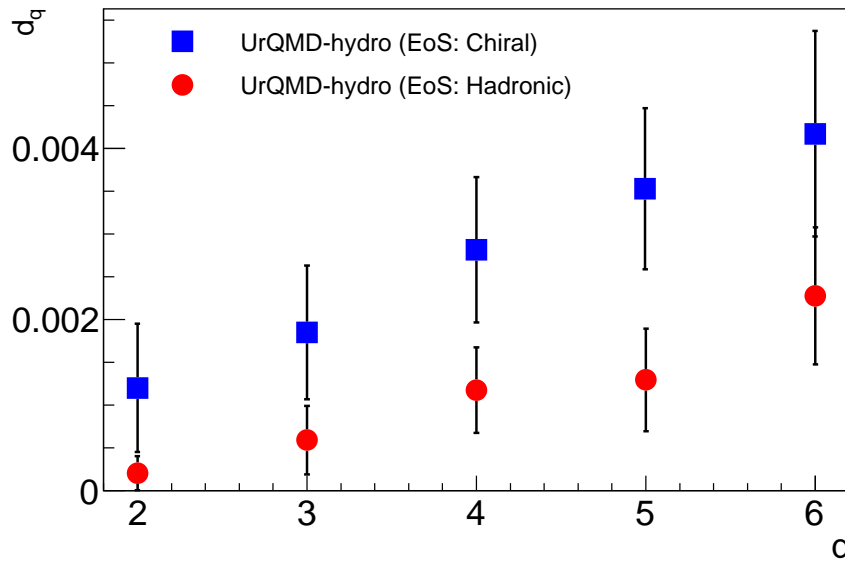


Fig. 4.9 $\ln \langle F_q \rangle$ vs $\ln M^2$ in $\chi(\eta - \phi)$ space for UrQMD-hydro data with two different transition energy density (TED). Solid straight lines are the best fitted lines for the data points.



(a)



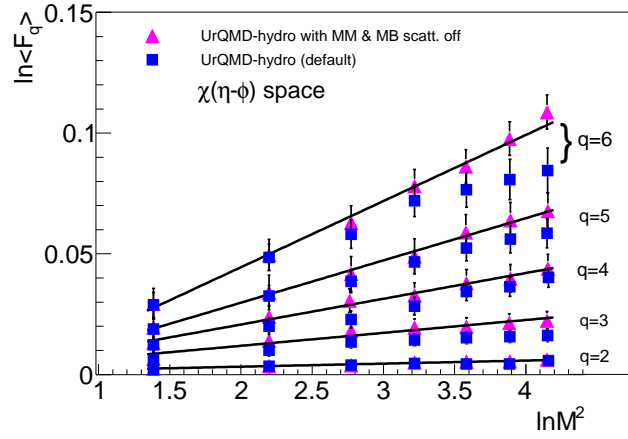
(b)

Fig. 4.10 (a) Intermittency index (α_q) vs q and (b) anomalous fractal dimension (d_q) vs q for UrQMD-hydro data with chiral and hadronic EoS.

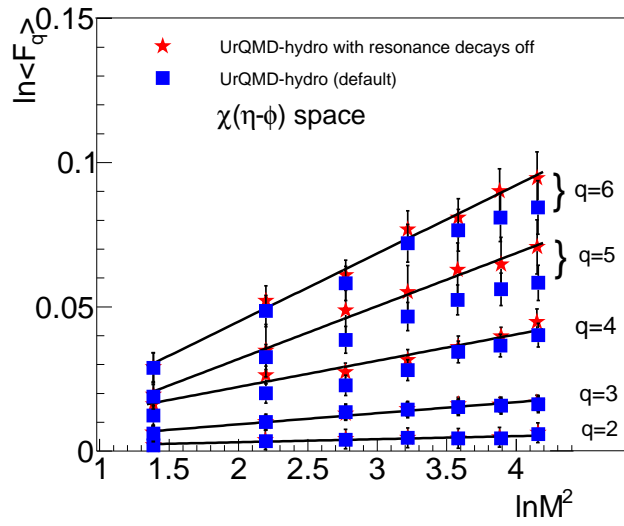
between the UrQMD initial and hydrodynamic evolution takes place. t_{start} is the initial time to begin the hydrodynamic evolution. In Fig. 4.8, $\ln \langle F_q \rangle$ vs $\ln M^2$ is plotted for different t_{start} (1, 3, and 5 fm). It could readily be seen that while the general trend of power law behavior remains unaffected, the strength of intermittency indices decrease with the increase of t_{start} (table. 4.1). For a fixed TED, a large t_{start} means a shorter period of hydrodynamic evolution which in turn weakened the strength of intermittency.

The freeze-out or transition energy density(TED), on the other hand, is the energy density at which the system passes from the local equilibrium phase to the phase of non-equilibrium final state [132, 133]. In other words, it is the energy density at which transition from hydrodynamic to transport description of HIC takes place and is expressed in terms of $\epsilon_o = 145 \text{ MeV}/fm^3$. A higher value of TED means early hadronization. A plot of $\ln \langle F_q \rangle$ against $\ln M^2$ for two different TED is shown in Fig. 4.9 and the power law of SFM is readily evident in this case as well. The observed decrease in the intermittency index could be due to shorter hydrodynamic evolution stage and/or more hadronic re-scattering due to longer final stage.

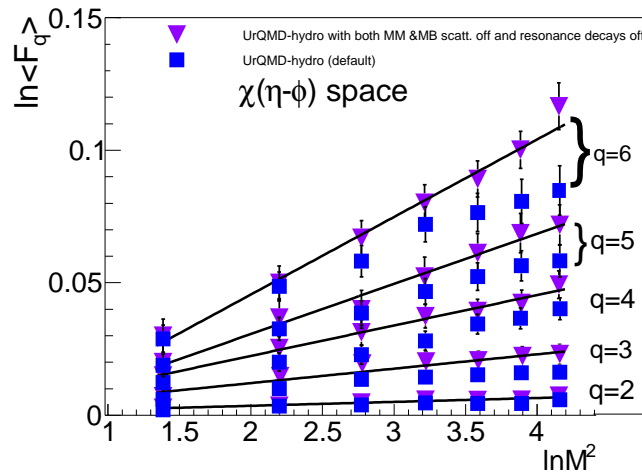
To ascertain the role of EoS (chiral/hadronic) in the observed intermittency in the hydro generated data of this investigation is due to chiral phase transition or not, realised in the model through the use of chiral EoS, another set of UrQMD-hydro data was generated with hadronic EoS. The result of 2D analysis is presented in Fig. 4.7(b) for both the sets of data generated with hadronic and chiral EoS. A clear increase in the values of $\ln \langle F_q \rangle$ against $\ln M^2$ could be seen with UrQMD-hydro central (0-5%) data for both hadronic and chiral EoS. With chiral EoS, the intermittency indices α_q for $q = 2 - 6$ are found to be significantly larger than that of hadronic EoS data. The values of intermittency indices for different order of moments as estimated from this analysis with different sets of data are listed in table 4.1. The errors in α_q are



(a)



(b)



(c)

Fig. 4.11 $\ln \langle F_q \rangle$ vs $\ln M^2$ in $\chi(\eta - \phi)$ space for UrQMD-hydro data with (a) MM and MB scattering off (b) resonance decays off (c) both MM, MB scattering and resonance decays off. Solid straight lines are the best fitted lines for the data points.

Table 4.1 Intermittency index values for $q=2-6$ for various systems using UrQMD-hydro model

Systems	Intermittency				
	$\alpha_2 \times 10^{-3}$	$\alpha_3 \times 10^{-3}$	$\alpha_4 \times 10^{-3}$	$\alpha_5 \times 10^{-3}$	$\alpha_6 \times 10^{-3}$
Hydro with chiral EoS	1.20 ± 0.75	3.70 ± 0.78	8.40 ± 0.85	14.10 ± 0.94	20.80 ± 1.20
Hydro with hadronic EoS	0.20 ± 0.10	1.18 ± 0.32	3.50 ± 0.78	5.20 ± 0.94	11.38 ± 0.99
Hydro with MM and MB scattering off	1.26 ± 0.90	5.31 ± 1.40	10.70 ± 1.46	18.10 ± 1.88	27.9 ± 2.46
Hydro with resonance decays off	1.06 ± 0.61	3.82 ± 0.94	9.19 ± 1.02	17.23 ± 1.38	24.56 ± 1.93
Hydro with both MM, MB and resonance decays off	1.44 ± 0.90	5.38 ± 1.46	13.25 ± 1.40	20.20 ± 1.61	31.50 ± 2.54
<i>Intermittency indices with different t_{start}</i>					
Hydro with $t_{start} = 1\text{fm}$	1.20 ± 0.75	3.70 ± 0.78	8.40 ± 0.85	14.10 ± 0.94	20.80 ± 1.20
Hydro with $t_{start} = 3\text{fm}$	0.90 ± 0.78	3.26 ± 0.80	7.98 ± 0.90	13.29 ± 0.93	19.09 ± 1.14
Hydro with $t_{start} = 5\text{fm}$	0.72 ± 0.80	3.02 ± 0.81	7.43 ± 0.91	12.74 ± 0.94	18.53 ± 1.12
<i>Intermittency indices with different TED</i>					
Hydro with TED = $5 \times \epsilon_o$ fm	1.20 ± 0.75	3.70 ± 0.78	8.40 ± 0.85	14.10 ± 0.94	20.80 ± 1.20
Hydro with TED = $7 \times \epsilon_o$ fm	1.00 ± 0.97	3.11 ± 0.99	8.10 ± 1.32	10.75 ± 2.01	19.11 ± 3.02

estimated by adding the errors in quadrature for three different bin widths [127]. The variation α_q against q for UrQMD-hydro generated data with chiral and hadronic EoS are shown in Fig. 4.10(a). The observed stronger intermittency in the data sample of UrQMD-hydro with chiral EoS than that of hadronic EoS data may be attributed to cascading particle production in partonic media produced due to the use of chiral EoS.

In Fig. 4.10(b), the variation of d_q with q is shown for UrQMD-hydro generated data with both hadronic and chiral equation of states and is found to increase monotonically with the increase of q for both the sets of data. A strong q dependence of d_q is suggestive of particle production via self-similar cascading mechanism indicating about the multifractal nature of the particle spectra. However, d_q is consistently found to be larger in data sample with chiral EoS than that of hadronic EoS indicating the fact that particles of UrQMD-hydro data with chiral EoS occupy less phase space than that of hadronic EoS, or otherwise, particle emission is more preferential in partonic media than that of hadronic media.

The hadronic re-scattering and/or resonance decays have substantial impact on most of the hadronic observables, such as correlations and fluctuations [134, 135]. Experimentally, one measures only final abundances of hadrons which includes both primordial particle production as well as contribution from the resonance decays. Production of resonances plays an important role for studying various properties of interaction dynamics in heavy-ion collisions. Resonances, having short life time that subsequently decay into stable hadrons, as well as hadronic re-scattering can effect the final hadrons yeilds and their number fluctuations [135]. To evaluate the contribution of such processes on the observed intermittency, three new sets of UrQMD-hydro events are generated with (i) meson-meson (MM) and meson-baryon (MB) scattering off but resonance decays on, (ii) MM, MB scattering on but resonance decays off, and (iii) MM, MB, and resonance decays all off. $\ln \langle F_q \rangle$ vs $\ln M^2$ plots for all such events are

shown in Fig. 4.11(a), (b) and (c). It is readily evident from these figures that although all these late stage processes, such as hadronic re-scattering and/or resonance decays weaken the signatures of intermittency significantly, none of these processes are the cause of observed intermittent type of particle emission in our hybrid UrQMD-hydro generated data.

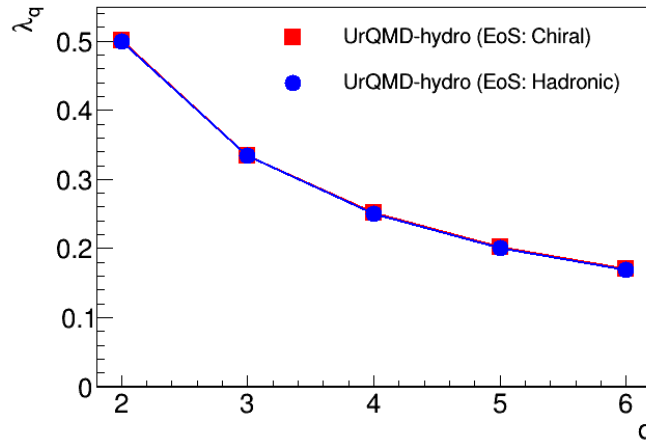
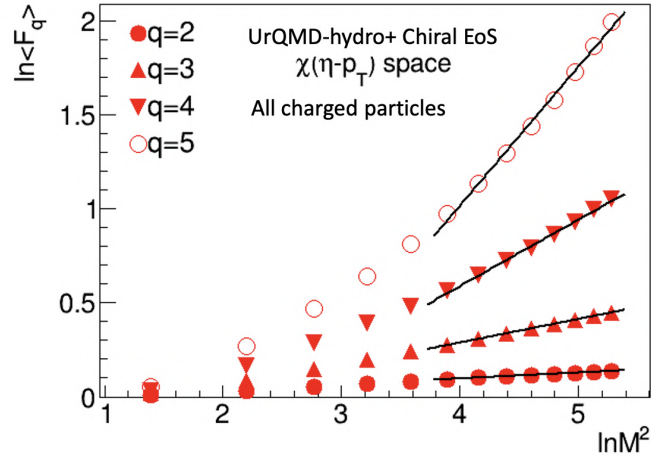


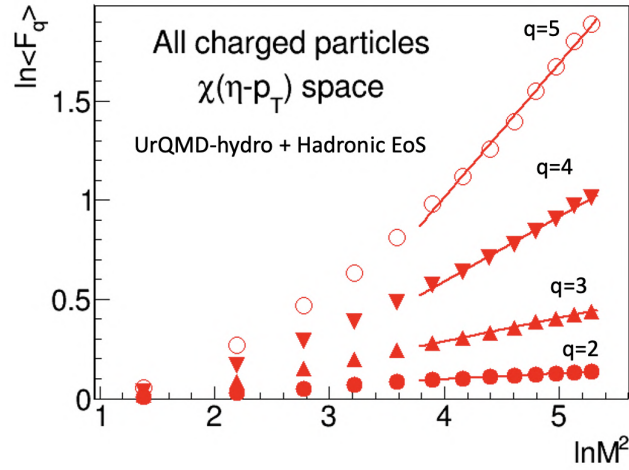
Fig. 4.12 The variation of λ_q against q for UrQMD-hydro generated data at 10 AGeV Au-Au collisions.

Fig. 4.12 displays the variation of λ_q against q for UrQMD-hydro generated data with both chiral and hadronic equation of states. Figure shows that, the value of λ_q decreases with the order of moment q for both the sets of data. From this plot no signature of non-thermal phase transition is seen in our UrQMD-hydro data.

Measurement of multiplicity fluctuations of identified particles produced in ultra-relativistic nucleus-nucleus collisions is motivated by several physics issues. These studies are generally performed to gather information about the matter formed in the collisions and write EoS of the nuclear matter formed in such collisions. Particularly, such fluctuation measurement provide insights into the search for the critical point of strongly interacting matter, revealing the mechanism of hadronization and testing validity of statistical models beyond mean multiplicity of identified hadrons [136, 137].



(a)

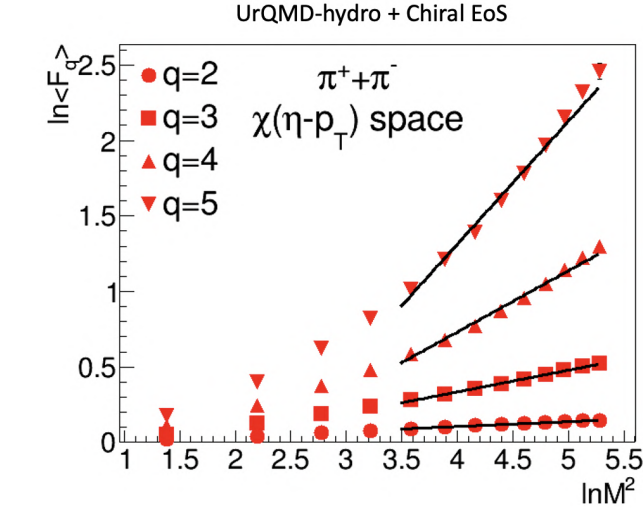


(b)

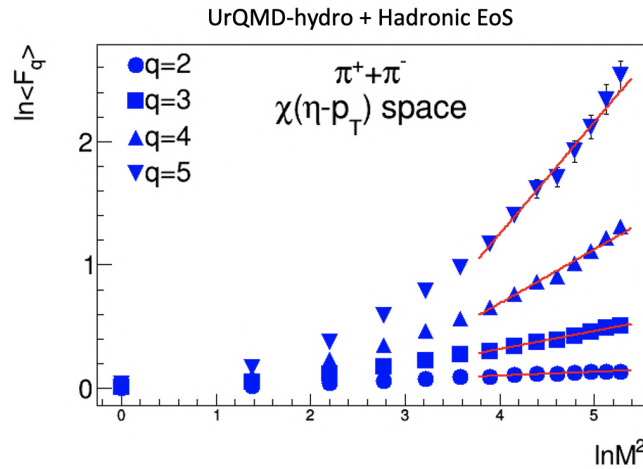
Fig. 4.13 $\ln \langle F_q \rangle$ vs. $\ln M^2$ plot for all charged particles in $\chi(\eta - p_T)$ space for UrQMD-hydro data with (a) chiral EoS, and (b) hadronic EoS.

Moreover, the multiplicity fluctuation of pions with low transverse momentum can provide signal of the formation of disoriented chiral condensates (DCC) [138]. Further, in ref. [139] it has been pointed out that, at the critical point, the fluctuations of the order parameter are self-similar, belonging to the 3D-ising universality class, and can be detected in transverse momentum space within the framework of an intermittency

analysis of proton density fluctuation by the use of scaled factorial moments technique. It is therefore essential to extend the SFM analysis with identified particles as well.



(a)



(b)

Fig. 4.14 $\ln \langle F_q \rangle$ vs. $\ln M^2$ plot for pion in $\chi(\eta - p_T)$ space for UrQMD-hydro data with (a) chiral EoS, and (b) hadronic EoS.

In the above analysis, it has been shown that the UrQMD hydro generated data exhibit an unambiguous signature of intermittency in 2D $\eta - \phi$ space for both chiral and hadronic Equations of States (EoS). In the following, an attempt has therefore been made to study the dynamical fluctuations in 2D $\eta - p_T$ space for various identified

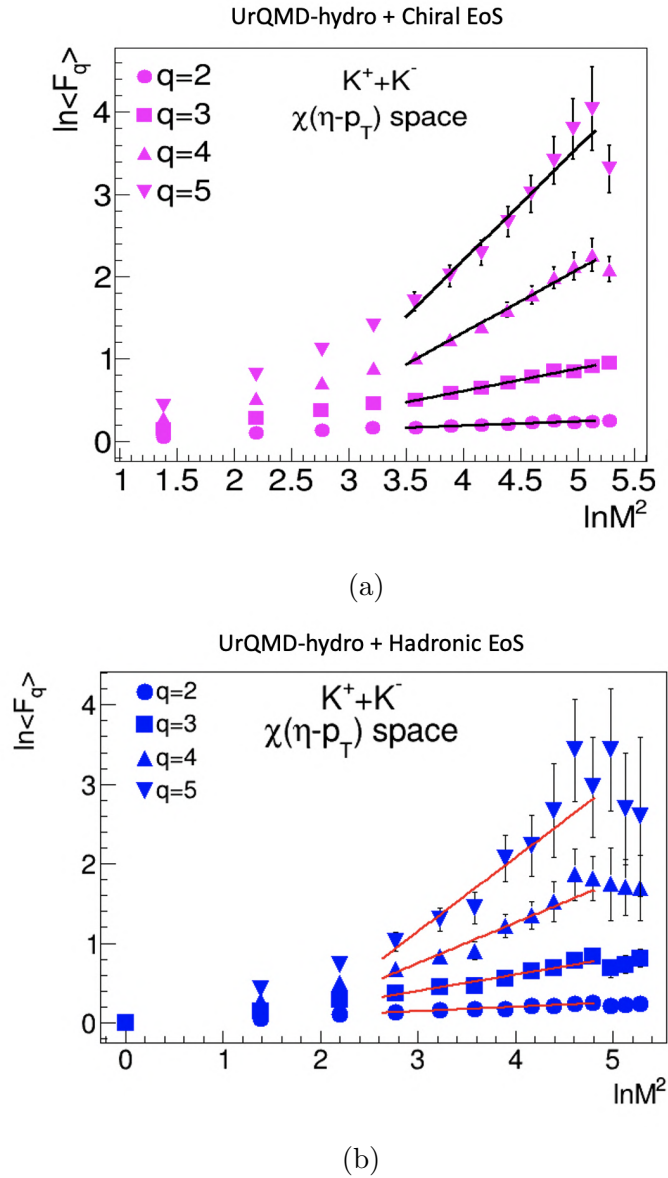
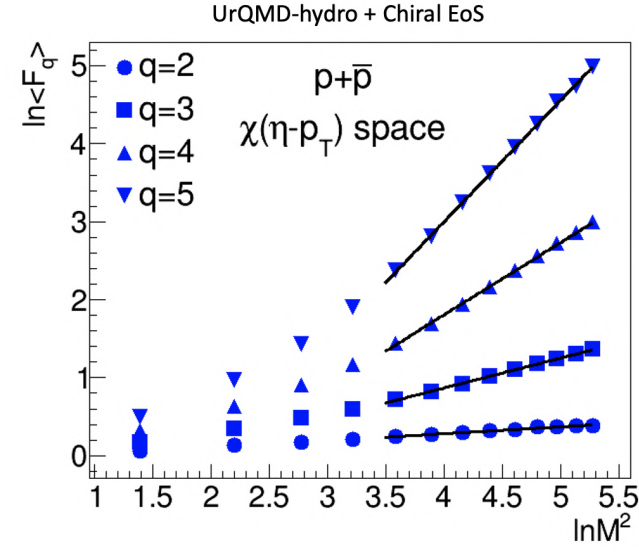


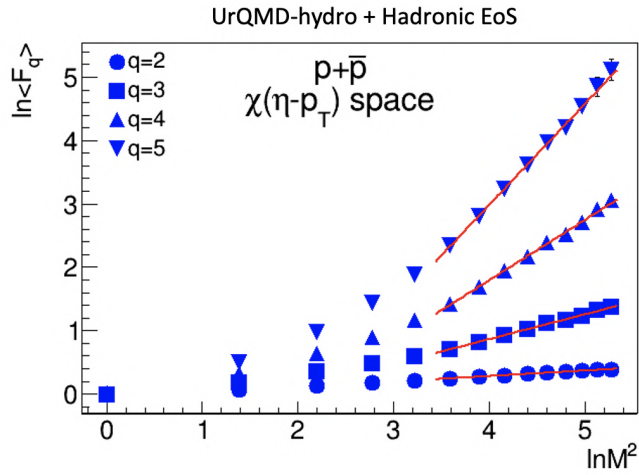
Fig. 4.15 $\ln \langle F_q \rangle$ vs. $\ln M^2$ plot for kaon in $\chi(\eta - p_T)$ space for UrQMD-hydro data with (a) chiral EoS, and (b) hadronic EoS.

particles namely, π , K , and p using the hybrid UrQMD-hydro model generated data for further insight into the collision dynamics.

Horizontally averaged scaled factorial moments $\langle F_q \rangle$ for different order $q = 2 - 5$ for the same sets of generated data for central Au-Au collisions at $E_{lab} = 10$ AGeV have been estimated for $\chi(\eta - p_T)$ space using equation 4.12 and plotted against the



(a)

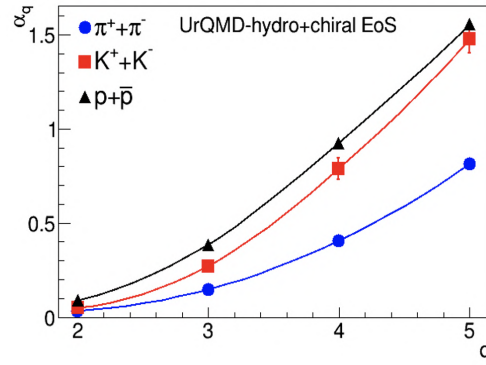


(b)

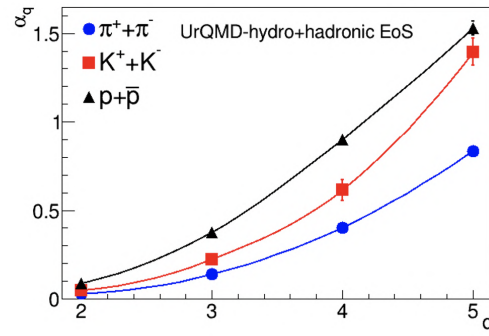
Fig. 4.16 $\ln \langle F_q \rangle$ vs. $\ln M^2$ plot for proton in $\chi(\eta - p_T)$ space for UrQMD-hydro data with (a) chiral EoS, and (b) hadronic EoS.

number of phase-space bins M^2 in log-log scale for all charged particles and is shown in Figs. 4.13 (a) & (b). Significant rise in $\ln \langle F_q \rangle$ against $\ln M^2$ could be seen indicating the presence of dynamical fluctuation in the emission spectra of all charged particles in the new $\eta - p_T$ phase space.

This behaviour is a clear indication of the presence of intermittency and multi-particle correlation in two dimensional pseudorapidity-transverse momentum space in the emission spectra of UrQMD-hydro generated primary particles of central Au-Au collisions at $E_{lab} = 10$ AGeV for both the EoSs.



(a)

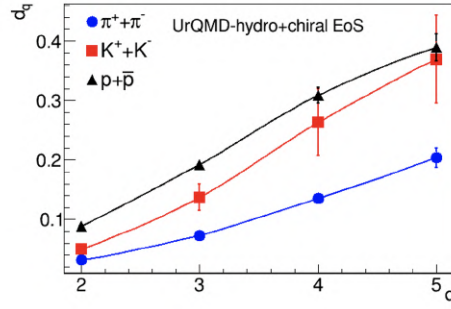


(b)

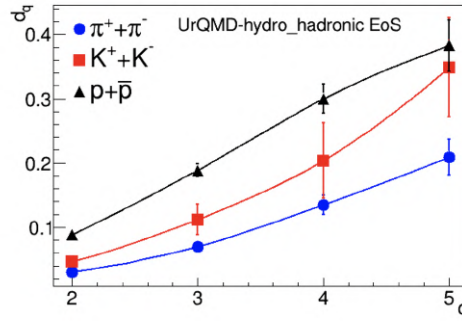
Fig. 4.17 Intermittency indices (α_q) vs. order of moments (q) plot for π , K , and p in $\chi(\eta - p_T)$ space with (a) chiral EoS, and (b) hadronic EoS.

The black solid lines represent the straight line fit of the data points. The straight line is one keeping the correlation coefficient $R^2 = 0.99$. The errors shown in these plots are statistical errors only.

The same $\ln F_q$ vs. $\ln M^2$ plot for identified π , K , p are shown in Figs. 4.14 (a) & (b), 4.15 (a) & (b), and 4.16 (a) & (b) respectively.



(a)



(b)

Fig. 4.18 Variation of values of anomalous fractal dimension (d_q) against order of moments (q) for identified pion, kaon and proton using UrQMD-hydro data with (a) chiral EoS, and (b) hadronic EoS.

Anomalous dimension d_q has been estimated using equation 4.13 from the slopes of Figs. 4.14, 4.15, 4.16 and the variation of α_q and d_q with the order of moments q are shown in Figs. 4.17 & 4.18 respectively. Such an increase of d_q with q indicates the presence of multifractal behaviour in the emission spectra of identified particles in pseudorapidity-transverse momentum space. The variations of λ_q , estimated using the equation 4.14, vs q in $\chi(\eta - p_T)$ spaces are shown in Figs. 4.19 & 4.20. λ_q is found decrease monotonically with q for all charged particles (Figs. 4.19 (a) & (b)). However, for the same plot drawn for identified hadrons (Figs. 4.20 (a) & (b)) a clear minimum could be observed in the plot of λ_q vs. q for all the light flavoured hadrons, readily

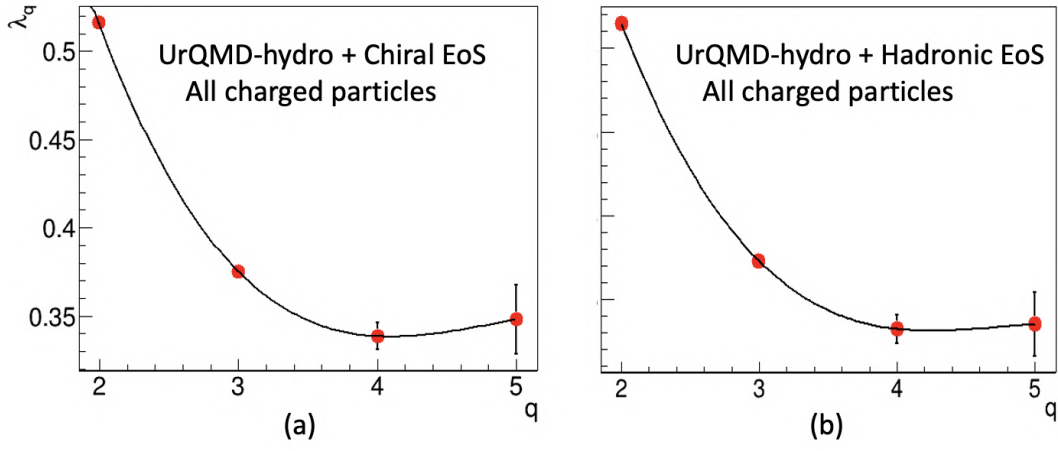


Fig. 4.19 λ_q vs. q plot for all charged particles with (a) chiral EoS, and (b) hadronic EoS.

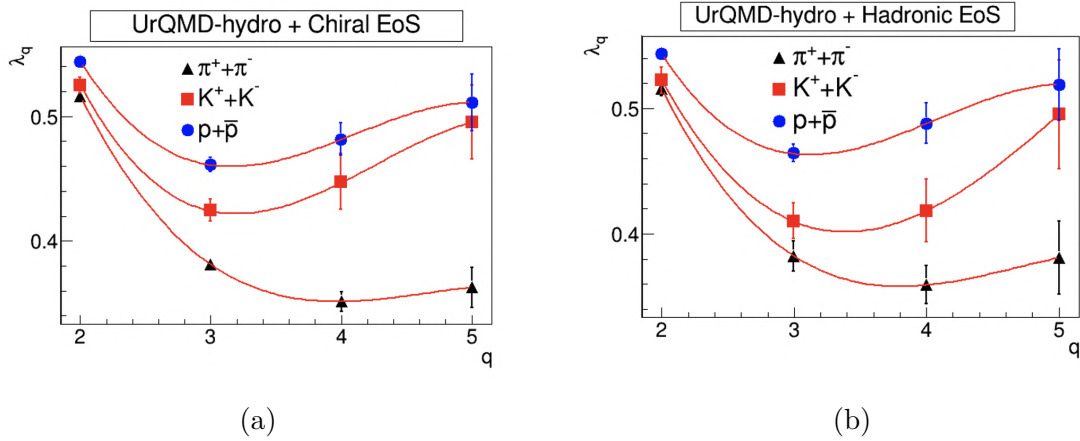


Fig. 4.20 λ_q vs. q plot for identified pion, kaon, and proton using UrQMD-hydro data with (a) chiral EoS, and (b) hadronic EoS.

indicating a non-thermal phase transition in the data sample of UrQMD hybrid hydro data (table 4.2).

It is interesting to observe that the $\lambda_{q(min)}$ value for $q = q_c$ decreases with the mass of identified particles.

Table 4.2 Intermittency index and λ_q values for order of moment $q = 2 - 5$ for all charged particles and different identified particles using UrQMD-hydro model

Particles	Intermittency			
	α_2	α_3	α_4	α_5
<i>Chiral EoS</i>				
All charged particles	0.03142±0.00073	0.1255±0.00061	0.3539±0.00751	0.7401±0.01959
Pion	0.0322±0.00179	0.1440±0.00365	0.4057±0.00802	0.8138±0.01593
Kaon	0.0503±0.00638	0.2724±0.02194	0.7879±0.05611	1.4770±0.07341
Proton	0.0883±0.00166	0.3832±0.00563	0.9264±0.01303	1.5560±0.02287
<i>Hadronic EoS</i>				
All charged particles	0.0297±0.00032	0.1189±0.00239	0.3275±0.00859	0.6752±0.01884
Pion	0.0302±0.00237	0.1390±0.00516	0.4036±0.01501	0.8360±0.02814
Koan	0.0463±0.00669	0.2233±0.02359	0.6106±0.05833	1.3946±0.07749
Proton	0.0879±0.00310	0.3755±0.00998	0.8989±0.02257	1.5303±0.03974
Particles	λ_q			
	λ_2	λ_3	λ_4	λ_5
<i>Chiral EoS</i>				
All charged particles	0.5157±0.00073	0.3752±0.00061	0.3385±0.00751	0.3480±0.01959
Pion	0.5161±0.00180	0.3813±0.00365	0.3514±0.00802	0.3628±0.01593
Kaon	0.5251±0.00638	0.4241±0.02194	0.4470±0.05611	0.4954± 0.07341
Proton	0.5441±0.00166	0.4611±0.00563	0.4816±0.01303	0.5112±0.02287
<i>Hadronic EoS</i>				
All charged particles	0.5149±0.00032	0.3730±0.00240	0.3319±0.00859	0.3350±0.01884
Pion	0.5151±0.00237	0.3797±0.00516	0.3509±0.01501	0.3672±0.02814
Koan	0.5232±0.00669	0.4078±0.02359	0.4027±0.05833	0.4789±0.07749
Proton	0.5440±0.00310	0.4585±0.00998	0.4747±0.02257	0.5061±0.03974

4.6 Summary

In this chapter, the investigation of two dimensional scaled factorial moments analysis on $\chi(\eta, \phi)$ spaces implies that, the data generated with UrQMD transport model or random generator do not exhibit any noticeable signature of self similarity or intermittency. On the other hand, the data of hybrid UrQMD-hydro event generator, which is a mixture of transport and hydrodynamic models, does exhibit intermittency both for hadronic and chiral EoS. The observed power law behavior seen in UrQMD-hydro data with both hadronic and chiral EoS, and not in UrQMD data, confirms that the observed intermittency is not associated with the nature of the medium produced in the heavy-ion collision, but on the mechanism of evolution of the medium produced in such collision. Although, the observed power law behavior is found to be invariant on the changes in initial conditions such as t_{start} and transition energy density (TED) of the hybrid UrQMD-hydro model, the intermittency index significantly changes due to the changes in initial condition. The particle production is found to be more preferential in UrQMD-hydro generated data with chiral EoS than that of hadronic EoS. In our effort to assess the effect of final state re-scattering and resonance decays on the strength of the intermittency, it is found that both hadronic re-scattering and resonance decays only weaken the strength of the intermittency. Thus, the multi particle correlations that could be observed with our UrQMD-hydro data can not arise due to late stage binary decays.

From SFM analysis of identified hadrons in the 2D pseudorapidity-transverse momentum space a clear indication of non-thermal phase transition could be seen. Moreover, there is an indication of the decrease of critical value $q = q_c$ of the order of the moment q for transition from small to large fluctuations with the increasing mass of the hadrons. A more detail investigation on this aspect of non-thermal phase transition needed to be conducted to make a final conclusion on such observation.

5

Summary

The Facility for Anti-proton and Ion Research (FAIR) of GSI, Germany is a future HIC facility that is designed to study proton-proton, proton-nucleus and nucleus-nucleus collisions from 10-45 $AGeV$. The facility will be unique in this energy range in the sense that such collision would be studied with high luminosity beam and therefore rare probes of heavy ion collisions would be studied with better statistics. The proposed Compressed Baryonic Matter (CBM) experiment is one of the four major experiments of FAIR that is planned to investigate nuclear collisions primarily to realise QCD phase transitions, locate QCD critical point, investigate particle production mechanism etc. by studying the rare probes of high energy nucleus-nucleus collisions.

The Time of Flight (ToF) detector is one of the core sub-detectors of CBM experiment, which is an array of Multi-gap Resistive Plate Chambers (MRPC) that will be used in all CBM experiments at SIS100 for the identification of hadrons in a time-of-flight measurement. It is therefore of utmost importance that the simulation of the proposed ToF detector be undertaken for proper design and study the performance of the ToF detector under realistic situation. In this investigation, from the performance studies on ToF simulation using CBM simulation setup version *CbmRoot-JUN16* and *FAIRROOT-nov15p7*, it could be found that the use of above-mentioned simulation software results in a good agreement, as shown in Fig. 3.3 (a) and (b), between the Monte Carlo (MC) points and hit distributions on ToF detector wall. Further, with 2σ cut, the time of flight geometry along with the selection criteria (track fit quality cut $\frac{\chi^2}{NDF} < 3$) used for this analysis can well be used to identify π , K , p up to the momentum of $2.5 \text{ GeV}/c$ and that the produced plot of $1/\beta$ vs. p/q of this work with 2σ cut agrees well with published result of I. Deppner and N. Herrmann [76]. It could be also been seen from this study that with the considered detector set up, as mentioned in section 3.4, all the identified light flavoured particles are found to be fallen well within the expected $y - p_T$ acceptance (Fig. 3.6) for the system under consideration.

From the present investigation it has also been observed that the ToF geometry, as considered in *CbmRoot - JUN16* and *FAIRROOT - nov15p7*, is quite successful in estimating the inverse slope parameters, which are found to be $(185.10 \pm 18.08 \text{ MeV})$ for pions ($\pi^+ + \pi^-$), $(219.00 \pm 25.44 \text{ MeV})$ for Kaons ($K^+ + K^-$), and $(247.00 \pm 19.77 \text{ MeV})$ for proton ($p + \bar{p}$). Although these estimated values are found to be to some extent higher than the expected values, the mass ordering of the inverse slope is quite evident.

Further, the rapidity distribution of π , k , p shows maximum at mid-rapidity which indicates high baryon stopping and thus high baryon density. The widths of the rapidity distribution spectra of the identified π , k , p are found to follow mass ordering (table 3.2). The p_T spectra of TOF identified π , k , p are found to follow the expected Boltzmann distribution pattern. The ratios of reconstructed tracks to MC points of TOF detector calculated from these p_T spectra is above 80 % over the entire p_T range of TOF. From this work, it is thus concluded that the considered TOF geometry of the present investigation, that is, *tof_v16a_1h.geo.root* under *CbmRoot-JUN16* of *FAIRROOT-nov15p7* can well be used for identification of light flavoured particles and in estimation of related observables of HIC of FAIR CBM experiment.

According to lattice QCD calculations, in relativistic heavy ion collisions there is possibility that the nuclear matter undergoes hadronic to partonic type phase transition. Such a phase transition is expected to be first order type in a high baryon density and at moderate temperature, a scenario that is expected to be created at FAIR energies, while such a QCD type phase transition is just a crossover at high temperature and low baryo-chemical potential, that is, at LHC energies. According to QCD, at the end of the first order phase transition, there exists a critical point T_c at which phase transition is of second order. If such a critical point does really exist, it is expected that a number of thermodynamical quantities should exhibit large scale fluctuation around T_c .

The fluctuations of physical observables on an event-by-event basis have been widely used as one of the tools to realize QCD type phase transition. Studies on multiplicity fluctuation is considered to be one of the most widely studied parameters of heavy ion collisions. Scaled factorial moment (SFM) is considered to be one of the most sophisticated methods to separate dynamical fluctuations from the mixture of two. A power law behavior of factorial moment F_q on diminishing phase space bin width δw ,

or otherwise, on increasing number M of bins into which the phase space is divided, that is, $F_q \propto M^{\alpha_q}$ is termed as intermittency where the exponent α_q is called the intermittency index and denotes the strength of intermittency. Keeping in mind the large acceptance of the upcoming Compressed Baryonic Matter (CBM) experiment of Facility for Antiproton and Ion Research (FAIR), Germany as well as the facts that 10 $AGeV$ is the highest achievable energy for A-A collision at SIS100 of FAIR [108], and according to hydrodynamical calculation, the deconfinement phase border is first reached around 10 $AGeV$ [109], in this work, an attempt was made to analyse UrQMD-hydro (in hydrodynamic mode) model generated data using scaled factorial moment technique to realize the presence of intermittency in the data sample and hence to find the critical point, if any. From the present investigation in the two dimensional $\eta - \phi$ space, it could be readily seen from the horizontally averaged scaled factorial moments that the data sample, generated with hybrid UrQMD hydro model at 10 $AGeV$ for Au+Au collisions, for both hadronic and chiral Equation of States (EoS), exhibit a power law behavior of the type $\langle F_q \rangle \propto M^{\alpha_q}$ for the order of the moments $q = 2 - 6$ giving a clear signature of intermittent pattern of particle emission. However, no such signature of intermittency could be seen with UrQMD (transport model) and randomly generated data samples of this work. The observed power law behavior seen in UrQMD-hydro data with both hadronic and chiral EoS, and not in UrQMD data, confirms that the observed intermittency is not associated with the nature of the medium produced in the heavy-ion collision, but on the mechanism of evolution of the medium produced in such collision. As in hybrid UrQMD hydro model, both the initial and final stages of the collision are described by transport UrQMD model [22], which does not exhibit any signal of intermittency, the observed intermittency in UrQMD-hydro (default) data is therefore considered to be due to hydrodynamic evolution of the matter created in the collisions.

To check the robustness of the observed intermittency in our UrQMD-hydro generated data, investigation on horizontally averaged scaled factorial moments is estimated by generating new sets of hydro data by changing the initial conditions such as the start time (t_{start}) of hydrodynamic evolution and the transition energy density (TED), which is related to the end time of the hydrodynamic evolution. It could readily be seen from $\ln \langle F_q \rangle$ vs. $\ln M^2$ plots (Fig. 4.8) for different t_{start} (1, 3, and 5 fm) that while the general trend of power law behavior remains unaffected, the strength of intermittency indices decrease with the increase of t_{start} (table. 4.1). For a fixed TED , a large t_{start} means a shorter period of hydrodynamic evolution which in turn weakened the strength of intermittency.

The freeze-out or transition energy density (TED), on the other hand, is the energy density at which the system passes from the local equilibrium phase to the phase of non-equilibrium final state [22, 23]. In other words, it is the energy density at which transition from hydrodynamic to transport description of HIC takes place and is expressed in terms of $\epsilon_o = 145 \text{ MeV}/\text{fm}^3$. A higher value of TED means early hadronization. A plot of $\ln \langle F_q \rangle$ against $\ln M^2$ for two different TED (Fig. 4.9) reveals the power law of SFM in this case as well. The observed decrease in the intermittency index could be due to shorter hydrodynamic evolution stage and/or more hadronic re-scattering due to longer final stage.

While the intermittency index is found to be more for chiral than the hadronic EoS, in either case its values are found to increase with the order of the moments q (Fig. 4.10). A monotonical increase of the anomalous dimension d_q with the order of the moments q favours cascading mechanism of particle production. Thus, although the observed power law behavior is found to be invariant on the changes in initial conditions such as t_{start} and transition energy density of the hybrid UrQMD-hydro model, the intermittency index significantly changes due to the changes in initial

condition. Further, from an effort to assess the effect of final state re-scattering and resonance decays on the strength of the intermittency, it is found that both hadronic re-scattering and resonance decays only.

From SFM analysis of identified hadrons in the 2D pseudorapidity-transverse momentum space a clear indication of non-thermal phase transition could be seen. Moreover, the critical value of the order of the moment $q = q_c$ for transition from small to large fluctuations are found to decrease with the increasing mass of the hadrons.

80_Recommendation

This particular work that has been undertaken is primarily on detector simulation and physics performance studies of the Time of Flight (ToF) detector to be used in the upcoming FAIR-CBM experiment of GSI, Darmstadt, Germany. Moreover, an attempt has also been made to realize the possible existence of critical point of QCD phase diagram through charged particle multiplicity studies using scaled factorial moment (SFM) technique. The system that has been considered for this work is Au-Au collision at 10 $AGeV$ and the monte carlo (MC) event generators that were used are UrQMD and hybrid UrQMD-hydro models.

From this work, it could be found that the used ToF geometry *tof_v16a_1h.geo.root* is quite successful in identifying light flavored hadrons namely π , K , and p over a momentum range of 2.5 GeV/c . Further, the transverse momentum and rapidity spectrum drawn with these reconstructed π , K , and p showed the general shape of both the spectra and the inverse slope as well as the rapidity width follow the expected mass ordering. Such observation suggests the validity of particle identification done with the considered ToF geometry.

The fluctuation studies revealed a clear intermittency in $\eta - \phi$ space with UrQMD-hydro generated data of present investigation for 10 $AGeV$ Au-Au collision system confirming the existence of large dynamical fluctuation in the data sample. The same

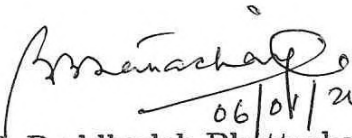
analysis when carried out with the same set of data in $\eta - p_T$ space, reveals a clear signature of nonthermal phase transition.

With the considered ToF geometry of the present investigation and using particle identification parameters used in this work one can easily continue the performance study of the CBM-ToF detector by studying other parameters of HIC such as particle ratio, nuclear modification factor, Λ production, fluctuation studies using SFM, etc. for the same and other different systems.

Somen Gope
06/01/2023
Somen Gope

Gauhati University, Jalukbari

January 2023


06/01/2023
Prof. Buddhadeb Bhattacharjee

Thesis Supervisor

Professor
Department of Phys.
Gauhati University

References

- [1] H. Fritzsche, in QCD 20 Years Later: Proceedings, Workshop, Aachen, Germany, June 9-13 (1992), pp. 827–852.
- [2] C. Amsler et al., Tech. Rep. CERN-PPE-91-215, CERN, Geneva (1991).
- [3] S. H. Menzemer, <https://www.physi.uni-heidelberg.de/Gmenzemer/PPWS1213/Lecture-XV.pdf>.
- [4] F. Karsch, Nuclear Physics A 698, 199 (2002), ISSN 0375–9474, 15th Int. Conf. on Ultra-Relativistic Nucleus-Nucleus Collisions (Quark Matter 2001).
- [5] E. V. Shuryak, “Quantum Chromodynamics and the Theory of Superdense Matter”, Physics Reports 61, 71 (1980), ISSN 0370-1573.
- [6] T. Zhiguan and M. Yunfe, “Phase transition between a hadrons system and QGP from entropy evolution”, Results in Physics 15 (2019) 102627.
- [7] J. Rafelski, “Connecting QGP-Heavy Ion Physics to the Early Universe”, arXiv:1306.2471v1 [astro-ph.CO] 11 Jun 2013.
- [8] U. Heinz, “The Little Bang: Searching for quark-gluon matter in relativistic heavy-ion collisions”, arXiv:hep-ph/0009170v2 19 Sep 2000.
- [9] J. Aichelin, “The expansion of the fireball formed by high energy heavy-ion collision”, Nuclear Physics A 411 (1983) 474-506.

-
- [10] A. Bursche et al., “Physics opportunities with the fixed-target program of the LHCb experiment using an unpolarized gas target”, LHCb-PUB-2018-015.
- [11] <https://en.wikipedia.org/wiki/RelativisticHeavyIonCollider>.
- [12] <https://en.wikipedia.org/wiki/LargeHadronCollider>.
- [13] S. Chattopadhyay et al., “Megaprojects: 2 Facility for Antiproton and Ion Research”, <https://www.ias.ac.in/article/fulltext/reso/024/12/1427-1438>.
- [14] Oliver Boine-Frankenheim, “FAIR beam intensity and quality limitations”, <https://indico.gsi.de/event/3368/sessions/2433/attachments/10888/13281/BoineFrankenheimExpIntenLimitsBeamPhys.pdf>.
- [15] P. Spiller, G. Franchetti, “The FAIR accelerator project at GSI”, *Nuclear Instruments and Methods in Physics Research A* 561 (2006) 305-309.
- [16] T. Stohlker, “Status Report: APPA From Fundamental to Applied Research”, (2020), <https://indico.him.uni-mainz.de/event/71/contributions/364/attachments/256/279/ThomasStoehlker201210%20APPA-KHUK.pdf>.
- [17] G. Boca, CBM Collaboration, “The PANDA experiment : physics goals and experimental setup”, <https://cds.cern.ch/record/1537358/files/p375.pdf>.
- [18] J. Gerlfor, NUSTAR Collaboration, “The NUSTAR Project at GSI and FAIR”, *Exotic Nuclei*, pp. 495-509 (2015).
- [19] P. Senger, “Astrophysics in the Laboratory- The CBM Experiment at FAIR”, <https://arxiv.org/pdf/2004.11214.pdf>.
- [20] S. A. Bass et al., “Microscopic Models for Ultrarelativistic Heavy Ion Collisions”, arXiv:nucl-th/9803035v2 19 Mar 1998.

- [21] M. Bleicher, “Introduction to the UrQMD model”, https://indico.cern.ch/event/719824/contributions/2994580/attachments/1743476/2821635/2018_Bleicher_CERN_v3.pdf.
- [22] H. Petersen et al., “Fully integrated transport approach to heavy ion reactions with an intermediate hydrodynamic stage”, *Phys. Rev. C* **78** 044901 (2008).
- [23] J. Steinheimer et al., “Hadronic SU(3) parity doublet model for dense matter and its extension to quarks and the strange equation of state”, *PHYSICAL REVIEW C* **84**, 045208 (2011).
- [24] K. Rajagopal and F. Wilczek, “THE CONDENSED MATTER PHYSICS OF QCD”, in M. Shifman (ed.): *At the frontier of particle physics*, vol. 3, 2061-2151.
- [25] S. Floerchinger, “Heavy ion physics 1 and 2”, <https://indico.cern.ch/event/381289/contributions/1807997/attachments/1150639/1657352/FloerchingerHeavyIonsL1L2v2.pdf>.
- [26] N. Hussain, Phd Thesis, “Charged particle production in pp and Pb-Pb collisions at Large Hadron Collider (LHC) energies”, (2020).
- [27] P. Sarma, Phd Thesis, “Studies on particle production in proton-proton collisions at the LHC energies using ALICE-TOF and MC data”, (2021).
- [28] Sarkar, S.; Satz, H.; Sinha, B. The physics of the quark-gluon plasma. *Lect. Notes Phys.* 2010, 785, 1–369
- [29] E. Daw, “Lecture 7-Rapidity and Pseudorapidity”, <https://www.hep.shef.ac.uk/edaw/PHY206/Site/2012coursefiles/phy206rlec7.pdf>.
- [30] Z. Tang et al., “The Statistical Origin of Constituent-Quark Scaling in QGP Hadronization”, *Chinese Phys. Lett.* **30** 031201 (2013).

-
- [31] D. M. de Godoy, ALICE Collaboration, “Measurements of the nuclear modification factor and the elliptic azimuthal anisotropy of heavy flavours with ALICE”, Conference Series 458 (2013) 012013.
- [32] F. X. Liu et al., “Study of nuclear modification factors of deuteron and anti-deuteron in Pb-Pb collisions at $\sqrt{s_{NN}} = 2.76$ TeV”, Scientific Reports 12:1772 (2022).
- [33] V. D. Elvira, “Impact of detector simulation in particle physics collider experiments-highlights”, EPJ Web of Conferences 214, 02019 (2019).
- [34] R. Ford and W. Nelson, Standard Linear Accelerator Center Report, SLAC-210, 1978.
- [35] T. Balog, “Overview of the CBM detector system”, J. Phys.: Conf. Ser. 503 012019 (2014).
- [36] V. Friese, “Strangeness and charm in the CBM experiment”, J. Phys. G: Nucl. Part. Phys. 32 S439 (2006).
- [37] Jungyu Yi et al., “Research and development of a CBM-RICH prototype”, EPJ Web of Conferences 20, 05004 (2012).
- [38] C. A. Dritsa, “Design of the Micro Vertex Detector of the CBM experiment: Development of a detector response model and feasibility studies of open charm measurement”, PhD dissertation, 2011.
- [39] <https://www.cbm.gsi.de/detectors/sts>.
- [40] A. Lebedev et al., “Article Track Reconstruction and Muon Identification in the Muon Detector of the CBM Experiment at FAIR”, (2008).

- <https://indico.cern.ch/event/34666/contributions/813491/attachments/683780/939254/lebedev-acat-2008.pdf>
- [41] CBM-RICH Technical Design Report, CBM Collaboration, (2013).
- [42] CBM-TDR Technical Design Report, CBM Collaboration, (2018).
- [43] CBM-TOF Technical Design Report, CBM Collaboration, (2014).
- [44] I. E. Korolko et al., “The CBM ECAL”, J. Phys.: Conf. Ser. 798 012164 (2017).
- [45] CBM-PSD Technical Design Report, CBM Collaboration, (2015).
- [46] M. Al-Turany, D. Bertini, and I. Koenig. CbmRoot: Simulation and analysis framework for CBM experiment. In S. Banerjee, editor, Computing in High Energy and Nuclear Physics (CHEP-2006), volume 1 of MACMILLAN Advanced Research Series, pages 170–171. MACMILLAN India, 2006.
- [47] K. Dey, Phd Thesis, “A Study on the MUCH Geometry Optimization and Physics Observables of the Proposed FAIR-CBM Experiment”, (2017).
- [48] R. Burn et al., “GEANT3”, (1987). <https://cds.cern.ch/record/1119728/files/CERN-DD-EE-84-1.pdf>
- [49] S. Agostinelli et al., “Geant4-a simulation toolkit”, Nuclear Instruments and Methods in Physics Research Section A: Accelerators, Spectrometers, Detectors and Associated Equipment, 506, 250-303 (2003).
- [50] A. Ferrari, “Fluka: a multi-particle transport code”, (2021). <http://www.fluka.org/content/manuals/FM.pdf>.
- [51] R. Brun and F. Rademakers, “ROOT: An object oriented data analysis framework”, Nucl. Instrum. Meth. A 389, 81 (1997).

-
- [52] T. Sjostrand, p. 25 p (1991), URL <https://cds.cern.ch/record/226013>.
- [53] S. Lehti, “Computing Methods In High Energy Physics”, Spring 2016, Helsinki Institute of Physics (Lecture 8), (2016).
- [54] M. Bleicher et al., “Relativistic hadron-hadron collisions in the ultra-relativistic quantum molecular dynamics model”, J. Phys. G: Nucl. Part. Phys. **25** 1859–1896 (1999).
- [55] S. Bass et al., “Microscopic models for ultrarelativistic heavy ion collisions”, Prog. Part. Nucl. Phys. **41** 225-370 (1998).
- [56] URL: <https://www.gsi.de/work/wissenschaftlichenetzwerke/helmholtzvirtuelleinstitute/unigen>.
- [57] I. Fröhlich et al., “Design of the pluto event generator”, Journal of Physics: Conference Series 219, 032039 (2010).
- [58] P. Alken, “GSL Technical Report”, (2022). URL: <https://www.gnu.org/software/gsl/tr/tr001.pdf>.
- [59] L. Lonnblad, “Clhep - a class library for high energy physics”, (2008). URL: <http://proj-clhep.web.cern.ch/proj-clhep/>.
- [60] B. Dawes et al., “Boost c++ libraries”, (2007). URL: <http://www.boost.org/>.
- [61] D. Bertini et al., “Computing in High Energy and Nuclear Physics (CHEP-2006)”, Proceedings, (2006).
- [62] M. Al-Turany et al., “computing in High Energy and Nuclear Physics (CHEP-2006)”, Proceedings, (2006), TIFR Mumbai (India).
- [63] URL: <https://root.cern.ch/doc/master/classTTree.html>.

- [64] E. L. Bratkovskaya et al., CBM Technical Status Report, CBM Collaboration, (2005). URL: <http://triton.itep.ru/ions/Methodics/CBMECAL/CBM-TSR-DOC-2006-Feb-108-1.pdf>.
- [65] S. Chattopadhyay et al., Technical Design Report for the CBM : Muon Chambers (MuCh) (GSI, Darmstadt, 2015).
- [66] S. Blyth, PhD thesis, University of Cape Town, South Africa (2007).
- [67] W. N. Alberico, M. Nardi and M. P. Lombardo, QUARK-GLUON PLASMA and HEAVY ION COLLISIONS, (World Scientific, 2002).
- [68] K. Aamodt et al. (ALICE collaboration), “Centrality Dependence of the Charged-Particle Multiplicity Density at Midrapidity in Pb-Pb Collisions at $\sqrt{s_{NN}} = 2.76$ TeV” Phys. Rev. Lett. 106, 032301 (2011).
- [69] J. STACHEL, “Systematics of global observables in relativistic heavy ion collisions”, Nucl. Phys. A 525, 23c–38c (1991).
- [70] K. Adcox et al. (PHENIX Collaboration), “Formation of dense partonic matter in relativistic nucleus–nucleus collisions at RHIC: Experimental evaluation by the PHENIX Collaboration”, Phys. A 757, 184 (2005).
- [71] <http://www1.maths.leeds.ac.uk/~kersale/2620/Notes/chapter5.pdf>.
- [72] I. G. Bearden et al. (The NA44 Collaboration), “Collective Expansion in High Energy Heavy Ion Collisions”, Phys. Rev. Lett. 78, 2080 (1997).
- [73] M. Gazdzicki and M. I. Gorenstein, “Power law in hadron production”, Phys. Lett. B517, 250-254 (2001).
- [74] Technical Design Report for the CBM, Time of Flight, CBM Collaboration, oct (2014).

-
- [75] S. Gope and B. Bhattacharjee, “Charged particle identification with CBM TOF”, CBM-progress report, (2017).
- [76] I. Deppner and N. Harrmann, “The FAIR Phase 0 program of the CBM TOF”, arXiv:2006.08510v2 [physics.ins-det] 31 JUL (2020).
- [77] Z. Liu et al., “Novel low resistivity glass: MRPC detectors for ultra high rate applications”, Nuclear Inst. and Methods in Physics Research, A, 959 (2020) 163483.
- [78] Yi Wang et al., “Multigap Resistive Plate Chambers for Time of Flight Applications”, Applied Sciences, 2021, 11, 111.
- [79] G. Nail, “Quantum Chromodynamics: Simulation in Monte Carlo Event Generator”, Ph.D. thesis, 2017, University of Manchester.
- [80] M. H. Seymour, “Quantum Chromodynamics”, arXiv:hep-ph/0505192v2 9 Oct (2010).
- [81] B. J. Schaefer, J. Wambach, “Susceptibilities near the QCD (tri)critical point”, Phys. Rev. D 75, 085015 (2007).
- [82] T. Hatsuda, T. Kunihiro, “QCD phenomenology based on a chiral effective Lagrangian”, Phys. Reports 247 (1994) 22 1—367.
- [83] S. Jeon and V. Koch, Hwa, R.C. (ed.) et al.: Quark gluon plasma, 430-490 (2003), arXiv:hep-ph/0304012 (2003).
- [84] A. Adare et al. (PHENIX Collaboration), “Charged hadron multiplicity fluctuations in Au+Au and Cu+Cu collisions from $\sqrt{S_{NN}}=22.5$ to 200 GeV” Phys. Rev. C 78, 044902 (2008).

-
- [85] M. A. Stephanov, K. Rajagopal and E. V. Shuryak, “Signatures of the Tricritical Point in QCD”, *Phys. Rev. Lett.* 81, 4816 (1998).
- [86] A. Chandra et al., “Centrality Dependence of Multiplicity Fluctuations in Ion-Ion Collisions from the Beam Energy Scan at FAIR”, *Advances in High Energy Physics*, Volume 2019, (2019).
- [87] X. Luo, and Nu Xu, “Search for the QCD critical point with fluctuations of conserved quantities in relativistic heavy-ion collisions at RHIC: an overview”, *Nuclear Science and Techniques* 28, **112** (2017).
- [88] M. Mukherjee, Phd. thesis, “EVENT-BY-EVENT MULTIPLICITY FLUCTUATIONS IN HIGH ENERGY HEAVY ION COLLISIONS AT THE LHC ENERGIES IN THE ALICE EXPERIMENT”, 2016.
- [89] Radka Sochorová et al., “Evolution of multiplicity fluctuations in heavy ion collisions”, arXiv:1901.10919v1 [nucl-th] 30 Jan 2019.
- [90] C. Alt et al., NA49 Collaboration, “Energy Dependence of Multiplicity Fluctuations in Heavy Ion Collisions”, *Proceedings of Science*, PoS (CFRNC 2006) 024.
- [91] C. Pruneau et al., “Methods for the study of particle production fluctuations”, *Phys. Rev. C* 66, 044904 (2002).
- [92] B. Sharma, STAR Collaboration, “Dynamical net charge fluctuations at RHIC energies in STAR”, arXiv:1512.00145v1 [nucl-ex] 1 Dec 2015.
- [93] S. Ghosh, P. Mali, A. Mukhopadhyay, “Net-charge fluctuation in Au+Au collisions at energies available at the Facility for Antiproton and Ion Research using the UrQMD model”, *Phys. Rev. C* 96, 024912 (2017).

-
- [94] P. Bozek and W. Broniowski, “Transverse-momentum fluctuations in relativistic heavy-ion collisions from event-by-event viscous hydrodynamics”, *Phys. Rev. C* **85**, 044910 (2012), arXiv:1203.1810 [nucl-th].
- [95] J. Adams et al. (STAR), “Incident energy dependence of pt correlations at relativistic energies”, *Phys. Rev. C* **72**, 044902 (2005), arXiv:nucl-ex/0504031.
- [96] L. Adamczyk et al. (STAR), “Bulk properties of the medium produced in relativistic heavy-ion collisions from the beam energy scan program”, *Phys. Rev. C* **96**, 044904 (2017), arXiv:1701.07065 [nucl-ex].
- [97] M.A. Stephanov, K. Rajagopal, E.V. Shuryak, “Signatures of the Tricritical Point in QCD”, *Phys. Rev. Lett.* **81** (1998) 4816.
- [98] D. Adamova et al., CERES Collaboration, “Event-by-event fluctuations of the mean transverse momentum in 40, 80, and 158 AGeV/c Pb–Au collisions”, *Nuclear Physics A* **727** (2003) 97–11.
- [99] U. Frisch, *Turbulence: The legacy of A. N. Kolmogorov* (Cambridge University Press, Cambridge, UK, 1995).
- [100] B. L. Hao, “Chaos” (World Scientific, Singapore, 1984), *ISBN* : 9971966514.
- [101] K. R. Sreenivasan et al., “The fractal facets of turbulence”, *J. Fluid. Mech* **173** 357-386 (1986).
- [102] T. H. Burnett et al., JACEE Collaboration, “Particle correlations in JACEE nucleus-nucleus collisions”, Organizing Committee of the 21st Int. Cosmic Ray Conf.
- [103] D. Ghosh et al., “Multi dimensional fluctuation analysis of target residue in nuclear collision”, *Indian J. Phys.* **80** (7), 745-752 (2006).

-
- [104] T. Anticic et al. (NA49 Collaboration), “Critical fluctuations of the proton density in A+A collisions at 158 AGeV”, *Eur. Phys. J. C* **75**, 587 (2015).
- [105] J. Wu et al. (for the STAR Collaboration), presentation at ISMD2021, virtual conference, 12–16 July 2021.
- [106] S. Bhattacharjee et al., “A STUDY OF MULTIFRACTALITY AND PHASE TRANSITION IN HEAVY-ION COLLISIONS - EXPERIMENTAL DATA VERSUS MODEL SIMULATION”, *Fractals*, **26** 1850015 (2018).
- [107] P. Sarma et al., “Color reconnection as a possible mechanism of intermittency in the emission spectra of charged particles in PYTHIA-generated high-multiplicity pp collisions at energies available at the CERN Large Hadron Collider”, *Phys. Rev. C* **99** 034901 (2019).
- [108] CBM Collab. (S. Seddiki), “The Compressed Baryonic Matter experiment”, *J. Phys. Conference Series* **503** 012027 (2014).
- [109] CBM Collab. (P. Satszel et al.), “CBM EXPERIMENT AT FAIR”, *Acta Physica Polonica B* **41** 341 (2010).
- [110] N. Hussain et al., “Role of net baryon density on rapidity width of identified particles from the lowest energies available at the CERN Super Proton Synchrotron to those at the BNL Relativistic Heavy Ion Collider and at the CERN Large Hadron Collider”, *Phys. Rev. C* **96** 024903 (2017).
- [111] V. Ozvenchuk et al., “Transverse momentum spectra of hadrons in $p + p$ collisions at CERN SPS energies from the UrQMD transport model”, *Nucl. Phys. A* **973** 104–115 (2018).
- [112] J. Wu et al., “Probing QCD critical fluctuations from intermittency analysis in relativistic heavy-ion collisions”, *Phys. Lett. B* **801** 135186 (2020).

-
- [113] A. Bialas, "Intermittency '90", Nucl. Phys. A **525**, 345C (1991).
- [114] A. Bialas et al., "Intermittency in multiparticle production at high energy", Nucl. Phys. B **308** 857-867 (1988).
- [115] R. C. Hwa et al., "Intermittency in second-order phase transitions", Phys. Rev. Lett. **69** 5 (1992).
- [116] A. Bialas et al., "Moments of rapidity distributions as a measure of short-range fluctuations in high-energy collisions", Nucl. Phys. B **273** 703-718 (1986).
- [117] R. C. Hwa and Q. Zhang, "Erraticity of rapidity gaps", Phys. Rev. D **62** 014003 (2000).
- [118] B. Bhattacharjee, "Signature of intermittent behavior in the emission spectra of target associated particles from Kr-AgBr interactions at 0.95 AGeV", Nucl. Phys. A **748** 641 (2005).
- [119] A. Bialas et al., "A new variable to study intermittency", Phys. Lett. B **252** 483 (1990).
- [120] P. Lipa et al., "From strong to weak intermittency", Phys. Lett. B **223** 465 (1989).
- [121] D. H. Rischke et al., "Relativistic hydrodynamics for heavy ion collisions. 1. General aspects and expansion into vacuum", Nucl. Phys. A **595** 346-382 (1995).
- [122] D. H. Rischke et al., "Relativistic hydrodynamics for heavy ion collisions. 2. Compression of nuclear matter and the phase transition to the quark-gluon plasma", Nucl. Phys. A **595** 383-408 (1995).
- [123] D. Zschesche et al., "Particle ratios at RHIC: Effective hadron masses and chemical freeze-out", Phys. Lett. B **547** 7-14 (2002).

- [124] Sascha Vogel et al., “Resonance studies with the UrQMD model”, EPJ Web of Conferences **36** 00019 (2012).
- [125] V. Klochkov et al., “Centrality determination in heavy-ion collisions with the CBM experiment”, Conference Series, J. Of Phys. G, 798 (2017) 012059.
- [126] C. Spieles et al., “Effects of the QCD phase transition on hadronic observables in relativistic hydrodynamic simulations of heavy-ion reactions in the FAIR/NICA energy regime”, arXiv:2006.01220v1 [nucl-th] 1 Jun 2020.
- [127] EMU01 Collab. (M. Adamovich et al.), “On Intermittency in heavy ion collisions and the importance of gamma conversion in a multidimensional intermittency analysis”, Nucl. Phys. B **388** 3 (1992).
- [128] E895 Collab. (J. L. Klay et al.), “Charged pion production in 2 to 8 agev central au+au collisions”, Phys. Rev. C **68** 054905 (2003).
- [129] NA22 Collab., (I. V. Ajinenko et al.), “Intermittency patterns in π^+ p and K^+ p collisions at 250 GeV/c ”, Phys. Lett. B **222** 306 (1989).
- [130] C. B. Chiu et al, “NON-STATISTICAL COMPONENT OF THE MULTIFRACTAL SPECTRAL FUNCTION”, Mod. Phys. Lett. A **5**, 2651 (1990).
- [131] N. M. Agarbalyan et al., “Self-affine fractality in π^+ p and K^+ p collisions at 250 GeV/c ”, Phys. Lett. B **382**, 305 (1996).
- [132] J. Steinheimer et al., “Non-thermal p/π ratio at LHC as a consequence of hadronic final state interactions”, arXiv:1203:5302 v2 [nucl-th] 2013.
- [133] J. Steinheimer et al., “Nonthermal p/π Ratio at LHC as a Consequence of Hadronic Final State Interactions”, Phys. Rev. Lett. **110** 042501 (2013).

-
- [134] J. Steinheimer et al., "Final state hadronic rescattering with UrQMD", EPJ Web of Conferences **171** 05003 (2018).
- [135] D. K. Mishra et al., "Effect of resonance decay on conserved number fluctuations in a hadron resonance gas model", Phys. Rev. C **94** 014905 (2016).
- [136] Z. Fodor and S. D. Katz, "Finite T/μ lattice QCD and the critical point", Prog. Theor. Phys. Suppl. 153, 86 (2004), hep-lat/0401023.
- [137] V. Koch, "Hadronic Fluctuations and Correlations", Landolt-Bornstein-Group I Elementary Particles, Nuclei and Atoms, (2010).
- [138] M. Bleicher, J. Randrup, R. Snellings, and X.-N. Wang, "Enhanced event-by-event fluctuations in pion multiplicity as a signal of disoriented chiral condensates in relativistic heavy-ion collisions", Phys. Rev. C **62**, 041901(R) (2000).
- [139] N. Davis, N. Antoniou, F. Diakonos, "Searching for the QCD critical point through power-law fluctuations of the proton density in heavy-ion collisions", Acta. Phys. Polon. Supp. 10, 537-541 (2017).